Turbulent Flow Separation Control by Boundary-layer Forcing: A Computational Study

Vom Fachbereich Maschinenbau an der
Technischen Universität Darmstadt zur
Erlangung des Grades eines Doktor-Ingenieurs
(Dr.-Ing.) genehmigte

D i s s e r t a t i o n

vorgelegt von

Sanjin Šarić, M.Sc.

aus Sarajevo

Berichterstatter:	Prof. Dr.-Ing. C. Tropea
Mitberichterstatter:	Prof. Dr.-Ing. F. Thiele
	Priv.-Doc. Dr.-Ing. habil. S. Jakirlić
Tag der Einreichung:	05.09.2006
Tag der mündlichen Prüfung:	20.12.2006

Darmstadt 2006
D17

to Una

Acknowledgments

I wish to express my gratitude to Prof. Cameron Tropea and Dr. Suad Jakirlić for the opportunity to conduct a research work at the Chair for Fluid Dynamics and Aerodynamics (FG SLA). Special thanks go to my supervisor Dr. Jakirlić for his advices, guidance, fruitful discussions and continuous support throughout this work. Helpful suggestions and discussions with my colleagues from FG SLA are greatly appreciated.

I use this opportunity to express sincere gratitude to the administrative staff at FG SLA.

The financial support of the Deutsche Forschungsgemeinschaft (DFG) through the grants GK "Modeling and numerical description of technical flows" and the research group on "Large-eddy Simulation of Complex Flows" (FOR 507/1, JA 941/7-1) is particularly acknowledged.

Finally, I wish to express heartfelt thanks to my family for providing loving support, especially to my wife Aida and daughter Una without whose love, understanding and support I could never have done this work.

Darmstadt, September 2006

Sanjin Šarić, M.Sc.

Abstract

Recent experimental studies have demonstrated that active flow control (AFC) has a potential to enable significant advances in many engineering applications. Though demonstrated experimentally, unsteady separation flow control remains a challenge for Computational Fluid Dynamics (CFD). The main goal of this work was a computational study of the effects of boundary-layer forcing on the mean flow and turbulence using various methods for turbulent flow computations: Large-eddy simulation (LES), Reynolds-averaged Navier-Stokes (RANS) and Detached-eddy Simulation (DES), aiming also at mutual comparison of their features and performance in complex flow situations. Predictive capability of various CFD methods were evaluated for the three representative complex separated flow configurations without flow control. A potential of the methods for unsteady flow computations: LES, DES and URANS was investigated by predicting the flow and turbulence field for the two experimentally investigated AFC configurations. They involve the two recent experimental works pertinent to AFC: periodically perturbed backward-facing step (BFS) flow at a low Reynolds number (Yoshioka et al. [77, 78]) and high Reynolds number flow over a wall-mounted hump (Greenblatt et al. [22, 23]). In general, both the LES and DES computations have reproduced all important effects observed in the BFS experiments. The imposed perturbation frequency corresponding to $St = 0.19$ was found to be the optimum one, leading to the maximum reduction of the reattachment length. URANS underpredicts substantially the intensity of the reduction, exhibiting a very weak sensitivity to the perturbations. Beside a close agreement with the experiment concerning time-mean behaviour of the flow for all perturbation frequencies, the extracted phase-averaged LES results for the case with the optimum frequency ($St = 0.19$) compare well with the reference experimental data. The LES and DES predictions of the main characteristics of separated flow over a wall-mounted hump, obtained on relatively coarse grids with respect to the flow Reynolds number considered ($Re_c = 9.36 \cdot 10^5$), are encouraging, outperforming significantly the examined RANS models. The numerous simulations of the flow configurations pertinent to active flow control (AFC) have been carried out providing a picture of the current status of CFD in AFC applications.

Zusammenfassung

Aktive Kontrolle der Strömungsablösung durch die Grenzschichtbeeinflussung: eine numerische Studie

Die neuesten experimentellen Studien veranschaulichen deutlich das große Potential der aktiven Strömungskontrolle (*Active Flow Control* – AFC) und deren wichtigen Vorteile im Hinblick auf die Gewinnung von optimalen Strömungseigenschaften in puncto der Verminderung der Druckverluste in unterschiedlichen industriellen Anwendungen. Trotz der experimentellen Evidenz stellt die korrekte Ermittlung der Kontrollmechanismen der instationären Strömungsablösung noch immer eine große Herausforderung für die Methoden der numerischen Strömungsmechanik (*Computational Fluid Dynamics* – CFD) dar. Das Hauptziel der vorliegenden Arbeit ist die numerische Untersuchung der Effekte der Grenzschichtbeeinflussung auf die mittlere Strömung und Turbulenzstruktur. Dabei wurden mehrere Berechnungsmethoden für die Simulation turbulenter Strömungen, wie Grobstruktursimulation (*Large-eddy Simulation* - LES), nach Reynolds gemittelte Navier-Stokes–sche Methode (*Reynolds-averaged Navier-Stokes* – RANS) und die bekannteste hybride LES–RANS Methode, die sog. *Detached-eddy Simulation* – DES, eingesetzt. Eine der Zielsetzungen war auch die kritische Analyse dieser Methoden hinsichtlich ihrer Leistungsfähigkeit in solchen komplexen Strömungssituationen. Drei unterschiedliche, durch die intensive Ablösung geprägte und mit stärker werdender Komplexität der Wandgeometrie bezeichnete Strömungskonfigurationen wurden herangezogen: die Strömung über eine zurückspringende Stufe (Experiment von Yoshioka et al., 2001) bei einer niedrigen Reynoldszahl (Re_H=3,700), die Strömung über eine Serie von symmetrischen, im regelmäßigen Abstand angeordneten Hügeln bei einer moderaten Reynoldszahl, Re_H=10,595 (LES von Fröhlich et al., 2005) und die Strömung über einen nicht-symmetrischen Hügel bei einer sehr hohen Reynoldszahl von Re_c=936,000 (Exp. Greenblatt et al., 2004). Die beiden experimentell untersuchten Strömungen wurden zusätzlich durch unterschiedliche Kontrollmechanismen – stationäre Einsaugung sowie durch abwechselnde Einsaugung/Ausblasung hervorgerufene Oszillationen der separierenden Scherschicht – angeregt. Im Fall der Stufenströmung wurden mehrere, in Form der Strouhal-Zahl ausgedrückte Frequenzen der in die Stufengrenzschicht periodisch eingeführten Störung betrachtet. Die zur maximalen Verkürzung des Eckenwirbels führende Frequenz entsprach der Strouhal-Zahl von 0.19. Wie erwartet, zeigten die im Rahmen der RANS-Methode eingesetzten statistischen Turbulenzmodelle eine schwache Empfindlichkeit gegenüber der Instationarität der Strömung und verfehlten deutlich die experimentell ermittelten Ergebnisse. Im Gegensatz dazu gaben die LES und DES Berechnungen alle wichtigen Effekte der Beeinflussung der abzulösenden Scherschicht wieder. Neben einer sehr guten Übereinstimmung der numerischen und experimentellen Ergeb-

nisse im Hinblick auf die zeitlich gemittelten Strömungsfelder, zeigen Vergleiche der phasen-gemittelten Daten ebenso ein hohes Maß an Übereinstimmung. Die Ergebnisse der LES und DES Berechnungen der Strömung über einen in die Grenzschicht ohne äußeren Druckgradienten positionierten, nicht-symmetrischen Hügel resultierten in einem hohen Übereinstimungsgrad mit experimentellen Ergebnissen, trotz eines relativ groben Gitters (4 Mio. Gitterzellen) in Hinblick auf die behandelte Reynoldszahl (ca. 1 Mio.). Dies gilt sowohl für die zeitlich- als auch die phasen-gemittelten Ergebnisse. Ähnlich wie bei der Stufenströmung schnitten RANS-Modelle in keiner zufriedenstellenden Übereinstimmung mit Messungen ab. Dies ist vor allem auf die Unfähigkeit der RANS-Methode zurückzuführen, die durch die hoch-frequenten Wirbelstrukturen hervorgerufene Instationarität der separierenden Scherschicht und deren Wechselwirkung mit der Hauptströmung korrekt aufzulösen. Diese umfangreiche Studie bietet einen detaillierten Einblick in den Stand der numerischen Aktivitäten im Bereich der aktiven Kontrolle der Strömungsablösung.

Contents

Nomenclature

Latin characters

C, c	cord length
C_s	Smagorinsky constant
C_{DES}	model constant (DES)
C_f	time-mean skin-friction coefficient
$< C_f >$	phase-averaged skin-friction coefficient
C_p	time-mean pressure coefficient
$< C_p >$	phase-averaged pressure coefficient
$\hat{C}_p$	coherent part of pressure coefficient, $\hat{C}_p =< C_p > -C_p$
c_f	flap cord length
$c_{b1}, c_{b2}, c_{v1}, c_{w1}, c_{w2}$	auxiliary relations and constants of the S-A model
$\mathcal{D}_k^\nu$	molecular diffusion of k
d	distance to the closest wall
F^+	reduced frequency, $F^+ = fc_f/U_\infty$
f	frequency
f_e	perturbation frequency, $\phi = 2\pi f_e t$
f_μ	wall-damping function
f_{v1}, f_{v2}, f_w	auxiliary relations of the S-A model
g	auxiliary relation of the S-A model
H, h	height of channel, hill, step
k	kinetic energy of turbulence
L	integral length scale
l	characteristic length scale
L_x, L_y, L_z	computational box size in x, y and z direction
N_{grid}	number of grid points
N_x, N_y, N_z	number of grid cells in x, y and z direction
$\hat{p}$	instantaneous pressure
p, p'	time-averaged and fluctuating pressure (RANS)
$\overline{p}, p'$	filtered and fluctuating pressure (LES)
Re	Reynolds number
Re_b	Re number based on bulk velocity, $Re_b = U_b H/\nu$
Re_c	Re number based on free-stream velocity, $Re_c = U_\infty c/\nu$
Re_H, Re_h	Re number based on step height
Re_τ	Re number based on friction velocity, $Re_\tau = u_\tau H/\nu$
Re_θ	Re number based on momentum thickness, $Re_\theta = U_\infty \theta/\nu$
r	radius, auxiliary relation of the S-A model
S	magnitude of vorticity

$\tilde{S}$	auxiliary relation of the S-A model
$\overline{S}_{ij}$	filtered rate of strain tensor, $\overline{S}_{ij} = \frac{1}{2}(\frac{\partial \overline{u}_i}{\partial x_j} + \frac{\partial \overline{u}_j}{\partial x_i})$
$\lvert\overline{S}\rvert$	characteristic rate of strain, $\lvert\overline{S}\rvert = \sqrt{2\overline{S}_{ij}\overline{S}_{ij}}$
St	Strouhal number, $St = f_e H/U_c$
$t, \Delta t$	time, time step
U, u	streamwise velocity
U_b	bulk velocity
U_c	centerline velocity
U_{cv}, U_{con}	convective velocity
U_∞	free-stream velocity
$\hat{u}_i$	instantaneous velocity field
$u_i, {u_i}'$	time-averaged and fluctuating velocity field (RANS)
$\overline{u}_i, {u_i}'$	filtered and residual velocity field (LES)
${u_i}'{u_j}'$	Reynolds-stress tensor
$u'u', \overline{u}^2, uu, u^2$	streamwise Reynolds stress
$u'v', \overline{u'v'}, uv$	Reynolds shear stress component
u_{rms}	root-mean square of streamwise velocity fluctuations
u_τ	friction velocity
V, v	wall-normal velocity
V_e, v_e	injection velocity peak, injection velocity, $v_e = V_e sin\phi$
$v'v', \overline{v}^2, vv, v^2$	wall-normal Reynolds stress
v_{rms}	root-mean square of wall-normal velocity fluctuations
$w'w'$	spanwise Reynolds stress
x, y, z	coordinate component
X_R	reattachment length
X_{R0}	reference reattachment length
y^+	non-dimensional wall distance, $y^+ = yu_\tau/\nu$

Greek characters

α	airfoil angle of attack
Δ	filter size
δ	boundary-layer thickness
ϵ	dissipation rate of k
ϵ_{hom}	homogeneous dissipation rate, $\epsilon_{hom} = \epsilon - 0.5\mathcal{D}_k^\nu$
η, η_k	Kolmogorov length scale, $\eta_k = (\nu^3/\epsilon)^{1/4}$
Φ, ϕ	phase angle
κ	constant in the S-A model, $\kappa = 0.41$
ν	molecular viscosity (kinematic)
$\tilde{\nu}$	modified turbulent viscosity (S-A model)
ν_t	turbulent viscosity
ν_{sgs}	sub-grid scale viscosity
ω	vorticity ($k-\omega$ model)
ρ	density
τ_{ij}	sub-grid stress tensor, $\tau_{ij} = \overline{u_i u_j} - \overline{u}_i \overline{u}_j$
τ_{wall}	wall shear stress
θ	momentum thickness
χ	auxiliary relation of the S-A model

Superscripts, subscripts

$+$	normalized by 'wall units' ν and u_τ
exp	experimental
int	interface
osc	oscillatory
sgs	sub-grid scale
suc	suction

Acronyms

AFC	Active Flow Control
BFS	backward-facing step
CFD	Computational Fluid Dynamics
DES	Detached-eddy Simulation
DNS	Direct Numerical Simulation
EVM	eddy viscosity model
FTT	flow-through time
GL	Gibson, Launder
HJ	Hanjalić, Jakirlić
LES	Large-eddy Simulation
LS	Launder, Sharma
MJVG	micro jet vortex generator
MPI	Message Passing Interface
N–S	Navier-Stokes
PIV	Particle Imaging Velocimeter
RANS	Reynolds-averaged Navier-Stokes
RSM	Reynolds-stress model
SA,S–A	Spalart-Allmaras
SGS	Sub-grid Scale
SIMPLE	semi-implicit method for pressure-linked equations
SM	Smagorinsky model
SMC	second moment closure
SST	Shear Stress Transport
Std	standard
TLV	two-layer, velocity-scale-based model
UAV	Unmanned Air Vehicle
URANS	Unsteady Reynolds-averaged Navier-Stokes
ZNMF	zero-net-mass flow
ZPG	zero-pressure gradient

1 Introduction

One of the most important tasks in the fluid mechanics research, in general, is to control turbulent flow evolution with respect to overall drag reduction. Flow separation, often being consequence of an adverse pressure gradient, is certainly one of the main flow phenomena contributing to increased pressure losses. Therefore, separation delay and resulting separation zone shortening are of great interest in a number of industrial branches, e.g. turbomachinery, car and aircraft aerodynamics, etc. Although the passive flow control devices like airfoil vortex generators have been proven to be quite effective in delaying flow separation, under some flow conditions they may cause undesired effects, e.g. drag increase in absence of the flow separation. On the other hand, recent experimental studies have demonstrated that active flow control (AFC) has a potential to enable significant advances in many engineering applications.

There are different ways of AFC; the most common are steady flow suction and periodic flow perturbation at the natural separation point. By means of steady suction, the fluid in turbulent boundary layer on the verge of separation is removed, being replaced by the high momentum fluid from the mean flow which makes boundary layer more resistant to adverse pressure gradient and separation. Whereas steady momentum injection (blowing) is not widely used mainly due to its inefficiency, numerous experimental studies of unsteady flow control show that periodic excitation, i.e. an alternating zero-net-mass flux blowing/suction, can be more efficient than steady blowing and at least as effective as steady suction. Obvious advantage of periodic forcing is lower energy consumption in comparison to the other two methods. Oscillatory perturbation, if added into a separating turbulent boundary layer, is expected to increase turbulence level in the separated shear layer; a higher level of the shear stress implies a higher momentum transport across the shear layer and consequently shortening of the recirculation bubble. However, the underlying flow physics and different mechanisms responsible for an efficient flow control are not fully understood. One of the main questions which is to be answered is what are the optimal control parameters such as suction rate or perturbation frequency and momentum input? At present, there is no accepted theoretical model that can adequately explain or describe the effects of these leading control parameters. Knowing that experiments are time consuming and expensive, in many occasions not reliable or even not feasible at all, numerical simulations are expected to be more extensively used in near future, along with experiments, for design applications involving AFC. Computational Fluid Dynamics (CFD) can be useful tool, if used knowledgeably, for understanding and studying flow characteristics, in many cases providing quite credible predictions for real-world applications.

Reynolds-averaged Navier-Stokes (RANS) approach is the most widely used method for prediction of industrially relevant flows. The limitations of RANS tech-

nique are clearly recognized in many practical, complex flows such as the ones relevant to AFC. RANS turbulence models are usually calibrated for simple flow regimes (e.g. thin shear layers), but even the most advanced and complex RANS models are unlikely to be capable of predicting a variety of practical flows like massively separated flows. Direct Numerical Simulation (DNS) requires no modeling but resolving all space and time scales in practical flows (high Reynolds number flows) is not feasible. Large-eddy simulation (LES) has been proven to be a powerful method for prediction of the flows where RANS is deficient, however, it is far from replacing RANS as a daily design tool due to its prohibitive resolution requirements in the near-wall regions. Alternative strategies, which combine LES and RANS (hybrid LES–RANS) appear to be a compromise, which could eventually replace RANS in foreseeable future. Detached-eddy Simulation (DES) is the most known hybrid LES–RANS method which seems to be very attractive and successful in predicting massively separated flows. Recently, DES was proposed to exploit the advantages of RANS in the near-wall regions ('attached' flow) and superiority of LES in the separated regions ('detached' flow) [68, 48].

1.1 Objectives of the study

Though demonstrated experimentally, unsteady separation flow control remains a challenge for numerical simulation strategies. The main goal of the present work is a computational study of the effects of boundary-layer forcing on the mean flow and turbulence using various methods for turbulent flow computations, namely LES, DES and RANS, aiming also at mutual comparison of their features and performance in complex flow situations. The selected flow configurations involve the two recent experimental studies pertinent to AFC: periodically perturbed backward-facing step flow at a low Reynolds number (Yoshioka et al. [77, 78]) and high Reynolds number flow over a wall-mounted hump (Greenblatt et al. [22, 23]). Steady and unsteady RANS computations of these cases have been reported in literature, however, LES and DES predictions are either scarce or not available as yet. If performed on a suitable grid, DES predictions are typically expected to be superior to the ones obtained by RANS. The issues of the grid design and LES–RANS interface position in DES are investigated in various flow configurations.

1.2 Thesis outline

The introductory part of the thesis is followed by the review of previous work pertinent to turbulent flow separation control. Afterwards, turbulence modeling strategies and computer codes employed in this study are described. Implementation of the turbulence models is verified by computing a number of flow configurations. Several turbulent separated flows with increasing complexity, both in terms of geometry and flow physics, are scrutinized. LES and DES predictions for a plane channel flow are discussed in the course of inflow data generation for the subsequent backward-facing step simulations. Predictions of the two selected test cases relevant

to AFC applications are then presented. In particular, important issues in LES and DES such as an influence of subgrid-scale (SGS) modeling, boundary conditions, space and time resolution, are investigated. Computational details are discussed along with thorough comparison of CFD results with the available experimental data. Finally, concluding remarks and recommendations for future work are given.

2 Literature Survey

Flow control research dates back to the discovery of the boundary layer by Prandtl (1904), thereafter it has been extensively studied and applied, although primarily to military-related flow systems. Nowadays, the advantages of separation control application are expected to improve performance of various technologically important systems involving fluid flow such as air, land, and sea vehicles, turbomachines, diffusers etc. In particular, flow separation control can lead to prospective enhancements of airplane performance in landing and take-off regimes. This chapter presents recent developments in the field of AFC. In line with objectives of the present work, an overview of selected experimental and numerical numerical investigations relevant to flow control is given.

2.1 Experimental Investigations

The first experimental investigation of turbulent separation control in a plane asymmetric diffuser by means of periodic perturbation was performed by Obi et al. [51]. It was found that application of periodic suction/injection through a slot on the wall upstream of the separation point did not affect the time-averaged location of the boundary-layer separation, whereas a reduction of the reattachment length occurred for a certain range of the perturbation frequencies.

An experimental study of the periodically perturbed separated flow over a backward-facing step was conducted by Chun and Sung [11]. Excitations were introduced to separated flow by means of a sinusoidally oscillating jet issuing from a thin slit (1 mm wide) near the separation line. The Reynolds number based on the step height varied from $13,000$ to $33,000$, expansion ratio at the step being $2:3$. The effect of local forcing on the flow structure was investigated by altering the forcing amplitude and frequency. Small localized forcing near the separation edge enhanced the shear-layer growth rate and produced a large roll-up vortex at the separation edge. A large vortex in the shear layer gave rise to a higher rate of entrainment, which led to a reduction in the reattachment length as compared to the unforced flow. The most effective forcing frequency was found to be comparable to the shedding frequency of the separated shear layer. Chun and Sung [12] studied effects of the spanwise-varying local forcing on the same flow configuration by altering the spatially banded blocking width and the open slit distance. The effect of such a forcing on reattachment length was slight compared to the case of two-dimensional forcing.

Yoshioka et al. [76, 77, 78] performed an extensive study of periodically perturbed turbulent separated flow over a backward-facing step at $Re = 3,700$ based on the step height, with the expansion ratio of $2:3$. It was revealed that the large

scale vortices were introduced into the shear layer by the periodic perturbation [76]. According to the investigation on the phase-averaged momentum transport in terms of the phase-averaged Navier-Stokes Equation, momentum transfer across the shear layer was enhanced by the introduced vortices. The measured turbulent statistics showed that there existed an optimum frequency for the promotion of the reattachment [78]. When perturbed at the optimum frequency, $St = 0.30$ (Strouhal number based on the centerline velocity and the step height), the reattachment length was reduced by 30 %. The promotion of the flow reattachment in time-averaged flow was well correlated with the increase in the production of Reynolds shear stress [77]. The optimum-frequency perturbation increased Reynolds stress near the reattachment region. The lower-frequency ($St = 0.08$) perturbation increased Reynolds stress more then the optimum one but increase was observed downstream of the reattachment region. The region where the higher-frequency ($St = 0.30$) perturbation increased Reynolds stress was limited to the early stage of the recirculating region. The authors concluded that the change in the mean velocity field due to the organized fluid motion altered the production rate of Reynolds stress, which was a key effect of the perturbation on turbulent separated flow.

An interesting experimental study of turbulent backward-facing step flow under two-frequency forcing was conducted by Jin et al. [32]. Flow Reynolds number was Re=27,000 based on the step height. The reattachment length was found to be significantly dependent on the phase difference between the two forcing frequencies. Within a certain range of the phase difference, the reattachment length became smaller than that of the single frequency forcing.

All aforementioned experimental investigations are pertinent to low-Reynolds number flows. The following experimental works deal with AFC applications to the high Reynolds number flow configurations relevant to aircraft aerodynamics. Oscillatory blowing as a tool to delay boundary-layer separation was studied by Seifert et al. [60, 62]. They carried out experiments on a hollow, flapped NACA 0015 airfoil equipped with a two-dimensional slot over the hinge of the flap [60]. It was demonstrated that the efficiency of flapped airfoils could be greatly increased by the addition of relatively low momentum oscillations that were superimposed on a small amount of steady blowing. The enhancement of lift and concomitant reduction in drag was achieved at all angles of incidence (up to 40°) and Reynolds numbers considered ($10^5 < Re_c < 10^6$). Experiments performed on different airfoils revealed that oscillatory blowing could delay separation more effectively than the steady blowing used traditionally for this purpose [62]. The flow was found to be dependent on many parameters such as the location of the blowing slot, the steady and oscillatory momentum coefficients of the jet, the frequency of imposed oscillations and the shape of the airfoil. Optimum gains in airfoil performance were obtained at reduced frequencies, based on the flap cord ($F^+ = fc_f/U_\infty$), of an order of unity.

Seifert at. al [63] used piezoelectric actuators to excite the turbulent boundary layer upstream of separation. The actuators have proven to be effective as well as energy efficient. Application of active separation control to a small unmanned

air vehicle (UAV) was examined by Seifert et al. [61]. The results of the experiments demonstrated application of active separation control to a UAV using a self-contained perturbation system.

Control of flow separation on an unconventional symmetric airfoil using synthetic (zero-net-mass flux) jet actuators was investigated by Amitay et al. [4]. The experiments were conducted over a range of Reynolds numbers between 3.1×10^5 and 7.25×10^5. When synthetic jet control was applied near the leading edge, upstream of the separation point, the separated flow reattached completely for angles of attack upto 17.5° and partially for higher angles of attack. It was found that the momentum coefficient required to reattach the separated flow decreased as the actuator was placed closer to the separation point.

Seifert and Pack [65] investigated active flow separation control on a wall-mounted hump at high Reynolds numbers ($2.4 \times 10^6 < Re_c < 26 \times 10^6$) and a Mach number of 0.25. The Reynolds number had a negligible effect on the flow and its control. AFC using periodic excitation was found to be of similar effectiveness as steady suction and significantly more effective than steady blowing. The effect of sweep on active separation control was studied as well [66]. For the sweep angles considered (0° and 30°), it was found that the excitation had to be introduced slightly upstream of the separation region regardless of the sweep angle, as in the two-dimensional flow. The effectiveness of AFC was not reduced by mild sweep, and the effective frequencies did not change.

Tuck and Soria [74] applied AFC to a NACA 0015 airfoil using zero-net-mass flow (ZNMF) jet. The optimum frequencies for AFC to be implemented using a ZNMF jet, located at the leading edge of a NACA 0015 airfoil, were identified to be $F^+ = 0.7$ or $F^+ = 1.3$. The airfoil stall angle was mitigated from $\alpha = 10°$ to $\alpha = 18°$, resulting in a maximum lift coefficient increase of 46 % above the uncontrolled lift coefficient.

Recently, Greenblatt et al. [22, 23] studied experimentally the control of separated flow over a wall-mounted hump by means of steady suction and two-dimensional ZNMF perturbations, in order to generate a data set for a workshop aimed at validating CFD turbulence models. More details about these experiments will be given in later chapters through a detailed comparison of the computational results with the available experimental data.

Nowadays numerous studies focus on a strategy to develop AFC design tools to enable transition of AFC from the laboratory to applications [34]. Smart control of separation around the wing was demonstrated by Nishizawa et al. [49, 50]. A new smart control system to suppress flow separation around a wing model was investigated. The system comprised of a separation discriminator, an intelligent controller and a row of disturbance generators. As soon as the discriminator detected a harbinger of separation, the controller with separation control algorithm activated the generators, which simultaneously injected periodic disturbances from the leading edge. It was shown that the smart control system managed by a computer effectively delayed the occurrence of stall. Abe et al. [1] developed a micro-jet vortex generator (MJVG) in order to establish smart control system for wing separation. MJVG was found to appreciably enhance the lift performance.

Collis et al. [13] provided a perspective on the current status and future directons for AFC technology with particular emphasis on oscillatory control. Certain issues that are often neglected in studies were highlighted showing their importance or impact on the reported observations and outcomes.

2.2 Numerical Studies

Rhee and Sung [55] performed unsteady RANS simulation of locally forced separated flow over a backward-facing step. A version of the $k - \epsilon - f_\mu$ model was employed, in which the near-wall behavior without reference to distance and non-equilibrium effects in the recirculation region were incorporated. The model predictions were shown to be generally satisfactory compared to the experimental data of Chun and Sung [11]. However, the fact that a numerical simulation of an unsteady flow with RANS approach is always questionable was shown in the numerical study of Schatz and Thiele [59]. No satisfactory RANS predictions could be obtained for a two-element high-lift configuration at stall condition with separation control by periodic excitation.

Neumann and Wengle [47] investigated controlled turbulent flow over a rounded step by means of large-eddy simulation. Three variable parameters were the frequency, amplitude and position of the oscillating jet. The LES results of the turbulent flow at $Re_h = 9,100$ revealed importance of properly chosen control parameters which could lead to significant reductions of the size of the recirculating flow region. For sufficiently optimized control parameters, the backflow region could not only be reduced significantly in size, it could even disappear entirely.

Dejoan et al. [15, 14] used LES and statistical turbulence models to investigate the effects arising from the unsteady perturbation of a separated backward-facing step flow. The LES and RANS computations were reported for the optimum frequency configuration (Strouhal number of 0.2) examined experimentally by Yoshioka et al. [77]. At a global level, the computations correctly predicted the substantial reduction in the size of the recirculation zone - around 30 % relative to the length in the unperturbed flow. However, statistical models underestimated the shear stress enhancement in the separated shear layer. Comparisons reported in Jakirlić et al. [30] showed that RANS computations returned only a modest reduction in the length of recirculation region. The unsteadiness and peak shear stress in the separated shear layer could not be captured by statistical models.

RANS computations of the separated flow over a wall-mounted hump with AFC were reported by Iaccarino et al. [27] and Spall et al. [70]. The results of both the baseline and steady suction flow control cases were found to overpredict the experimentally determined reattachment length.

The flow over a hump model with no-flow control, steady suction and oscillatory control served as a test case for the 2004 CFD Validation Workshop on Synthetic Jets and Turbulent Separation Control [58]. It was discovered after the workshop that the side plates used in the tunnel caused blockage that, if not included, resulted in relatively minor, but noticeable overprediction of the pressures over most

of the hump. Overall, CFD could only qualitatively predict the flow physics. Predictions of the separation point were satisfactory, however, reattachment location was consistently overpredicted, regardless of turbulence model or method used. Inside recirculation bubble, most computations predicted velocity profiles in reasonably good agreement with experimental data, but turbulent shear stresses were underpredicted in magnitude.

Krishnan et al. [38] reported detached eddy simulation (DES) predictions of the baseline and steady suction cases. While DES predictions of the baseline configuration were encouraging, the disagreement with experimental measurements for the steady suction case was significant. Neither the pressure distribution nor the mean streamwise velocity in the separated region were predicted to similar accuracy. The relatively shallower separation as compared to the baseline configuration was found to pose a great challenge to hybrid LES–RANS methods. 2D unsteady RANS was also used to predict the case with oscillatory suction/blowing. Overall poor predictions were obtained providing impetus for further development and application of hybrid LES–RANS simulation strategies such as DES.

Recently, You et al. [79] employed LES to predict the turbulent flow separation and its control by synthetic jets over a wall-mounted hump. These computations have actually followed the present study and reproduced to a large extent its main results. Particularly encouraging is agreement among the results obtained applying different inlet boundary conditions and subgrid-scale modeling.

3 Turbulence Modeling

This chapter describes turbulence modeling strategies which are commonly used in the field of Computational Fluid Dynamics (CFD). Depending on the physical phenomena and flow configurations of interest, a proper selection of modeling approach and turbulence model itself is essential in order to achieve as accurate and reliable solutions as possible, yet at an affordable computational cost. One has to be aware not only of advantages but also of drawbacks and limitations of the computational method employed. Potential uncertainties, underlying assumptions and approximations must be kept in mind while interpreting the results of CFD calculations.

3.1 Direct Numerical Simulation (DNS)

Direct Numerical Simulation (DNS) involves the numerical solution of the equations governing the fluid flow, i.e. the Navier-Stokes (N-S) equations, without recourse to any modeling whatsoever. Assuming that the fluid density is constant, the incompressible N-S equations can be written as:

$$\frac{\partial \hat{u}_i}{\partial x_i} = 0 \tag{3.1}$$

$$\frac{\partial \hat{u}_i}{\partial t} + \frac{\partial (\hat{u}_i \hat{u}_j)}{\partial x_j} = -\frac{1}{\rho}\frac{\partial \hat{p}}{\partial x_i} + \nu \frac{\partial^2 \hat{u}_i}{\partial x_j \partial x_j} \tag{3.2}$$

where the hat denotes the instantaneous value of velocity or pressure in the continuity (3.1) and momentum (3.2) equations. This type of direct solution of the N-S equations is limited in its accuracy only by the numerical methods employed. Resolving all the time and length scales of the motions contained in the flow requires extremely high grid resolutions. In order to assure that all of the significant structures of the turbulence can be captured, the computational domain must be at least as large as the largest turbulence eddy that is comparable to the geometry scale of the problem (the integral scale, L), and must capture all of the kinetic energy dissipation that occurs on the smallest scale (the Kolmogorov scale, η). The relation between the integral and Kolmogorov scales can be expressed in terms of the Reynolds number as $L/\eta \approx Re^{3/4}$, so that the number of grid points required for the three dimensional simulations is $N_{grid} \approx Re^{9/4}$ [72]. It is well-known that DNS is limited to the flows involving relatively simple geometries and low Reynolds numbers. DNS remains a powerfull research tool that provides us with an extremely detailed description of the flow field. Indeed, it is sometimes even more practical to

accurately simulate the flow by means of DNS than to try to observe it in the experiment. Obviously, DNS is of great value for theoretical investigations and model testing.

3.2 Reynolds Averaged Navier-Stokes (RANS)

One can decompose instantaneous values of velocity and pressure $\hat{\phi}$ into average ϕ and fluctuating parts ϕ':

$$\hat{u}_i(x_i,t) = u_i(x_i,t) + u_i'(x_i,t) \tag{3.3}$$

$$\hat{p}(x_i,t) = p(x_i,t) + p'(x_i,t) \tag{3.4}$$

The time-averaging procedure results in the so-called Reynolds-averaged Navier-Stokes (RANS) equations that read:

$$\frac{\partial u_i}{dx_i} = 0 \tag{3.5}$$

$$\frac{\partial u_i}{dt} + \frac{\partial (u_i u_j)}{dx_j} = -\frac{1}{\rho}\frac{\partial p}{\partial x_i} + \nu \frac{\partial^2 u_i}{\partial x_j \partial x_j} - \frac{\partial u_i' u_j'}{\partial x_j} \tag{3.6}$$

Their form is similar to that without averaging except the last term in (3.6). The term $u_i' u_j'$ is called Reynolds stress and it is responsible for momentum transport by the turbulence. It appears as a consequence of the time-averaging operation on the N-S equations, which actually throw away all details concerning the instantaneous fluctuations. The Reynold stresses represent the information lost and must be closed before solving the RANS equations. For most engineering applications it is unnecessary to resolve details of the turbulent fluctuations, only the effects of turbulence on the mean flow are required. It is for this reason that RANS is used as a daily design tool. Currently, a variety of simpler (eddy viscosity models - EVM) and more complex RANS models (Reynolds stress transport models - RSM) is available to the CFD users. These models are calibrated for specific classes of flows and typically are deficient when the flow conditions depart from the range of calibration. Nevertheless, the RANS approach is attractive since many production-type codes exist within various industries, which can provide cost-effective solutions in many design applications. However, in numerous complex flow configurations RANS models have been applied with a limited success. One of the questions that remain open is whether RANS approach can be used in AFC applications.

3.3 Large-eddy Simulation (LES)

With regard to the computational cost, Large-eddy Simulation (LES) is a compromise between RANS and DNS. The larger three-dimensional unsteady structures

are resolved (as in DNS) whereas the effects of the smaller scale motions are modeled (as in RANS). In LES one filters (space or volume average) the N-S equations; the velocity field is decomposed into filtered (or resolved) component $\overline{u}$ and residual (or subgrid-scale, SGS) component u' :

$$\hat{u}_i(x_i,t) = \overline{u}_i(x_i,t) + u'_i(x_i,t) \tag{3.7}$$

the filtered velocity being defined by:

$$\overline{u}(x,t) = \int G(r,x)\hat{u}(x-r,t)dr \tag{3.8}$$

Upon filtering, the constant-density, incompressible N-S equations take the following form:

$$\frac{\partial \overline{u}_i}{dx_i} = 0 \tag{3.9}$$

$$\frac{\partial \overline{u}_i}{dt} + \frac{\partial(\overline{u}_i\overline{u}_j)}{dx_j} = -\frac{1}{\rho}\frac{\partial \overline{p}}{\partial x_i} + \nu\frac{\partial^2 \overline{u}_i}{\partial x_j \partial x_j} - \frac{\partial \tau_{ij}}{\partial x_j} \tag{3.10}$$

where the SGS stresses are given by:

$$\tau_{ij} = \overline{u_i u_j} - \overline{u}_i\overline{u}_j \tag{3.11}$$

This appears analogous to the RANS decomposition but important differences are that the filtered variables are function of space and time, and that the filtered residual is not zero ($\overline{u'}(x,t) \neq 0$). In most finite volume codes implicit filtering is employed, where the filter volume is actually equal to the control volume. The influence of smaller turbulent scales which can not be resolved by the computational grid needs to be modeled. The task of SGS modeling is, fortunately, not as difficult as in the case of RANS due to relatively universal character of the finer scales. Consequently, even simple models employed on the proper numerical grids can fulfill the main task of a SGS model, which is providing a proper energy cascade from larger to smaller scales.

Advantages of LES over conventional RANS are clearly recognizable if one is to tackle complex flows with pronounced vortex shedding or special influences of buoyancy, curvature, rotation or compression. Unlike RANS, LES gives access to the dominant unsteady motion so that it can be used, for example, to study aero-acoustics, or AFC by an appropriate unsteady forcing. Nowadays, the number of successfull LES applications in more complex geometries is increasing. However, in handling wall-bounded flows, LES still remains limited to the low-to-moderate Reynolds numbers. The grid density increases with $Re^{0.4}$ and $Re^{1.8}$ in regions away from a solid wall, and in near-wall regions, respectively [25]. Due to its prohibitive resolution requirements, both in space and time, it is difficult to expect that LES

will replace RANS as an industrial standard in the foreseeable future.

3.4 Hybrid LES–RANS Methods

Keeping in mind LES limitations, the only realistic solution appears to be a sort of combination of LES and RANS strategy. The numerical task of solving the LES equations is substantially the same as that of solving RANS equations. Hence, the identical forms of equations for RANS and LES (noting different meaning of variables) make it convenient to combine both approaches into a hybrid LES–RANS method. Various hybrid LES–RANS concepts that have been proposed recently can be classified as zonal or non-zonal techniques. A zonal approach implies that LES and RANS regions of the flow are defined in advance, which is often difficult to carry out for unknown flow configurations. On the other side, a non-zonal approach chooses (more or less) automatically the suitable simulation technique, thus avoiding the predefinition of RANS and LES regions of the flow. Depending on the numerical grid, a gradual transition between both methods takes place which weakens the problem of setting up an appropriate coupling strategy at the interface between RANS and LES zones.

One of the most popular hybrid LES–RANS approaches is Detached-eddy Simulation (DES) proposed by Spalart et al. [68]. A DES technique is defined as a three-dimensional unsteady numerical simulation using a single turbulence model, which functions as a SGS model in regions where the grid density is fine enough for LES, and as a RANS model elsewhere. This is a non-zonal approach, the two regions are not explicitly distinguished or coupled; there is a single velocity and model field. DES was originally conceived for wings at very high angles of attack and has been successfully applied mainly to external aerodynamic flows. The idea was to exploit the advantages of RANS in the near-wall regions ('attached' flow) and superiority of LES in the separated regions ('detached' flow).

Many hybrid LES–RANS methods are currently explored in attempt to solve the problem of wall modeling in LES, and extend its applications to practical engineering and aeronautical flows at high Reynolds numbers. A conjectured prospect on utilization of the available computing power by different computational approaches was recently presented by Hanjalić [25]. With the rapid development in computing power, hybrid methods are expected to be used more frequently. Particularly, it is realistic to expect that more advanced RANS models will be hybridized with LES in near future.

Basic approaches to turbulence modeling were outlined without going into details regarding the specific turbulence models. Simulation strategies and corresponding turbulence models employed in this study will be described within the subsequent chapter.

4 Numerical Method

Two different in–house computer codes based on the finite–volume method were used in this work to solve numerically governing equations presented in the previous chapter. The main features of the codes are briefly presented next, afterwards, the turbulence models that were implemented in the codes are described. Implementation of the models is verified by computations of the specific test cases and comparison of the results with the available reference computational data.

4.1 Computer Codes

FASTEST-3D (Flow Analysis Solving Transport Equations Simulating Turbulence) is the code used to predict majority of the flow configurations investigated in this study [17]. The code is based on a finite–volume numerical method for solving both three-dimensional filtered and Reynolds-Averaged Navier-Stokes equations on block-structured, body-fitted, non-orthogonal meshes. Block interfaces are treated in a conservative manner, consistent with the treatment of inner cell-faces. A cell–centered (collocated) variable arrangement and Cartesian vector and tensor components are used. The well-known SIMPLE algorithm is applied for coupling the velocity and pressure fields. The convective and diffusive transport of all variables is discretized by a second-order central differencing scheme, whose stability is enhanced through the so-called deferred correction approach [18]. Time discretization is accomplished by applying the 2^{nd} order implicit Crank-Nicolson method. FASTEST-3D is parallelized based on domain decomposition in space using the MPI message passing library. Message Passing Interface (MPI) is currently the most popular parallel programming model which has been accepted as a standard. The user is expected to decompose computational domain into subdomains with preferably equal number of grid cells. This enables an efficient parallel computation on PC clusters which usually contain a number of processors with the same speed and available memory.

Yet another code, FAN-3D (Flow Analysis Numerically), very similar to FASTEST-3D but originally developed for RANS calculations, was used to compute some flow configurations [53]. Unlike FASTEST-3D, it has not been designed for parallel computations, furthermore, the boundary conditions available in the code are typical for RANS applications. Therefore, FAN-3D was mainly used in order to test capability of a typical RANS code to predict some flows by LES method.

4.2 Turbulence Models

4.2.1 Smagorinsky SGS Model (LES)

In order to close the equations for the filtered velocity, a model for the subgrid-scale (SGS) stress tensor is needed. The very first and simplest SGS model was proposed by Smagorinsky in 1964 and is still widely used. It is an eddy viscosity based model, which relates the residual stresses, τ_{ij}^{sgs}, to the filtered rate of strain, $\overline{S}_{ij}$:

$$\tau_{ij}^{sgs} = -2\nu_{sgs}\overline{S}_{ij} \tag{4.1}$$

The eddy viscosity of the subgrid-scale motions, ν_{sgs}, is modeled by analogy to the Prandtl's mixing length model:

$$\nu_{sgs} = l^2|\overline{S}| = (C_s\Delta)^2|\overline{S}| \tag{4.2}$$

The characteristic length scale l is related to the filter size Δ through the Smagorinsky coefficient C_s and the velocity scale is given by $l|\overline{S}|$, where:

$$|\overline{S}| = \sqrt{2\overline{S}_{ij}\overline{S}_{ij}} \tag{4.3}$$

$$\overline{S}_{ij} = \frac{1}{2}(\frac{\partial\overline{u}_i}{\partial x_j} + \frac{\partial\overline{u}_j}{\partial x_i}) \tag{4.4}$$

The filter width is taken as the local grid size, i.e. $\Delta = (\Delta x\Delta y\Delta z)^{\frac{1}{3}}$. Altough theoretical values of $C_s \approx 0.17$ for homogeneous, isotropic turbulence can be found in the literature [54], usually smaller values are applied in LES computations of non-homogeneous and non-isotropic flows leading to improved results. $C_s = 0.1$ or even lower values, $C_s = 0.065$, are typically used for practical applications of the Smagorinsky model. The disadvantage of the model is that the coefficient C_s is actually not constant but flow-dependent. Close to solid walls ν_{sgs} has to be reduced to account for the anisotropy of the turbulence. Most often, a Van Driest damping function known from statistical models is used:

$$f_\mu = 1 - e^{\frac{-y^+}{25}} \tag{4.5}$$

The Smagorinsky model is most widely used SGS model for its simplicity. Beside the fact that the optimal values of C_s may vary with the type of flow, Reynolds number or discretization scheme, the kind of damping to be applied is a further point of uncertainty. Its drawbacks are that it is strictly dissipative and does not allow for backscatter, i.e transfer of energy from fine to coarse scales. Furthermore, it is not appropriate for simulating transition since it yields positive values of subgrid-scale turbulent viscosity even in laminar flows. In order to get rid of these limitations and deficiencies, Germano et al. [20] have proposed the dynamic procedure which

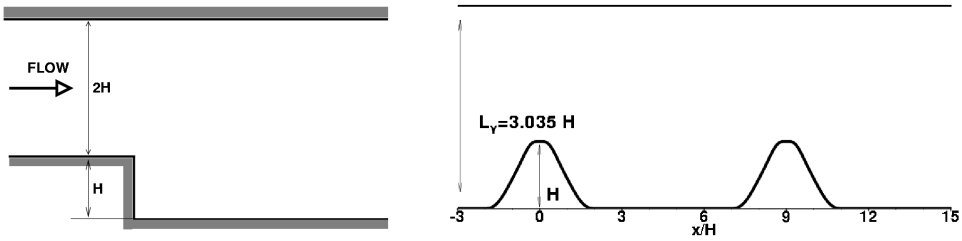

Figure 4.1: Schematics of the backward-facing step flow (left) and 2-D hill flow (right).

determines the coefficient C_s as a value changing in space and time. The parameter of the Smagorinsky model C_s is no longer required from the user but is determined by the model itself. It is automatically reduced close to walls and vanishes for well-resolved laminar flows.

4.2.1.1 Verification of the Smagorinsky Model Implementation

The standard Smagorinsky SGS model is implemented in FAN-3D code and tested on the unperturbed backward-facing step flow. The flow configuration considered corresponds to the experiment of Yoshioka et al. [77], with the channel expansion ratio of 3:2 as shown in Fig. 4.1-left. A description of the experiment along with the computational details will be subject of the later chapters. Here, the model implementation is verified by comparing LES predictions of FAN-3D to the reference results obtained by FASTEST-3D. It is important to note that the same computational domain, numerical grid and unsteady inlet boundary conditions are used in both computations. The codes employ virtually the same numerical method, the only difference pertains to the outlet boundary conditions and boundary conditions in the spanwise direction. Instead of periodic boundary condition, FAN-3D employs symmetry plane in the spanwise direction, whereas zero gradient at the outlet is applied instead of the convective outflow commonly used in LES computations. LES predictions of the mean streamwise velocities and Reynolds stresses are

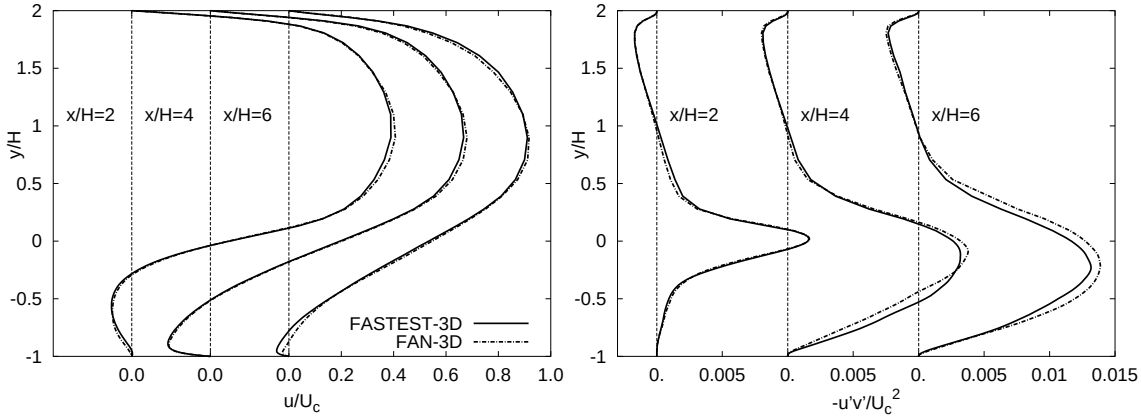

Figure 4.2: LES predictions of the backward-facing step flow; comparison of mean streamwise velocity (left) and Reynolds shear stress (right) profiles obtained by FASTEST-3D and FAN-3D.

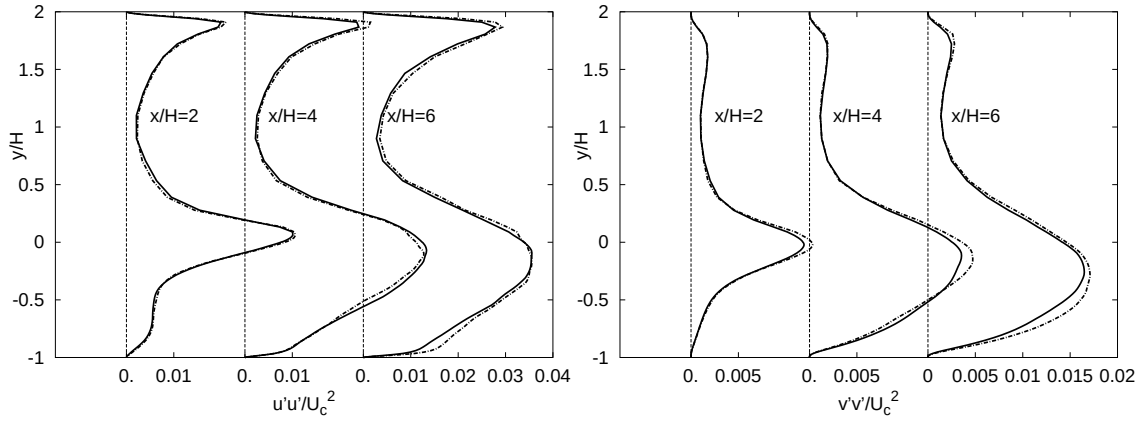

Figure 4.3: LES predictions of the backward-facing step flow; comparison of normal Reynolds stresses (u'u' and v'v') obtained by the two different codes.

compared at the three stations downstream of the step as shown in Figs 4.2 and 4.3. Interestingly, despite different boundary conditions in the spanwise direction, which could be expected to be quite influential, agreement between the two simulations is almost excellent. A small difference in backflow velocity can be observed at $x = 6H$ (Fig. 4.2-left), whereas minor discrepancies in turbulent stresses are visible at the last two stations. Influence of the exit boundary condition is not expected to be significant for the exit plane is placed 30 step heights (H) downstream of the step. Hence, these small discrepancies could be associated with different boundary conditions in the spanwise direction (spanwise computational box size was $L_z = \pi H$). Evidently, though a typical RANS code, FAN-3D is successfully applied to predict the flow over a backward-facing step by means of LES employing the standard Smagorinsky model. At least for this flow at the Reynolds number $Re = 3,700$, based on the step height and centerline velocity upstream of the step, it appears that symmetry boundary condition has a minor influence on the predictions of mean velocity and turbulence fields.

4.2.2 Spalart-Allmaras Model (RANS)

The Spalart-Allmaras (S–A) model is a one-equation RANS model designed specifically for aerospace applications involving wall-bounded flows [67]. It is usually used with fine mesh as a low Reynolds number model but it is sufficiently robust for relatively crude simulations on coarse meshes as well. It solves a transport equation for the variable $\tilde{\nu}$ which is dependent on the turbulent viscosity. The model is derived based on empiricism and arguments of Galilean invariance, dimensional analysis and dependence on molecular viscosity. It includes a wall destruction term which reduces the turbulent viscosity in the laminar sub-layer and trip terms to provide smooth transition to turbulence. The trip terms are not used in the present investigations and are therefore not included in the model. The transport equation for the working variable $\tilde{\nu}$ is written as:

$$\frac{D\tilde{\nu}}{Dt} = c_{b1}\tilde{S}\tilde{\nu} + \frac{1}{\sigma_{\tilde{\nu}}}\left[\frac{\partial}{\partial x_j}\left((\nu+\tilde{\nu})\frac{\partial\tilde{\nu}}{\partial x_j}\right)\right] + \frac{c_{b2}}{\sigma_{\tilde{\nu}}}\left(\frac{\partial\tilde{\nu}}{\partial x_j}\right)^2 - c_{w1}f_w\frac{\tilde{\nu}}{d^2} \tag{4.6}$$

The auxiliary relations are functions of $\tilde{\nu}$ and velocity gradients:

$$\nu_t = \tilde{\nu} f_{v1}, \qquad f_{v1} = \frac{\chi^3}{\chi^3 + c_{v1}^3}, \qquad , \qquad \chi = \frac{\tilde{\nu}}{\nu} \tag{4.7}$$

$$\tilde{S} = S + \frac{\tilde{\nu}}{\kappa^2 d^2} f_{v2}, \qquad f_{v2} = 1 - \frac{\chi}{1 + \chi f_{v1}} \tag{4.8}$$

$$f_w = \left[\frac{1 + c_{w3}^6}{g^6 + c_{w3}^6} \right]^{1/6}, \qquad g = r + c_{w2}(r^6 - r), \qquad r = \frac{\tilde{\nu}}{\tilde{S} \kappa^2 d^2} \tag{4.9}$$

where S is the magnitude of vorticity, and d is the distance to the closest wall. The wall boundary condition is $\tilde{\nu} = 0$ and the model constants are: $c_{b1} = 0.135$, $\sigma = 2/3$, $c_{b2} = 0.622$, $\kappa = 0.41$, $c_{w1} = c_{b1}/\kappa^2 + (1 + c_{b2})/\sigma$, $c_{w2} = 0.3$, $c_{w3} = 2$ and $c_{v1} = 7.1$. The S–A model has been calibrated on 2-D mixing layers, wakes and flat-plate boundary layers. It yields very good predictions of boundary layers in pressure gradients.

4.2.2.1 Verification of the S–A Model Implementation

The S–A model is implemented in both FAN-3D and FASTEST-3D. Implementations are verified by computing the backward-facing step flow mentioned previously, and separated flow in a channel with streamwise periodic constrictions. Both flow configurations served as test cases at the 9^{th} ERCOFTAC workshop on refined turbulence modeling [30].

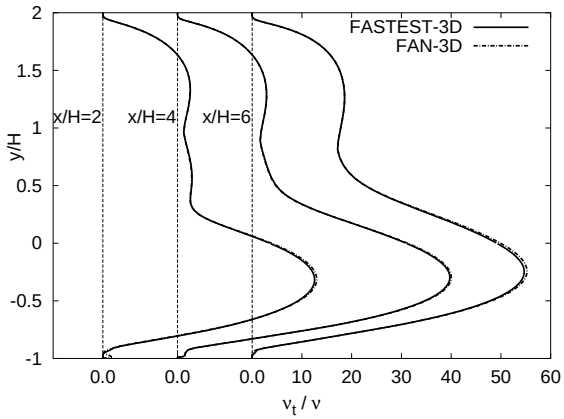

Figure 4.4: Turbulent viscosity distributions for the backward-facing step flow obtained by FASTEST-3D and FAN-3D employing the S–A model.

Turbulent viscosity predictions of the backward-facing step flow obtained by FASTEST-3D and FAN-3D codes employing the S–A model are presented in Fig. 4.4. These steady 2D-RANS computations are performed employing the same turbulence model, numerical grid and boundary conditions. It can be seen that both codes produce practically the same results. In order to verify the model implementation,

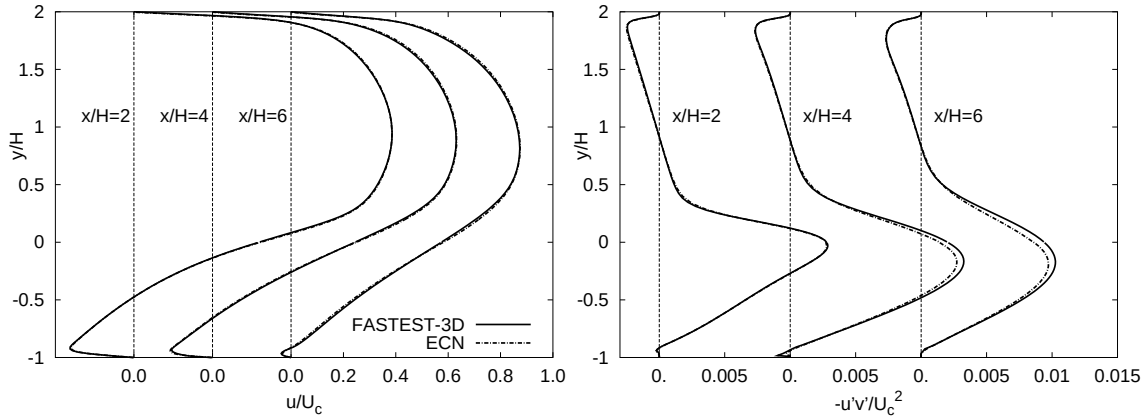

Figure 4.5: Streamwise velocity (left) and Reynolds shear stress (right) predictions of the backward-facing step flow; comparison with the reference computations of ECN, Nantes [30]

the FASTEST-3D results are compared to the computational data of Queutey (Ecole Centrale de Nantes - ECN). Details of the reference computations can be found in the authors contribution to the 9^{th} ERCOFTAC workshop on refined turbulence modeling [30]. At this point, one should note that the same test case is computed employing different codes and numerical grids. Inflow boundary conditions corresponding to a fully developed channel flow, though produced by different statistical turbulence models, are virtually the same. Comparison of streamwise velocity and Reynolds shear stress profiles is displayed in Fig. 4.5. Agreement between the two independent computations is excellent. Small deviations in shear stress at the last two stations are presumably caused by slightly different streamwise resolutions in this flow region.

The next case to be considered is separated flow in a channel with streamwise periodic constrictions. The popular 2-D hill flow was one of the test cases at both the 9^{th} and 10^{th} ERCOFTAC workshops [30, 41]. Flow separates in a channel constricted by periodically distributed hill-shaped protrusions on one wall that obstruct the channel by 33% of its height and are arranged 9 hill heights apart (Fig. 4.1-right). The Reynolds number based on the hill height and the bulk velocity above the crest is 10,595. The length of computational domain is 18 hill heights (H)and the conditions at the inlet are taken from the reference LES solution of Leschziner et al. [30, 41]. Rumsey (NASA) has performed computations of the same hill flow configuration using the S–A model. Description of the code employed and specifics of the computations can be found in the authors contribution to the 10^{th} ERCOFTAC workshop [41]. As compared to FASTEST-3D and the corresponding numerical grid, the code CFL3D with significantly different structure and numerics is employed on the grid which is about four times finer. Figs. 4.6 and 4.7 display velocity and Reynolds shear stress predictions of these two independent computations. Almost excellent agreement between the velocity and turbulence profiles is encouraging. Deviations in the normal velocity component at the first two stations arise from different applications of the model, i.e. differences in computational grid

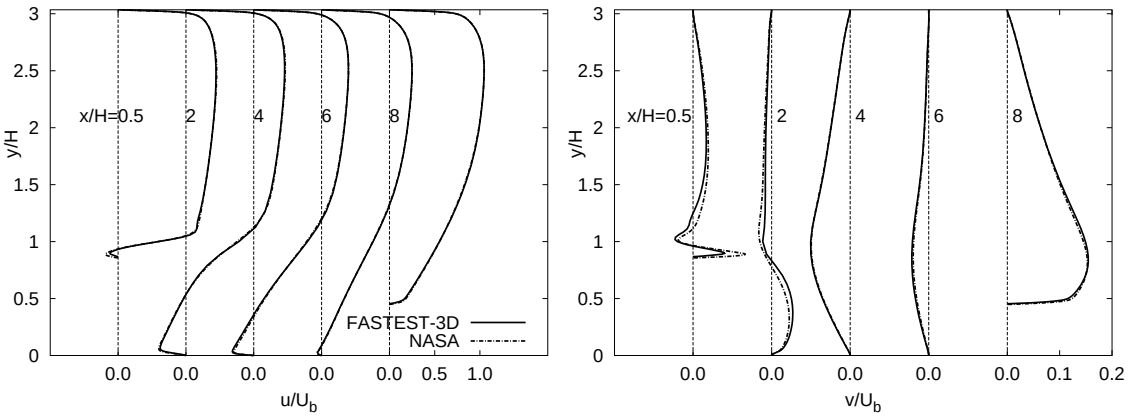

Figure 4.6: Axial (left) and normal (right) velocity profiles for the 2-D hill flow; comparison with the computations of Rumsey (NASA, Langley) [57]

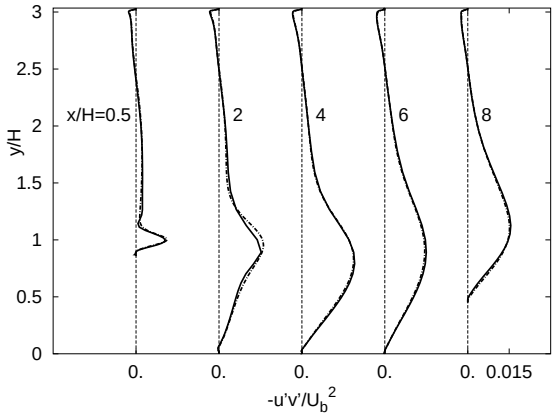

Figure 4.7: Reynolds shear stress distributions for the 2-D hill flow; comparison with the computations of Rumsey (NASA, Langley) [57]

and numerical method. The foregoing comparison of the predictions of the two flows featuring separation demonstrates reproducibility of the results, from code to code and grid to grid, obtained by the S–A model.

4.2.3 Detached-eddy Simulation (Hybrid LES–RANS)

The S–A turbulence model is employed in this study to model influence of the smallest, unresolved scales on the resolved ones in the framework of the detached-eddy simulation (DES) computational scheme [68]. It is recalled that the S–A RANS model determines the modified turbulent viscosity ($\tilde{\nu}$) from the corresponding transport equation, whose destruction term ($-c_{w1} f_w \frac{\tilde{\nu}}{d^2}$) is modelled in terms of the distance to the nearest wall. The DES formulation is obtained by replacing the wall distance by $\tilde{d}$, which is defined as:

$$\tilde{d} = min(d, C_{DES}\Delta_{DES}) \tag{4.10}$$

where a somewhat modified length scale ('a DES filter') valid in the 'LES part' of the flow field is introduced as $\Delta_{DES} = max(\Delta x \Delta y \Delta z)$. This modification of the destruction term in Eq. (4.6) tunes the model to function in a RANS mode in near-wall regions ('attached' boundary layers), whereas away from the walls, in 'detached' regions of the flow, the closure reduces to a (one-equation) Smagorinsky-like model for the SGS eddy viscosity. The original value of the corresponding model constant $C_{DES} = 0.65$ is used in the present work.

Motivated by the excessive LES cost in boundary layers and poor RANS accuracy after separation, DES has been conceived to tackle separated flows at high Reynolds numbers. It is the most widely used hybrid LES–RANS method with increasing number of successful applications, particularly in complex vortical and massively separated flows. However, the issues of grid design and position of the LES–RANS interface remain a point of interest in DES.

4.2.3.1 DES of the 2-D Hill Flow

Upon the aforementioned modification of the S–A model, DES of 2-D hill flow is performed. Results can then be compared to the computational data of Breuer (LSTM Erlangen) who obtained DES predictions for the same flow configuration with the curvilinear finite-volume LESOCC code [75]. Since the same computational grid and boundary conditions are used in both simulations, it is not only possible to verify model implementation but also to investigate code dependence. Figs 4.8 to 4.10 compare DES predictions of the hill flow configuration obtained by FASTEST-3D and LESOCC. The profiles of mean streamwise and normal velocities show excellent agreement. The same holds for Reynolds stress and turbulence kinetic energy distributions noting that minor deviations may have resulted due to differences in numerical methods applied and integration times used to obtain the flow statistics.

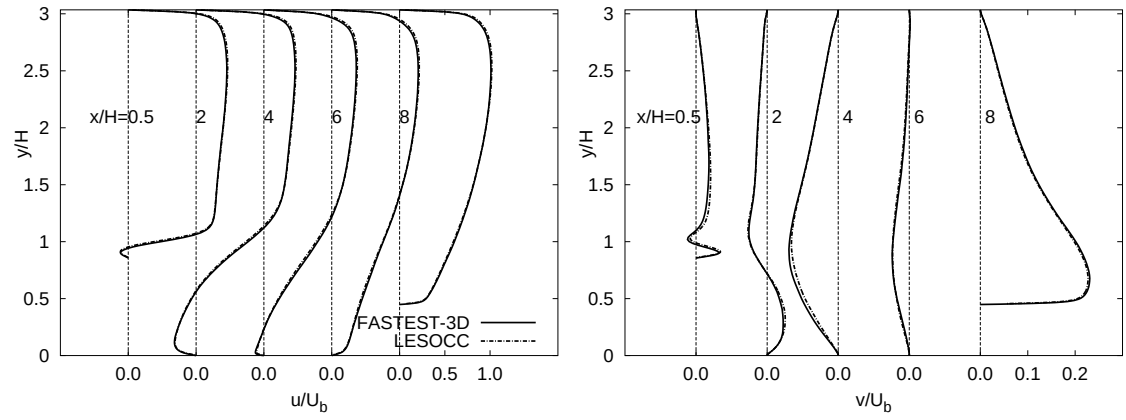

Figure 4.8: Mean streamwise (left) and normal (right) velocity profiles for the 2-D hill flow; comparison with the DES results of Breuer (LSTM Erlangen) [8]

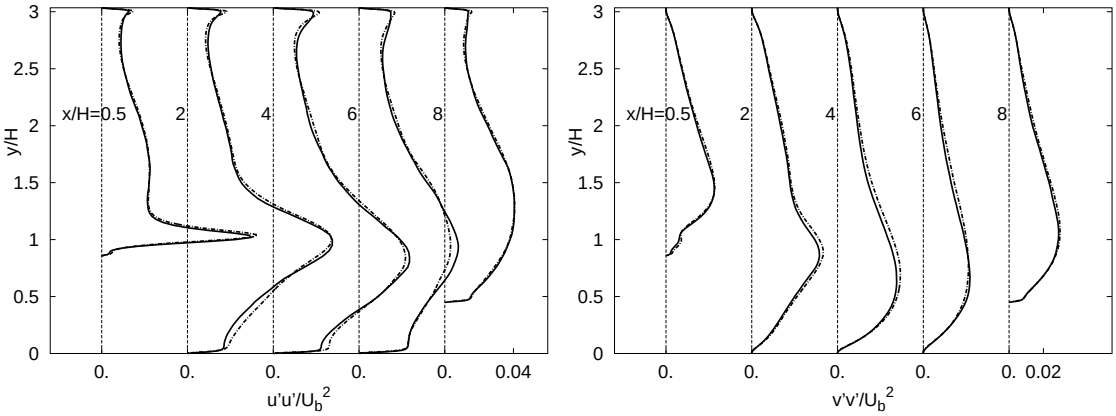

Figure 4.9: Normal Reynolds stress u'u' (left) and v'v' (right) profiles for the 2-D hill flow; comparison with the DES results of Breuer (LSTM Erlangen) [8]

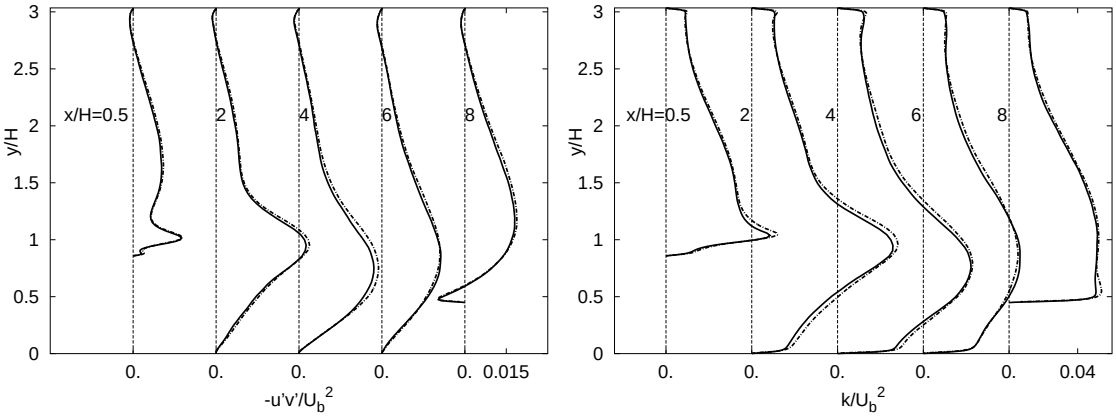

Figure 4.10: Reynolds shear stress (left) and turbulent kinetic energy (right) predictions of the 2-D hill flow; comparison with the DES results of Breuer [8]

It is interesting to see the performance of the S–A model in two different computational frameworks; RANS vs. DES. Breuer [8] has recently reported a highly resolved LES (13.6×10^6 grid cells) of the periodic hill flow, which is here used as a reference. DES of the hill flow is performed employing 960,000 grid cells ($160\times100\times60$), the size of computational domain being $9H \times 3.035H \times 4.5H$. Periodic boundary conditions are imposed in the streamwise and spanwise directions. At the walls the no-slip boundary condition is applied for the velocity and the modified turbulent viscosity $\tilde{\nu}$ is set to zero. Streamwise pressure gradient is imposed and adjusted in time to provide a target mass flow rate corresponding to the flow Reynolds number of 10,595. Evaluation of DES for predicting the flow over periodic hills will be presented in the next chapter. Without going into further computational details, DES predictions are here compared to the reference LES, and 2D-RANS results already presented in section 4.2.2.1.

Mean streamwise and normal velocity profiles are displayed in Fig. 4.11. Unlike RANS, which returns velocity distributions satisfactorily only at the first two stations, DES predictions are in very close agreement with the reference LES data,

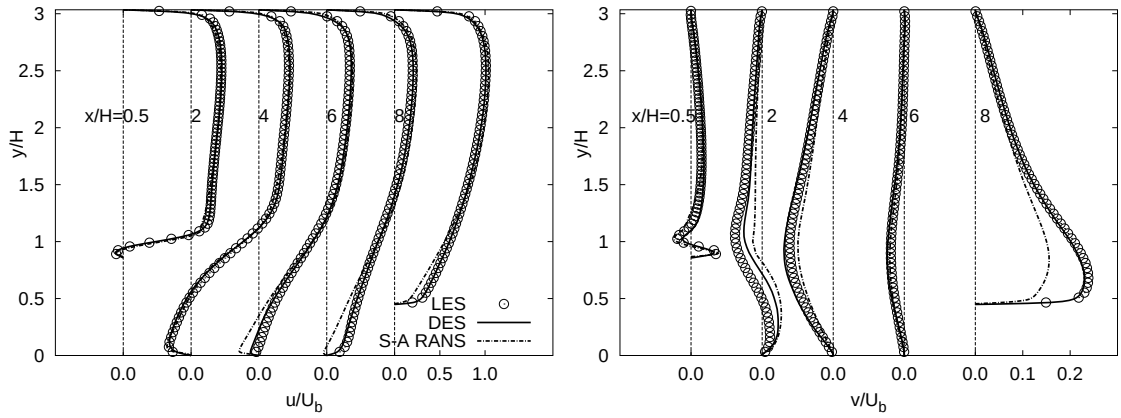

Figure 4.11: Axial (left) and normal (right) velocity profiles for the 2-D hill flow; S–A DES vs S–A RANS predictions

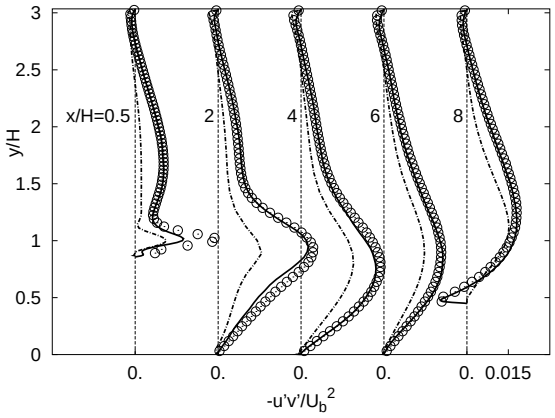

Figure 4.12: Turbulent shear stress distributions for the 2-D hill flow; S–A DES vs S–A RANS predictions

predicting also closely the location of flow reattachment. Unsteadiness of the large scales in the separated shear layer is captured by DES as shown in Fig. 4.12. Except at the first station, DES yields the correct level of turbulent shear stress, and therefore mixing, in the separated shear layer which is crucial for capturing the reattachment location. However, DES overpredicts the flow reattachment at $5.12H$ as compared to the reference value of $4.69H$ (LES). This could be explained by inadequate resolution in the shear layer just after separation, which is responsible for underprediction of the shear stress peak at the first station ($x = 0.5H$).
Flow structures can be discerned in Fig. 4.13 which displays a three-dimensional isosurface plot of the instantaneous pressure fluctuation p'. Organized vortical activity in the hill flow can be observed, consistent with LES treatment of the largest portion of the computational domain. Near-wall region of the flow treated by RANS includes 7-9 cells in the wall-normal direction at the lower wall, and 4-5 cells at the upper wall. This flow configuration features separation from a curved surface with the strong spatial and temporal fluctuation of the separation line. Hence, it is possible to distinguish attached boundary layer and separated flow regions only

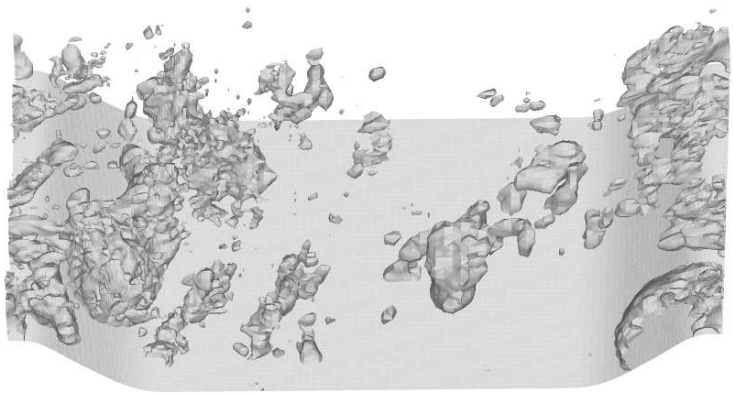

Figure 4.13: Visualization of coherent flow structures in DES of the hill flow: isosurface of the instantaneous pressure fluctuation p'.

in the time-averaged sense. Such an internally separated flow may seem not to be attractive for DES that, as a hybrid LES–RANS method, relies on the RANS model in predicting the location of boundary-layer separation. Leschziner [41] observed that in LES even slight changes in the time-averaged location of the separation line result in substantial changes in the reattachment behavior (the ratio being around 1:7). The RANS solutions indicate this sensitivity as well, albeit less distinctly. Nevertheless, knowing that generally all RANS models perform poorly in this flow, it is challenging to test the capability of DES to predict the periodic hill flow, yet at an affordable computational cost. Compared to the reference parallel computation (LES employing 13.6×10^6 grid cells) DES is performed on a 14 times coarser grid using a single PC. Recall that the S–A RANS model captures boundary layer separation closely ($0.18H$, reference value being $0.19H$) but fails to predict the flow reattachment at all. On the other hand, DES predicts recirculation bubble and main flow quantities close to the reference LES results. It is shown, for the considered hill flow configuration, that DES can produce results comparable to the ones obtained by LES, but employing substantially coarser space and time resolution.

Implementation of turbulence models used in the framework of LES, RANS and DES was verified by computing the two geometrically simple, but complex flow configurations involving separation from a fixed point (backward-facing step) and separation from a curved surface (periodic hill flow). The flows feature separation, recirculation, reattachment, recovery and strong acceleration within the statistically homogeneous spanwise domain. Close agreement between the results obtained by the independent simulations is encouraging indicating a high level of fidelity of the predictions obtained by the codes. Finally, FASTEST-3D and FAN-3D codes were validated by applying DES and LES to the turbulent separated flows.

5 Prediction of Separated Flows

This chapter tends to scrutinize some generic turbulent separated flows with emphasis on the flow physics and predictive capability of various CFD strategies. Predictions of the flows featuring increasingly complex separation phenomenon will be evaluated. Despite relatively simple flow geometries, the separation process and its complexity is strongly affected by geometry of the surfaces where the flow detaches. Only the baseline cases (without any flow control) are investigated here in order to provide an insight in the flow physics and identify some issues which may be important for successful computations when tackling the same configurations with flow control.

5.1 Separated Flow over a Backward-facing Step

Due to its geometrical simplicity, separated flow over a backward-facing step is most often selected as a starting benchmark for testing turbulence models. Separation point is fixed by the geometry, yet this flow is quite complex featuring different flow regimes (boundary layers, separated shear layer, flow reattachment and recovery) in the presence of a strong adverse pressure gradient. The simulated flow configuration corresponds to already mentioned experiment conducted by Yoshioka et al. [76, 77, 78]. Some details and description of the experimentally studied backward-facing step flow will be presented later in the following chapter. Accordingly, the computational method along with features of the performed simulations will be discussed thoroughly.

Two dimensional, steady RANS computations considered in the comparison that follows were performed using the one-equation model by Spalart and Allmaras (S-A, [67]) and $k-\omega$ SST model due to Menter [45]), the two most popular statistical turbulence models in aerodynamics, both allowing integration to the wall. Additional results are available from the 9^{th} ERCOFTAC workshop [30], where this experimental configuration served as one of the test cases. The aforementioned RANS results are representative of the predictions obtained by the variety of statistical models noting that the workshop results exhibited a certain scatter and are probably not suitable for a very detailed comparison.

RANS calculations have been performed on the computational meshes which are demonstrably adequate to provide essentially grid-independent solutions. Details about the $k-\omega$ SST computations can be found in the Queutey (Ecole Centrale de Nantes - ECN) contribution to the 9^{th} ERCOFTAC workshop on refined turbulence modeling [30]. The unsteady computations are summarized in Table 5.1 showing the main parameters of the performed large-eddy and detached-eddy simulations of a backward-facing step flow. The computational domain adopted behind the step

Table 5.1: Backward-facing step computations (unperturbed flow)

Run	$\frac{L_z}{H}$	$\frac{\Delta t U_c}{H}$	Δx^+	Δy^+ $\frac{min}{max}$	Δz^+ $\frac{min}{max}$
$LES - 220 \times 82 \times 32$	π	0.047	$\frac{14}{107}$	$\frac{0.14}{37.7}$	18.5
$DES - 142 \times 82 \times 16$	π	0.047	$\frac{25}{115}$	$\frac{0.14}{37.7}$	37

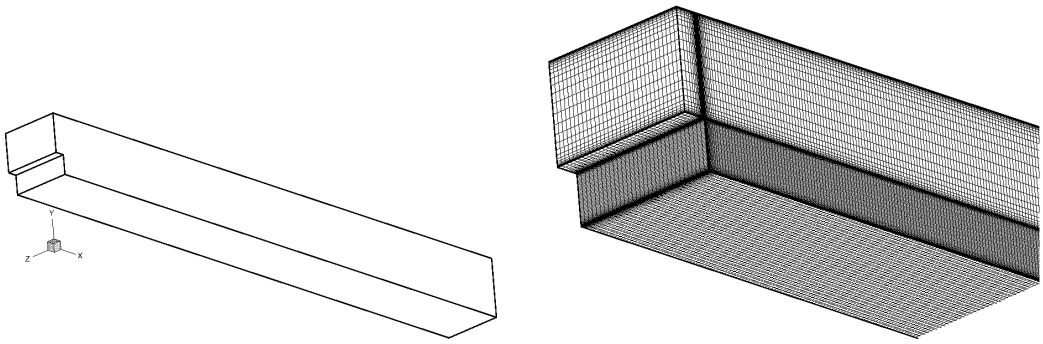

Figure 5.1: Separated flow over a backward-facing step. Computational domain and grid around the step.

($L_x \times L_y \times L_z = 30H \times 3H \times \pi H$) and a blow-up of the mesh are shown in Fig. 5.1. The instantaneous inflow velocity profiles (obtained by a separate LES of a fully developed channel flow) were imposed just upstream of the step at $L_i = -0.5H$.

Mean velocity and turbulence profiles are compared in Figs. 5.2 and 5.4. The predicted reattachment points lie around $x/H = 7$ being considerably larger than the measured value $X_R/H = 6.0$ (this value represents a corrected value, Obi [52]); the originally reported value corresponds to $X_R/H = 5.5$, Yoshioka et al., [77, 78]). Regarding the experimental configuration, particularly important is the aspect ratio based on the channel height after expansion ($3H$) and its spanwise dimension, which was only $1 : 4$. This is regarded as too short for providing a 2-D flow in the mid-span plane. Hence, the side walls might have contaminated the experimental results. For example, Kasagi and Matsunaga [35] performed experiment at a comparable Reynolds number ($Re_H = 5,540$) for the same expansion ratio. However, the above-mentioned aspect ratio was $1 : 6.7$ and, consequently, the reattachment length was substantially larger ($X_R/H = 6.51$). In favor of the computational results obtained here is the LES of the same case performed by Dejoan and Leschziner [15] who reported the reattachment length of $X_R/H = 7.0$. Discrepancies in the back-

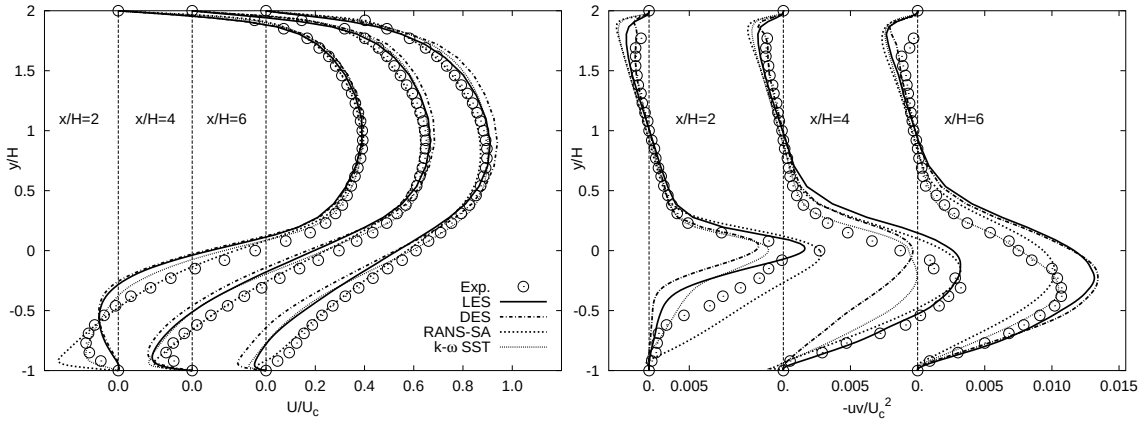

Figure 5.2: LES and DES vs. statistical models of turbulence: streamwise velocity and shear stress profiles (unperturbed flow over a backward-facing step)

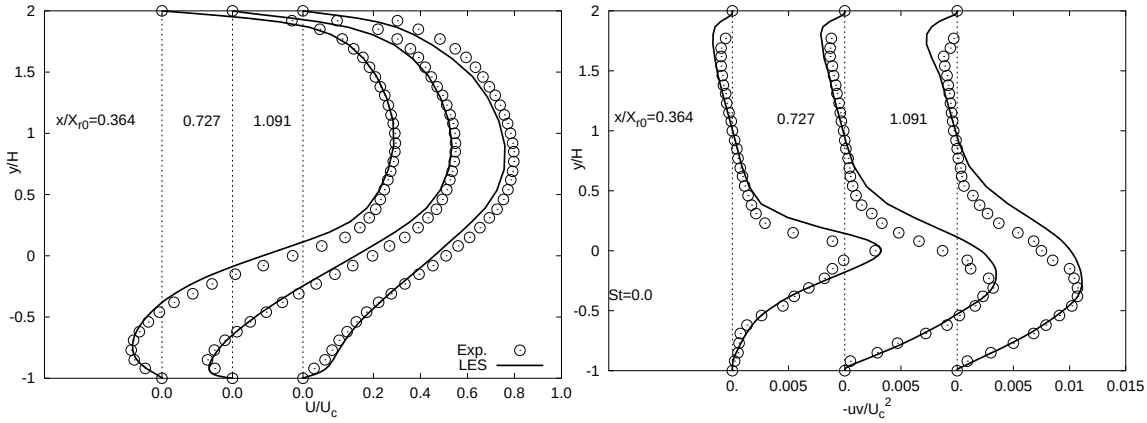

Figure 5.3: LES predictions of the mean streamwise velocity and shear stress at different streamwise locations x/X_{R0} (unperturbed flow over a backward-facing step)

flow velocity predictions are observed at the stations $x/H = 2$ and 6 (Fig 5.2-left). The aforementioned 3-D contamination can be compensated by somewhat different representation of the results. For instance, comparison of velocity profiles at the selected streamwise locations normalized by corresponding reattachment length (instead of step height) shows very good agreement between LES and experiment in the region of flow reversal (see Fig. 5.3-left). Shear stress profiles displayed in Fig 5.2-right agree reasonably well with the experimental data regardless of the method applied. If the same profiles obtained by LES are compared at normalized positions x/X_{R0}, almost excellent agreement with the experiment data is evident (Fig 5.3-right). Reynolds stresses obtained by LES and DES exhibit closer agreement with the measurements as compared to the $k-\omega$ SST RANS model as shown in Fig 5.4, clearly demonstrating capability of LES and DES to resolve stress anisotropy.

In summary, all computations of the baseline backward-facing step flow return an excessive reattachment. Due to possible problem of 3-D contamination in the experiment, it is not possible to reliably judge performance of the methods applied. Despite the flow complexity, a reasonable representation of the flow can be obtained

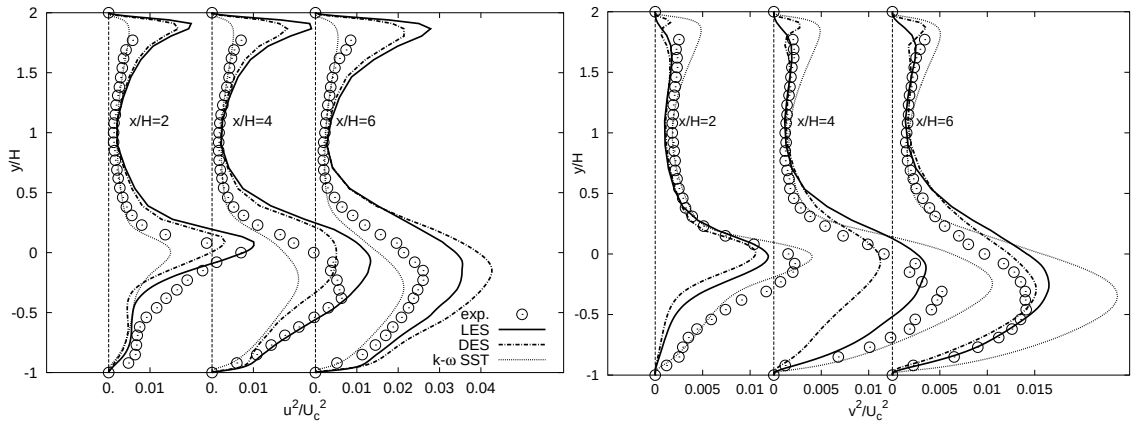

Figure 5.4: Normal stresses (streamwise and wall-normal components) predicted by LES, DES and $k-\omega$ SST RANS model (unperturbed flow over a backward-facing step)

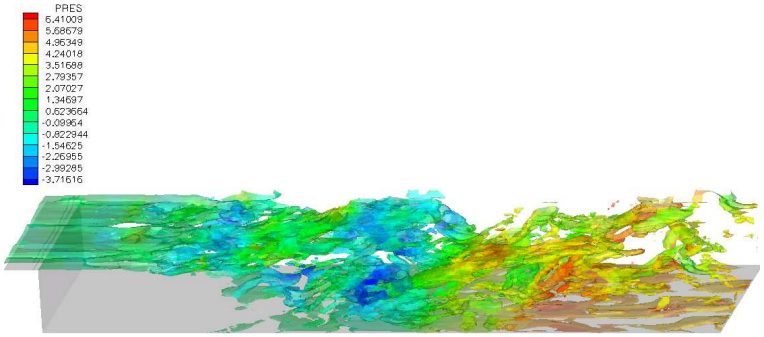

Figure 5.5: Iso-surfaces of vorticity colored by pressure obtained by LES of the unperturbed flow over a backward-facing step)

by RANS approach due to the fact that detachment of the flow is entirely determined by geometry. However, predictions of the stresses indicate that only unsteady calculations, i.e. LES and DES, can resolve the dynamics of the flow which is highly dominated by large-scale vortices. Flow topology is represented in Fig 5.5 which shows iso-surfaces of the vorticity magnitude colored by pressure coefficient. The separated shear layer, which is initially very thin and highly strained, reattaches and strongly interacts with the wall. Tendency of the flow to reorientate a spanwise vorticity field into streamwise vorticity can be observed. It is expected that the same configuration subjected to flow control will be more challenging since external forcing gives rise to modifications of coherent structures and turbulence field.

5.2 Separated Flow over a Wall-mounted Hump

The turbulent flow over a wall-mounted hump (simulating the upper surface of a Glauert-Goldschmied type airfoil at zero angle of attack) at a high Reynolds number of $Re_c = 9.36 \cdot 10^5$ (based on the free-stream velocity $U_\infty = 34.6\ m/s$ and the chord length $c = 0.42\ m$), situated in a plane channel (height $0.909c$) was

experimentally examined at the NASA Langley Research Center (Greenblatt et al. [22, 23]) for the purpose of the CFDVAL workshop on computational methods and turbulence models validation (Rumsey et al. [58]). The same test case was studied at the 11^{th} ERCOFTAC workshop on refined turbulence modeling (Johansson and Davidson [33]). Detailed description of the experimental measurements and flow control cases will be presented in the next chapter. Herein, CFD predictions of the baseline flow configuration will be evaluated. Unlike backward-facing step flow, the flow over a wall-mounted hump is characterized by much more complex separation which now occurs from a smooth surface. A blow-up of the computational grid with the geometry of the hump model are displayed in Fig 5.6. The approaching boundary layer accelerates as it is subjected to a strong favorable pressure gradient over the hump fore-body. The flow separates in the region of strong convex curvature at x/c $\approx$ 0.67, separation bubble is formed over the concave ramp of the hump, and reattachment occurs just downstream of the trailing edge at x/c $\approx$ 1.1. Time-averaged streamlines obtained by LES (see Fig 5.7) illustrate the baseline flow field in the region of separation.

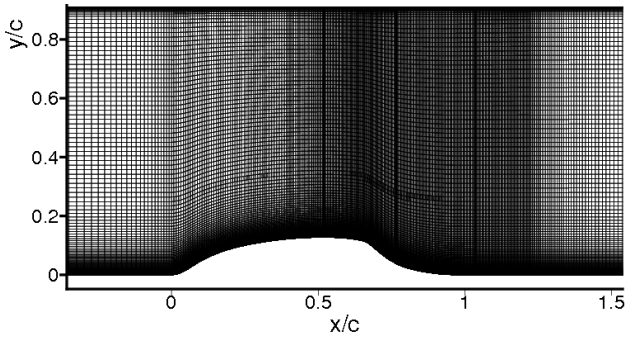

Figure 5.6: Blow-up of the grid (x-y plane) used for the 2d-hump computations

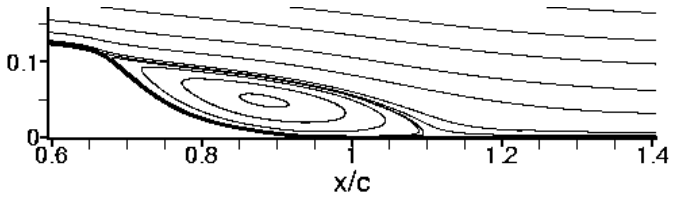

Figure 5.7: Time-averaged streamlines obtained by LES of the baseline flow over a wall-mounted hump

The solution domain for the hump geometry (dimensions: $6.14C \times 0.91C \times 0.152C$) was meshed with almost 4 Mio. ($426 \times 145 \times 64$) grid cells for LES computations, while the domain for DES with somewhat larger spanwise dimension ($0.2C$), was meshed by approximately 1.7 Mio. ($426 \times 145 \times 28$) grid cells. RANS computations have not shown significant difference in solutions obtained if the computational domain was extended further upstream ($6.39C$) as in the experiment. Furthermore, it has been demonstrated experimentally that the flow is insensitive to the upstream

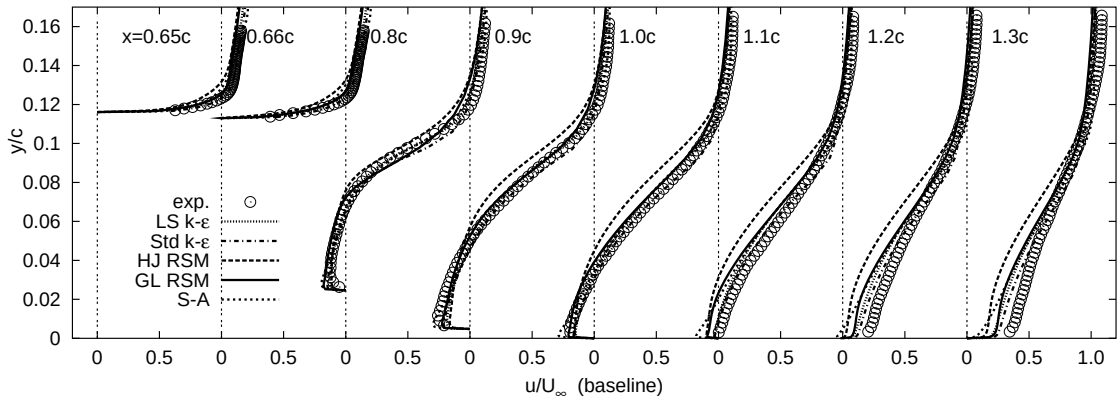

Figure 5.8: Mean streamwise velocity

boundary conditions. Therefore, in all LES and DES computations available steady profiles (the mean experimental velocity profiles) were imposed at the inlet plane placed at $2.14C$ upstream of the hump leading edge. The focus region, just downstream of the slot including the region around reattachment, was meshed to provide the wall-unit resolution of $\Delta x^+ = 80, \Delta y^+ = 1 - 80$ and $\Delta z^+ = 150$ (maximum values for DES grid). Compared to DES, LES resolution in the spanwise direction was finer providing $\Delta z^+ = 50$.

Comparison that follows includes 2D-RANS results obtained on the grids of size 426×145 and 422×75 for the low-Re and high-Re model calculations, respectively. Various statistical turbulence models were examined including the standard high-Reynolds number $k-\varepsilon$ model and its near-wall adaptation due to Launder and Sharma (LS $k-\varepsilon$ [39]) as well as the low-Reynolds number Reynolds-stress model developed by Hanjalić and Jakirlić (HJ RSM [24]) employing the homogeneous part of the total viscous dissipation rate as a scale-supplying variable (Jakirlić and Hanjalić [29]) and its high-Reynolds number asymptote due to Gibson and Launder (GL RSM [21]). The Reynolds-stress model computations require more elaborated profiles of all turbulence quantities including dissipation rate of the turbulent kinetic energy at the inlet cross-section (note that only the profiles of mean velocity and streamwise stress component are available from the reference experiment). For this purpose, the inflow data were generated by carrying out a separate computation of the zero-pressure gradient (ZPG) boundary layer with the same free-stream velocity $U_\infty = 34.6\ m/s$, using the near-wall second-moment closure model by Hanjalić and Jakirlić (HJ low-Re SMC). Finally, in all RANS computations the generated inflow velocity and turbulence profiles were imposed at the inlet plane of the solution domain. RANS predictions of streamwise velocity are compared in Fig. 5.8 with the measurements at eight positions: $x/c = 0.65, 0.66, 0.8, 0.9, 1.0, 1.1, 1.2$ and 1.3 During the initial phase of flow reversal up to $x/c = 0.8$ (about 90% of the entire geometry expansion occurs up to this length) a strong adverse-pressure gradient dominates the flow. This fact is responsible for the good agreement of the mean velocity profiles at $x/c = 0.8$ with respect to both the intensity of back flow and the thickness of separation zone, despite the poor prediction of the shear stresses shown

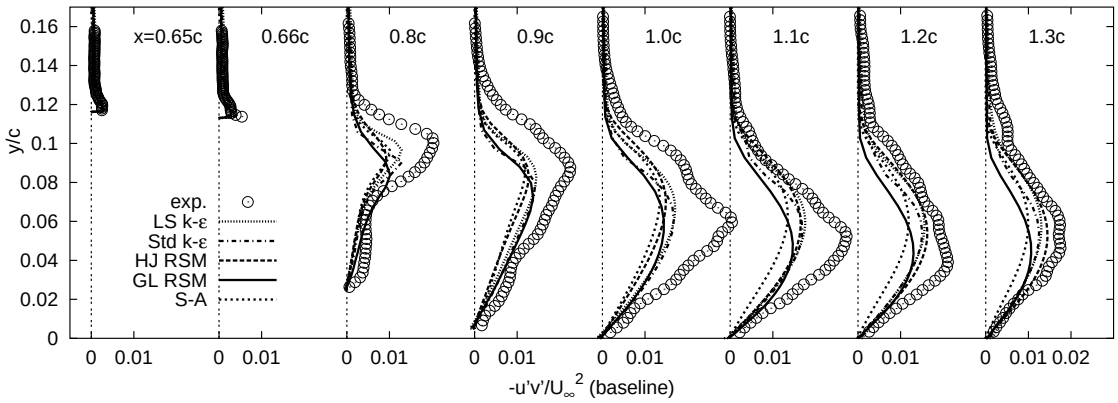

Figure 5.9: Shear stress profiles

Table 5.2: Separation and reattachment locations

		$(x/c)_S$	$(x/c)_R$
Baseline	Exp.	0.673	1.110
	LES	0.667	1.114
	DES	0.663	1.121
	S-A	0.667	1.259
	Std. $k-\epsilon$	0.672	1.125
	LS $k-\epsilon$	0.670	1.125
	GL RSM	0.670	1.158
	HJ RSM	0.660	1.195

in Fig. 5.9. Further downstream at $x/c = 1.1$ the shear-stress gradient overweighs significantly the mean pressure gradient in the momentum equation. A fairly weak gradient of the shear stress components at this location, as a consequence of a generally low shear-stress level in the shear layer being aligned with the mean dividing streamline, causes a longer recirculation region. The latter is a typical outcome of the RANS method, with a fairly weak dependence on the modeling level adopted. All models capture separation point correctly but the reattachment location is overpredicted downstream of the experimental value of $x/c = 1.1$ as summarized in Table 5.2. As far as these gross flow parameters are concerned, it is interesting to note exceptionally good performance of both $k-\varepsilon$ models. This happens to be fortuitous, presumably due to the correct level of the wall-normal stress as shown in Fig. 5.10, which appears to influence the flow reattachment significantly. However, downstream of the reattachment RANS underpredicts the level of turbulence resulting in too slow recovery. By closer inspection of Figs. 5.10 and 5.11, one can see that stress anisotropy is reproduced only to a certain extent by the Reynolds stress transport models. Still, the level of turbulence is insufficient, all RANS predictions being far from capturing the peak values (and their positions with respect to the wall) of streamwise and shear stresses in the separated shear layer. Unlike 2D-RANS, LES and DES return much better flow representation and close agreement with the ex-

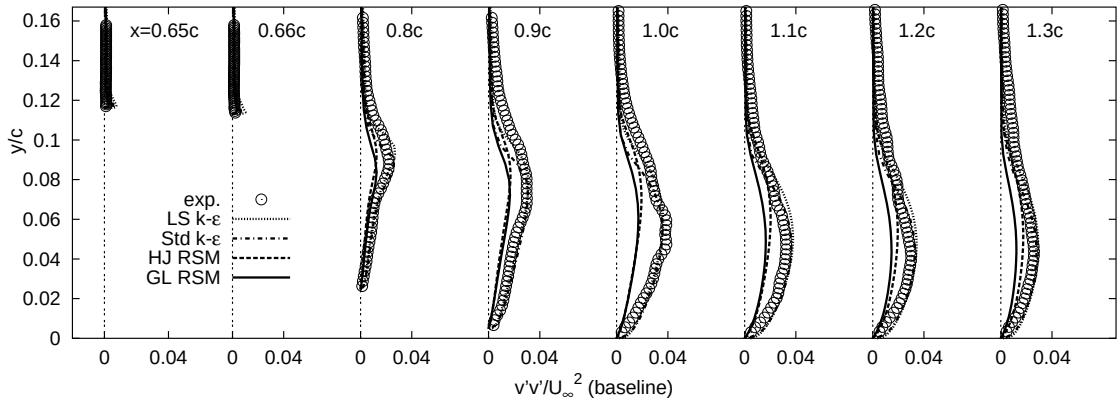

Figure 5.10: Wall-normal stress profiles

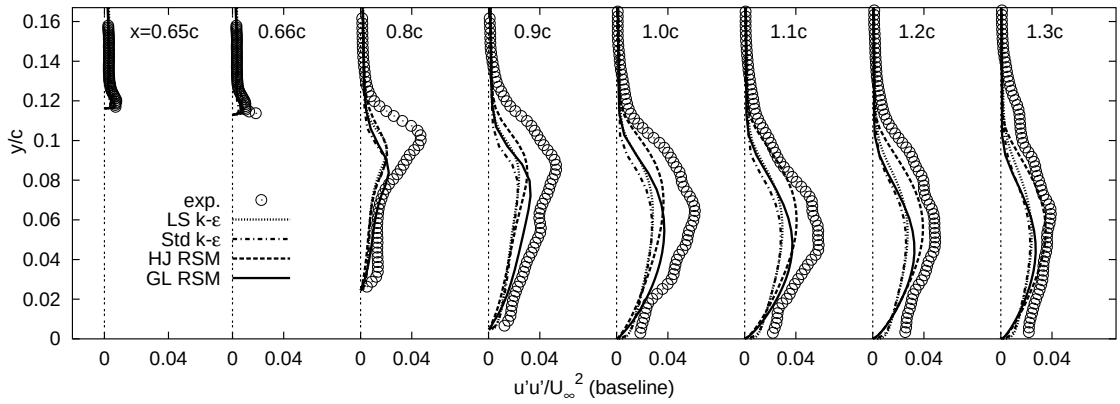

Figure 5.11: Streamwise stress profiles

perimental data. Streamwise velocity profiles obtained by LES and DES are plotted in Fig 5.12 showing that separation and reattachment, but also flow representation within the recirculating region, are captured correctly. It is interesting to see that DES predictions are even better than the ones obtained by the conventional LES (see also the shear stress profiles in Fig. 5.13). Feasibility of the DES as a hybrid LES–RANS approach (designed to operate as the RANS method within attached boundary layers and the LES method in detached, separated regions of the flow) is further expressed through the fact, that these results were obtained using a coarser grid (1.7 Mio. in total vs. 4 Mio. for LES). The Reynolds shear stress evolution presented in Fig. 5.13 demonstrates how crucial it is to capture the level of turbulence in separated shear layers with respect to the mean flow features downstream, especially to the reattachment location. The correct LES and DES predictions of the shear stress in the region aligned with the mean dividing streamline lead to the accurate reattachment length. Noteworthy is a close agreement of the wall-normal stresses with the reference data as demonstrated in Fig 5.14. Finally, due to the correct turbulence level in the near-wall region, LES and DES yield an excellent representation of flow recovery downstream of the reattachment.

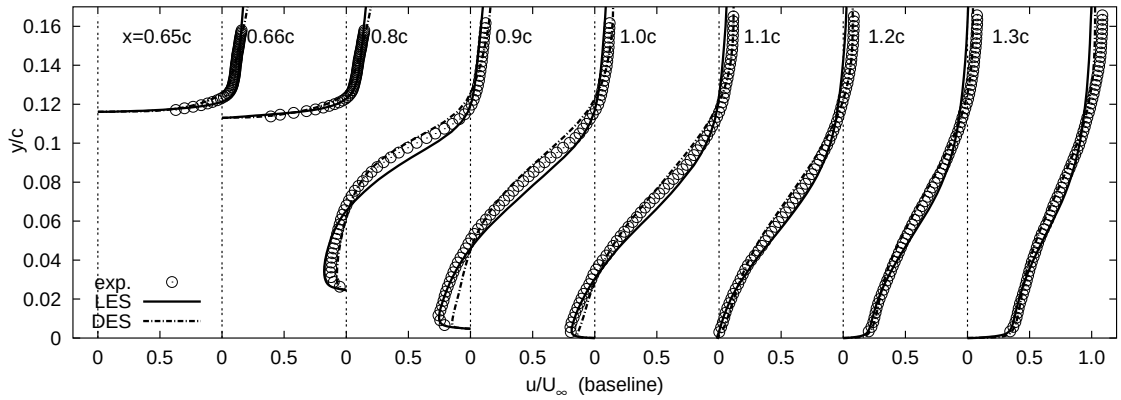

Figure 5.12: Mean streamwise velocity

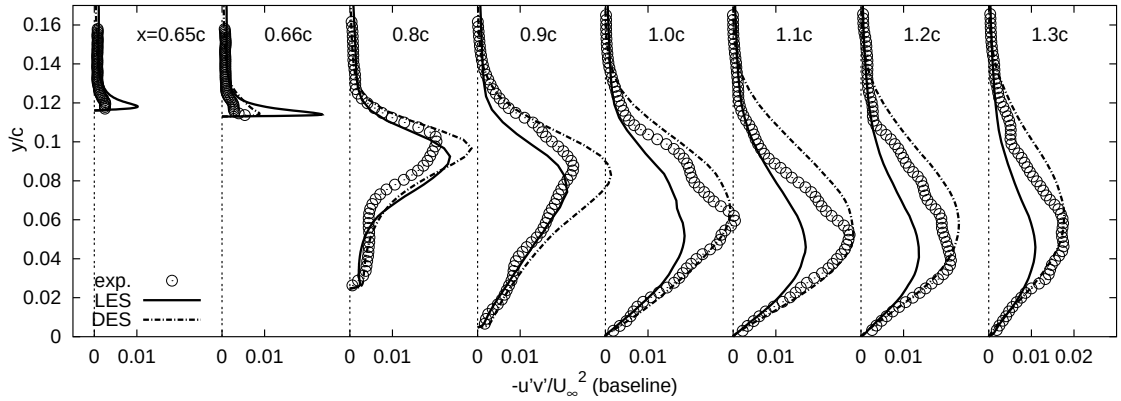

Figure 5.13: Shear stress profiles

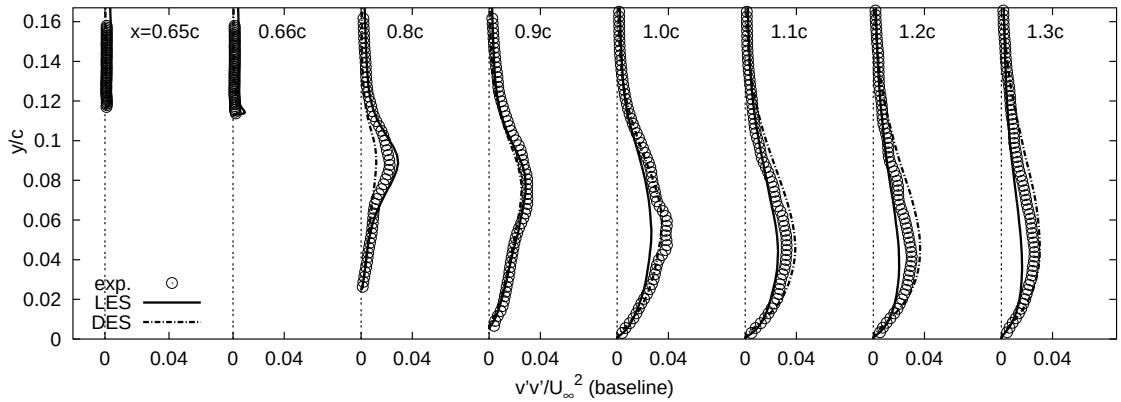

Figure 5.14: Reynolds normal stresses

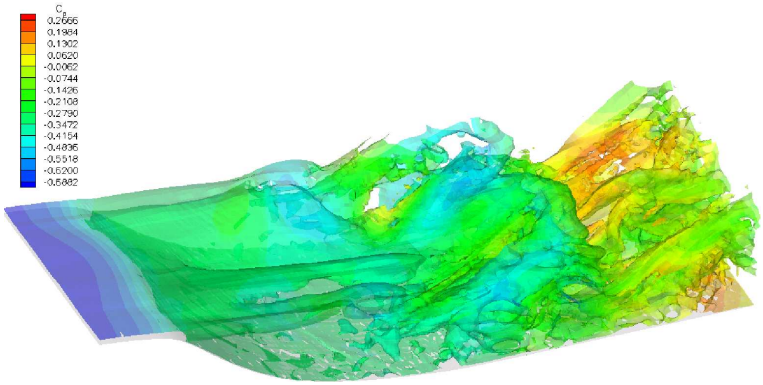

Figure 5.15: Iso-surfaces of vorticity colored by pressure obtained by DES of the flow over a wall-mounted hump (baseline case)

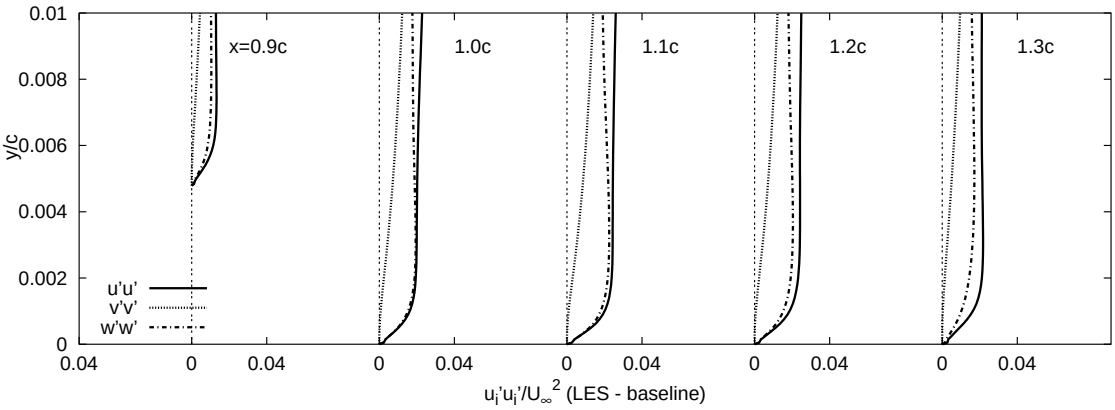

Figure 5.16: Reynolds stress components in the near-wall region

Despite the fact that the hump geometry still has a significant influence on the flow separation, which is proven by broadly correct separation obtained by RANS models, the only way to predict the flow characteristics downstream is to resolve large-scale structures which are dominant in this region of the flow. The three-dimensional instantaneous flow structures are elucidated in Fig 5.15 showing iso-surface of vorticity colored by pressure obtained by DES of the baseline hump flow. The DES treatment of the separated region results in clearly visible resolved vortical structures. Strong interaction between the separated shear layer and the wall around reattachment and further downstream can be observed. Impingement of the separated flow onto the wall gives rise to a highly anisotropic turbulence as presented by Reynolds stress components in Fig 5.16. At the same time, the spanwise stress level is comparable to the streamwise one, especially in the region of flow reattachment at x/c=1-1.1. This is an indication of flow 'splatting', which can hardly be accounted for by existing statistical models. The investigated baseline flow configuration is characterized by unsteady separation governed by large-scale unsteadiness (highly intermittent separation and reattachment regions, highly unsteady separated shear layer), all the features being beyond the reach of the inherently steady RANS ap-

proach. Hence, one can expect that the same flow subjected to flow control will be more complex and challenging for CFD validation.

5.3 Separated Flow over a Periodic Arrangement of Smoothly Contoured Hills

The last test case to be considered is even more complex, massively separated flow in a channel with streamwise periodic constrictions. Compared to the previous two cases, the influence of the geometry on separation process from a curved surface is minor. Consequently, the flow is very complex with the sensitive dependence of the mean reattachment position on that of separation, posing a great challenge for simulation strategies. An important aspect of the work on this particular case is the fact that it is undertaken in a collaborative effort involving five different flow solvers used by five different groups to cover a broad range of numerical methods and implementations. The flow over a periodic arrangement of smoothly contoured hills [44] has been extensively studied over the past few years [19, 8, 30, 41, 6, 28, 7]. Recently, this flow configuration at $Re_b = 10,595$ was selected as a common test case within the French-German research group on 'Large-Eddy Simulation of Complex Flows'. Originally based on the experiments of Almeida et al. [3], the numerical benchmark case had been modified to be more suitable for numerical simulations [44]. An experiment corresponding to this new setup is presently designed at the University of Technology Munich in order to provide future experimental reference data. New computational reference solutions have been already obtained by the French-German research group [8, 7]. These include highly resolved LES at $Re_b = 10,595$ using 13×10^6 grid cells and DNS at $Re_b = 2,800$ and $5,600$.

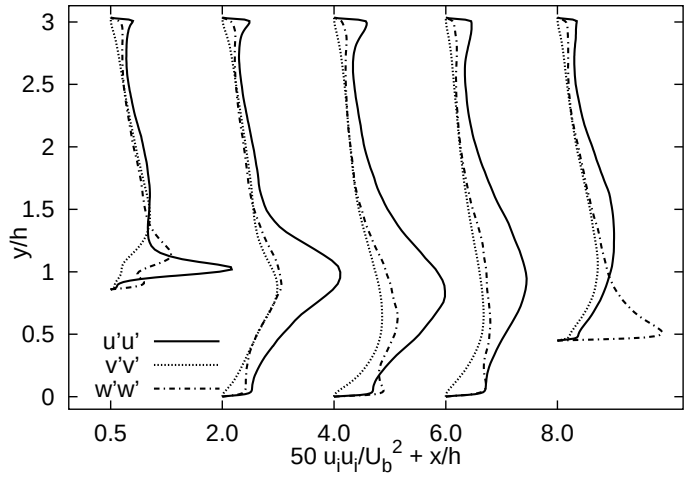

Figure 5.17: Distribution of the Reynolds stress components obtained by DES of the flow over periodic hills

The type of flow under consideration is a challenging test case for statistical turbulence models. A distinct 'splatting' of eddies on the windward side of the

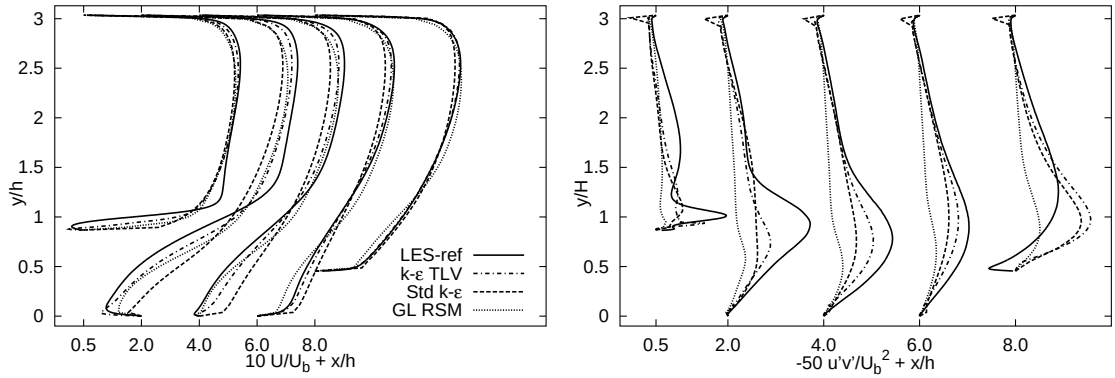

Figure 5.18: Comparison of the RANS results obtained by various turbulence models (the standard $k-\varepsilon$ model, the two-layer $k-\varepsilon$ model due to Rodi at al. ($k-\varepsilon$ TLV [56]) and Gibson and Launder Reynolds stress model (GL RSM [21]): a) mean streamvise velocity, b) Reynolds shear stress u'v'.

hill, which was recently identified by Fröhlich et al. [19], represents a structural feature reflected by generation of strong spanwise fluctuations, which is unlikely to be accounted for by any RANS model. Fig. 5.17 shows DES capturing the strong spanwise fluctuations in the regions of flow reattachment and strong acceleration along the windward slope of the hill. Poor predictions of mean flow and turbulence are obtained by RANS as illustrated in Fig. 5.18. In various workshops [30, 41], RANS methods failed to predict the reattachment accurately and exhibited a great sensitivity to the individual turbulence closure model. This failure is commonly attributed to the inability of RANS to capture the large-scale dynamics in the separated shear layer. This large-scale motion dominates the momentum exchange and thus determines how quickly the separated flow reattaches. On the other hand, LES is designed to capture these flow structures, but predictions of wall-bounded flows (without wall functions) are limited to moderate Reynolds numbers due to extremely high resolution requirements in the near-wall region. Various hybrid LES–RANS strategies were proposed to alleviate this dilemma, DES being the most popular one. If performed on a suitable grid, DES is typically expected to yield results superior to those obtained with RANS computations (for the flow investigated here cf. Fig. 5.19). However, due to its complex grid sensitivity, serious deterioration of the predictions occur if the LES–RANS interface resides either too far from or too close to the wall. Noting that the S-A model has been tuned for external aerodynamic flows at high Reynolds number, it is interesting to examine DES performance in a complex wall-bounded flow such as the periodic hill configuration. DES has been designed relying on the capability of a RANS model to predict boundary layer flows, and on the superiority of LES in separated flow regions. The hill flow poses yet another challenge for DES: strong spatial and temporal fluctuations of the separation line.

This section investigates the performance of DES for the hill flow at $Re_b = 10,595$ using computational meshes limited to one million cells – a number feasible

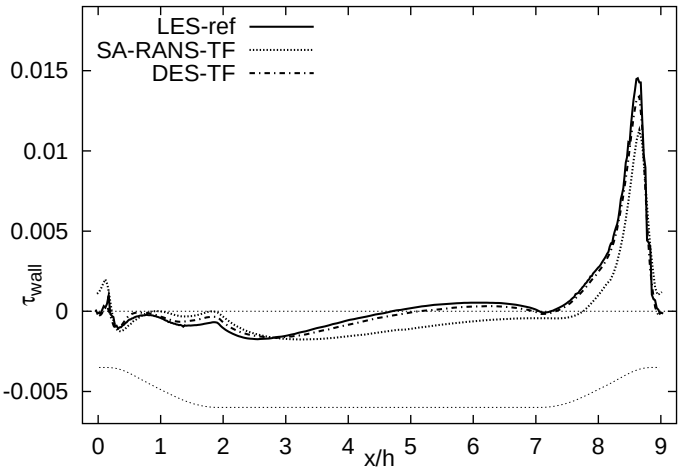

Figure 5.19: LES, DES and 2D SA-RANS predictions of the time-averaged wall shear stress; the hill contour is included for reference.

for computations on present day personal computers. In order to ensure independence of the findings from numerical methods and particular implementations, several independent research groups computed the same flow by DES using different flow solvers, but employing the same standard grid ($N_x \times N_y \times N_z = 160 \times 100 \times 60$) depicted in Fig. 5.20. As reference data serve results from a highly resolved LES obtained with roughly 13 million cells [7]. The performance of the DES is further evaluated by comparison of its results to those computed on the same grid using LES with the standard and the dynamic Smagorinsky models and an alternative hybrid LES–RANS proposed by Breuer and Jaffrézic [6] and Jaffrézic et al. [28]. In addition, LES data employing an immersed boundary technique on Cartesian meshes are included. Finally, the impact of resolution and, therefore, the location of the LES–RANS interface is studied.

A concise description of the flow configuration studied and various flow solvers employed in the present work are outlined first. Afterwards, the main features of the performed simulations will be introduced in order to facilitate the proper analysis and comparison of the results. The Reynolds number, based on the hill height (h) and the bulk velocity above the crest (U_b) is 10,595. The dimensions

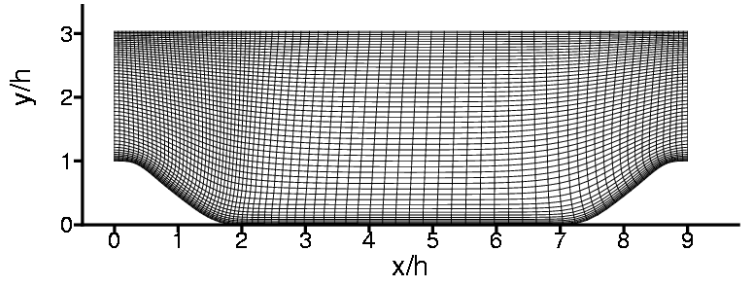

Figure 5.20: A slice of the standard grid ($x - y$ plane, every second grid line shown).

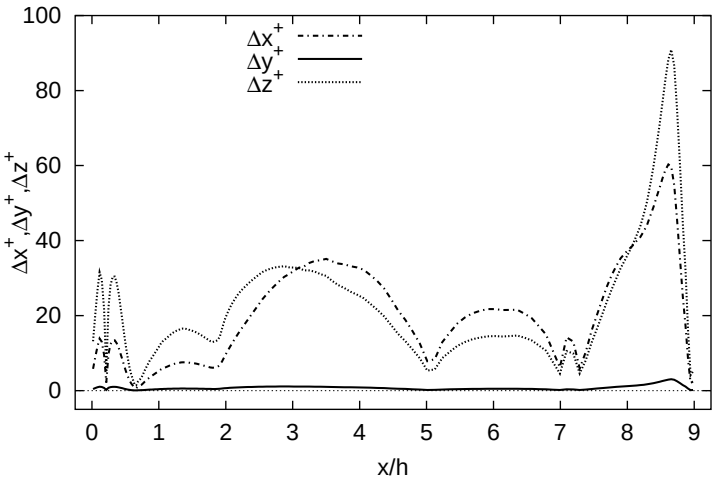

Figure 5.21: Wall-adjacent cell size in wall units along the lower wall boundary for the standard grid.

of the computational domain are $L_x = 9.0h$, $L_y = 3.035h$ and $L_z = 4.5h$. The choice of the spanwise extent is based on the investigations by Mellen et al. [44]. The flow is assumed to be periodic in the streamwise and spanwise directions, with a no-slip boundary condition applied at both walls. The flow rate is imposed by a spatially constant pressure-forcing term which is adjusted in time to yield the target mass flow rate. The standard grid used in most of the simulations consists of $160 \times 100 \times 60$ cells providing a near-wall resolution in wall units of $\Delta x^+, \Delta z^+ < 35$ in the streamwise and spanwise directions, respectively (see Fig. 5.21). The values of $\Delta {y_1}^+$ in the near-wall cells do not exceed 1 for most of the computational domain, i.e. for $x/h = 0-8$. The exception is the windward side of the hill, where the resolution decreases. Nevertheless, compared to the values of $\Delta {y_1}^+ = O(1)$, $\Delta x^+ = O(50)$ and $\Delta z^+ = O(20)$, typically recommended for wall-resolved LES, the grid is still deemed to be adequate, although significantly coarser than the grid used in the reference LES (1 vs. 13 million grid cells). This is mainly due to a larger cell size in the spanwise direction that is intentionally chosen such that the RANS region in the framework of DES covers the first 7-9 cells and 4-5 cells in the wall-normal direction at the lower and upper walls, respectively. In some computations even coarser grids are used, being obtained simply by decreasing either spanwise or streamwise resolution, while maintaining the original wall-normal cell distribution and uniformity of the cell size in the spanwise direction. These additional simulations with coarser resolutions in the wall-parallel directions are conducted in order to assess the influence of the LES–RANS interface position on the DES performance. Five computer codes, namely LESOCC [9, 10], LESOCC2 [26], ISIS [16], FASTEST [17] and MGLET [42] are used to predict the periodic hill flow. The first four codes solve the incompressible Navier-Stokes equations on body-fitted, non-orthogonal grids by finite-volume methods with collocated arrangement of the Cartesian velocity components. MGLET employs an immersed boundary method on a Cartesian grid. For this grid, $221 \times 173 \times 106$ (4.1 million) cells are used. With this number, the high wall-normal resolution achieved

Table 5.3: Summary of the computations (SJ: Šarić & Jakirlić, code FASTEST; BJ: Breuer & Jaffrézic, code LESOCC, OE-One-Equation model for the turbulent kinetic energy k; DC: Deng & Chikhaoui, code ISIS; TF: von Terzi & Fröhlich, code LESOCC2; PM: Peller & Manhart, code MGLET); t_a: averaging time, t_x: flow-through time, $(\cdot)_s$: separation point, $(\cdot)_r$: reattachment point.

Case	*Grid*	*Model*	$\Delta t U_b/h$	t_a/t_x	$(x/h)_s$	$(x/h)_r$
LES-ref	$281 \times 222 \times 200$	*DSM*	0.0018	141	0.190	4.694
DES-SJ	$160 \times 100 \times 60$	*SA*	0.0105	31	0.214	5.123
DES1-SJ	$160 \times 100 \times 45$	*SA*	0.0105	30	0.214	5.012
DES2-SJ	$160 \times 100 \times 30$	*SA*	0.0105	28	0.214	4.792
LES-SJ	$160 \times 100 \times 30$	*SM*	0.0105	28	0.182	4.902
LES1-BJ	$160 \times 100 \times 60$	*SM*	0.004	69	0.214	4.576
LES2-BJ	$160 \times 100 \times 60$	*DSM*	0.004	71	0.247	4.262
DES-BJ	$160 \times 100 \times 60$	*SA*	0.004	67	0.182	5.235
HYB-BJ	$160 \times 100 \times 60$	*OE*	0.004	65	0.279	4.792
DES-DC	$160 \times 100 \times 60$	*SA*	0.007	200	0.187	5.013
DES1-DC	$80 \times 100 \times 60$	*SA*	0.007	90	0.214	4.957
DES-TF	$160 \times 100 \times 60$	*SA*	0.008	93	0.182	5.123
LES-IB-PM	$221 \times 173 \times 106$	*DSM*	0.004	80	0.270	4.270

by the curvilinear grid for the other codes could not be reached. At the point of maximum wall shear stress, the wall-adjacent cell size is $\Delta x^+ \approx 11$, $\Delta y^+ \approx 8$ and $\Delta z^+ \approx 56$ leading to a maximum wall-normal distance of about 10 wall units. In all codes, second-order central differences are used to discretize convective and diffusive terms. An exception concerns the simulations performed with the ISIS code for which the Gamma Differencing Scheme (GDS) is applied for the transport equation for $\tilde{\nu}$, giving a behavior similar to the first-order upwind scheme [31]. With LESOCC2, the HLPA scheme [80] is used for the $\tilde{\nu}-$equation. Different second-order accurate time integrations are employed.

The main objective here is a comparative study of the periodic hill flow, focused on DES as the arguably most popular and widely used hybrid LES–RANS method. Another hybrid LES–RANS technique proposed by Breuer et al. [6] is tested for comparison. This method employs a one-equation (OE) model based on the transport equation for the turbulent kinetic energy which governs the modeled turbulent kinetic energy k_{mod} in RANS mode and the subgrid scale turbulent kinetic energy k_{sgs} in LES mode. More details about the method and switching criteria defining the LES–RANS interface can be found in [6, 28]. A summary of the simulations performed is given in Table 5.3 displaying the notation used henceforth, the main parameters and information pertinent to the computations, and the location of separation and reattachment points. At this point, one should note that the LES-ref, LES2-BJ and LES-IB-PM computations use the dynamic SM, whereas LES1-BJ and LES-SJ employ the standard Smagorinsky model with the constant $C_s = 0.1$

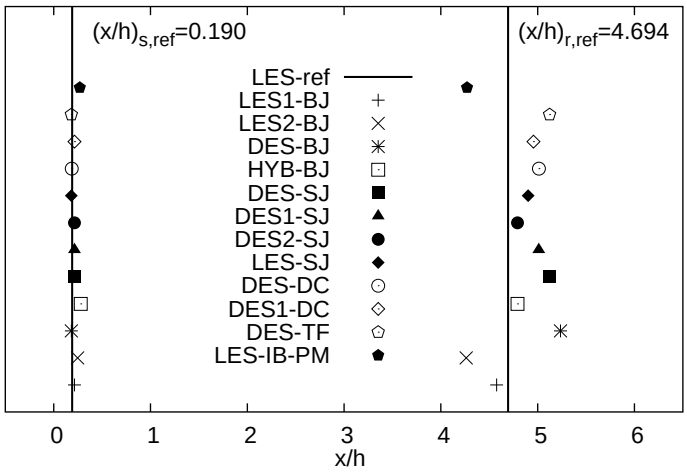

Figure 5.22: Comparison of predicted separation and reattachment locations.

damped by means of the standard van-Driest damping function. It should also be noted that LES-IB-PM uses no wall model although the wall-normal resolution goes up to 10 wall units.

In the following subsections, the performance of DES will be assessed. The Reynolds number of 10,595 is not as high as desirable for testing an hybrid LES–RANS method, but an analysis can only be undertaken relying on highly resolved LES reference data [8, 7] which are not available at higher Reynolds numbers. An important issue for the successful computation of this flow is to accurately capture the separation point [19]. This is achieved by all applied methods as illustrated in Fig. 5.22 and Table 5.3 indicating that the grid resolutions are sufficiently fine for capturing this flow phenomenon. Deviations in predicted reattachment locations are observed; the majority of the computations predict a delayed reattachment.

Henceforth, profiles of velocities, Reynolds stresses and turbulent kinetic energy are compared to those of the reference LES at the following stations: $x/h = 0.5$, 2, 4, 6 and 8. The selected positions include the regions just upon separation ($x/h = 0.5$), in the middle of the recirculating zone ($x/h = 2$), prior to the reattachment ($x/h = 4$), the post-reattachment and flow recovery ($x/h = 6$), and the region of accelerating flow on the windward slope of the hill ($x/h = 8$).

5.3.1 DES on the Standard Grid using Different Flow Solvers

First, DES results generated using different flow solvers on the same standard grid are presented. Figs. 5.23 and 5.24 show the mean velocity and turbulence statistics. The mean streamwise velocity profiles exhibit good agreement with the reference data at positions $x/h = 0.5$, 2 and 8, whereas discrepancies are observed in the regions prior and after flow reattachment (at locations $x/h = 4$ and 6). Here, the backflow velocity ($x/h = 4$) is overpredicted corresponding to longer reattachment and slower recovery farther downstream (Fig. 5.23a). Despite the good agreement of the Reynolds shear stresses (Fig. 5.23b), DES results yield insufficient turbulent

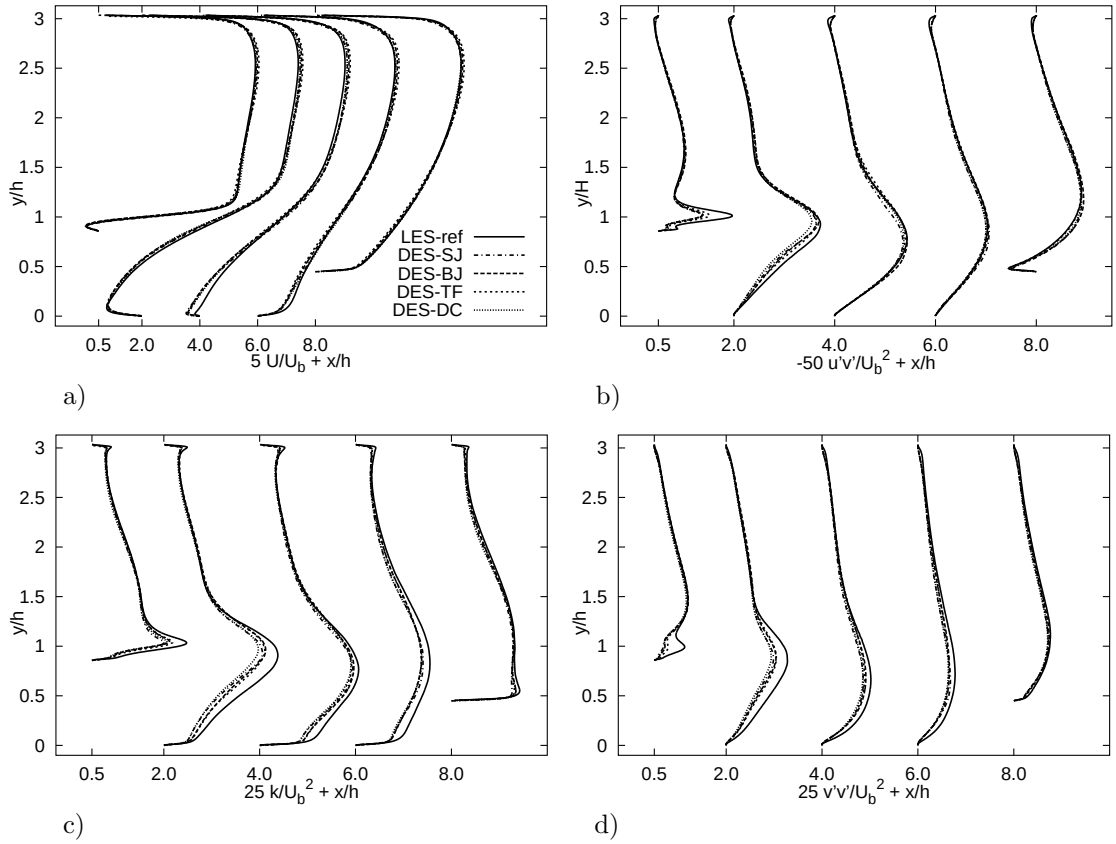

Figure 5.23: Comparison of DES predictions obtained by different codes on the standard grid: a) mean streamvise velocity, b) Reynolds shear stress u'v', c) turbulent kinetic energy k, d) normal Reynolds stress v'v'.

kinetic energy within the reattachment region (Fig. 5.23c). Furthermore, the near-wall peak of the wall-normal Reynolds stress v'v' at $x/h = 0.5$ cannot be captured accurately by DES, which has an impact on the results farther downstream (see Fig. 5.23d). One possible reason for this behavior could be that the 'DES filter' $\Delta = \max(\Delta x, \Delta y, \Delta z)$ in this region is 40% larger than the one employed by LES $\Delta = (\Delta x \Delta y \Delta z)^{1/3}$ on the same grid. Hence, the SGS-viscosity of DES is larger in this flow region. Code dependency, on the other hand, can be ruled out, since different flow solvers with distinct implementations and various numerical methods predict the same flow behavior on the same grid. However, minor discrepancies in the results remain owing to differences in numerical methods and chosen time steps. Slight deviations in the mean flow and predictions of turbulence statistics originate from differences in the computed turbulent viscosity as shown in Fig. 5.24a. The profiles of the wall shear stress on the lower wall agree reasonably well with the reference data (Fig. 5.24b), but they reveal that the DES consistently underpredict the wall shear stress in the reattachment region and consequently yield a delayed reattachment. Overall, the mutual agreement of the independently performed DES is very good, thus demonstrating a high level of fidelity of the results.

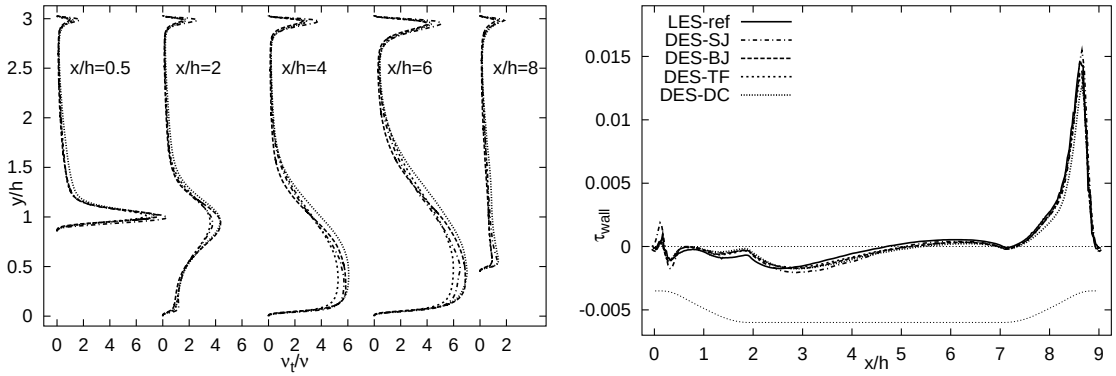

a) b)

Figure 5.24: Comparison of DES predictions obtained by different codes on the standard grid: a) time-averaged turbulent viscosity and b) time-averaged wall shear stress distribution on the lower wall.

5.3.2 Influence of the Turbulence Modeling Strategy

In order to investigate the influence of the turbulence modeling, i.e. applied simulation strategies, profiles of the mean streamwise velocity along with the (resolved) Reynolds shear stresses obtained with different approaches are compared in Fig. 5.25. All results in this figure are obtained with the same code (LESOCC) on the standard grid. The mean velocity profiles displayed in Fig. 5.25a exhibit a similar good behavior of both hybrid LES–RANS computations DES-BJ and HYB-BJ, but also a surprising deficiency of the dynamic LES (LES2-BJ) in this simulation, which will be discussed below. Concerning HYB-BJ and DES-BJ, despite the discrepancy at the location $x/h = 4$ already mentioned for all the previously commented DES, the mean streamwise velocity is in good agreement with the reference LES. It is noticeable that HYB-BJ captures the reattachment point accurately and better than DES-BJ (see Fig. 5.22). One can see that the hybrid simulation HYB-BJ fails to capture the tiny separation at the hill crest (see Fig. 5.26). This kind of behavior of the wall shear stress has already been observed in RANS simulations as illustrated in Fig. 5.19. A detailed evaluation of this hybrid approach can be found in [28].

Excellent predictions of the mean streamwise velocity profiles obtained by LES employing the standard SM are evident. This supports the previous assertion that the grid resolution is deemed to be adequate, with the exception of the region of separated shear layer (see Fig. 5.25b at $x/h = 0.5$) where shear stress overpredictions associated with a locally coarser grid are visible. At the same time, the results reveal surprisingly poor performance of the dynamic SM. This is demonstrated by the wall shear stress distribution plotted in Fig. 5.26 which shows the dynamic SM predicting too a short recirculation zone. This unexpected behavior is an indication of high grid sensitivity of the dynamic SM, which is confirmed by direct comparison of various LES computations presented in Figs. 5.27 and 5.28 all applying DSM. The simulation LES-IB-PM using the immersed boundary method was performed with 4.1 million grid cells. The computational effort of the additional cells is more than compensated by a substantially lower cost per grid point. Therefore, the increase in number of

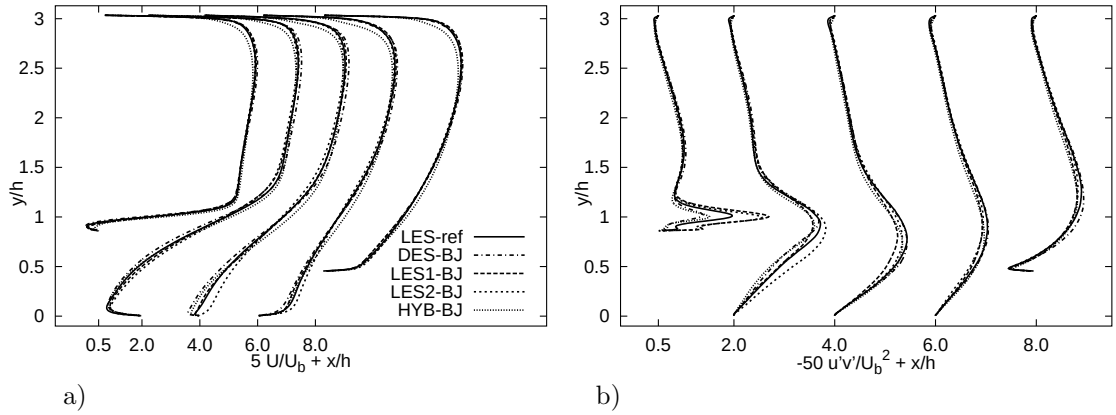

Figure 5.25: Influence of turbulence modeling/simulation strategies on the hill flow predictions on the same grid: a) mean streamvise velocity, b) Reynolds shear stress u'v'.

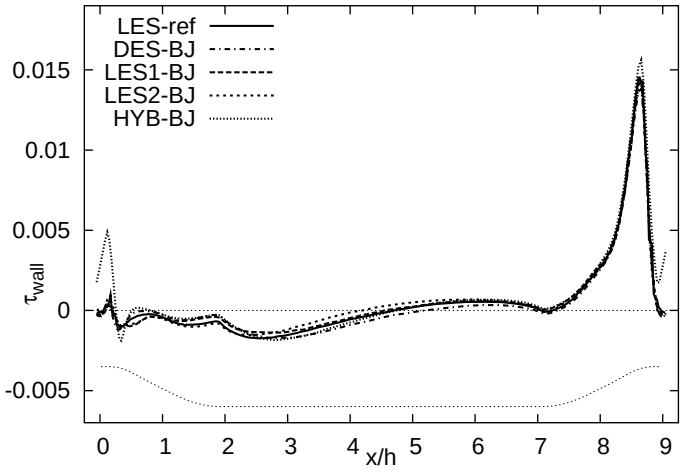

Figure 5.26: Time-averaged wall shear stress distributions on the lower wall predicted by different models.

grid points with this method is justified for a fair comparison. However, due to the use of a Cartesian grid, the wall-normal resolution was substantially coarser than in the curvilinear grid used for the other simulations. Differences with respect to LES2-BJ are clearly noticeable in the profiles of the mean streamwise velocity and shear stress. In particular, LES-IB-PM yields better velocity predictions (Fig. 5.27a). The wall shear stress distribution shown in Fig. 5.28 reveals that despite close agreement within the recirculation zone, these two simulations generate different wall shear stresses elsewhere. LES-IB-PM fails to capture both the tiny separation at the hill crest and the small recirculation region just before the windward side of the hill. These deviations between the two LES predictions using the dynamic SM can be attributed to the different grids and boundary treatments employed, whereas the variations between the standard (LES1-BJ) and dynamic SM (LES2-BJ) using the same code and grid can be imputed to a higher SGS eddy-viscosity prediction of LES2-BJ in comparison to LES1-BJ.

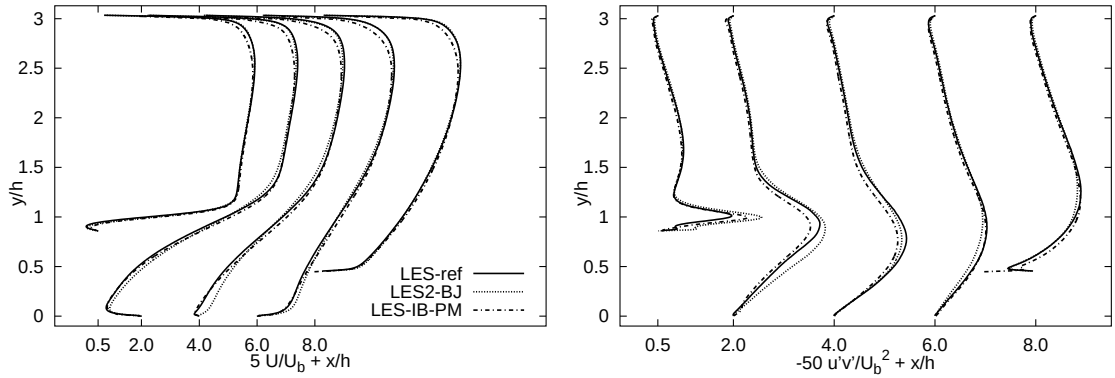

Figure 5.27: Comparison of LES results obtained by different codes: a) mean streamwise velocity, b) Reynolds shear stress u'v'.

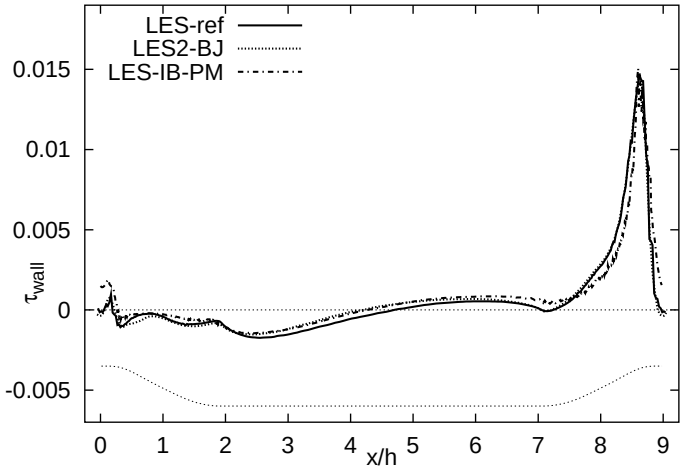

Figure 5.28: Time-averaged wall shear stress distributions on the lower wall for LES obtained by different codes.

5.3.3 DES vs. LES on a Coarser Grid

Comparable deviations from the reference solution for LES and DES on the standard grid have been demonstrated in the previous section. The two methods are further compared directly by additional simulations conducted on the same, but two times coarser grid in the spanwise direction (DES2-SJ, LES-SJ). Indeed the purpose of the hybrid LES–RANS strategies is to decrease the near-wall resolution in the streamwise and spanwise directions, for which LES is assumed to fail. Profiles of the mean streamwise velocity, Reynolds shear stress and wall shear stress are compared in Figs. 5.29 and 5.30. Still, the results of DES are comparable to LES and no evident superiority of DES is observed. This tends to prove that the grid resolution is still sufficient for LES to predict reasonably well separation and reattachment. Temmerman et al. [71] have also obtained separation and reattachment points at x/h =0.23 and 4.64, respectively, by LES using $N_x \times N_y \times N_z = 112 \times 64 \times 56$

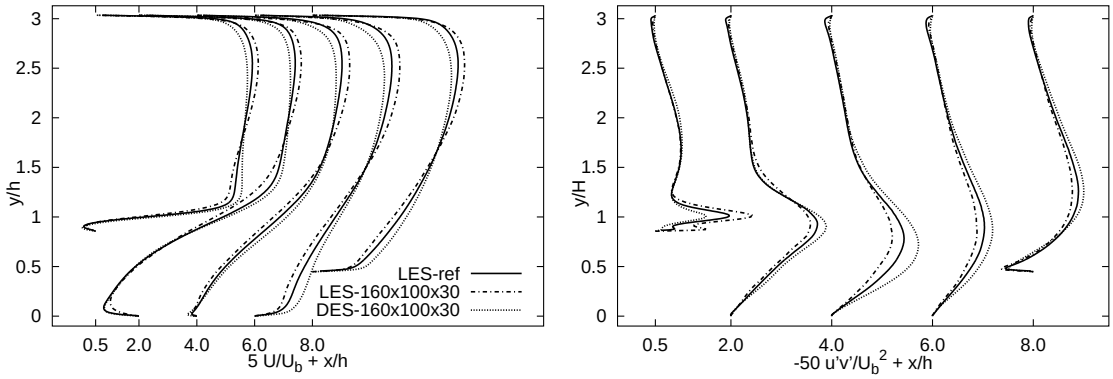

Figure 5.29: DES vs. LES on the same coarse grid: LES-SJ and DES-SJ. a) mean streamvise velocity, b) Reynolds shear stress u'v'.

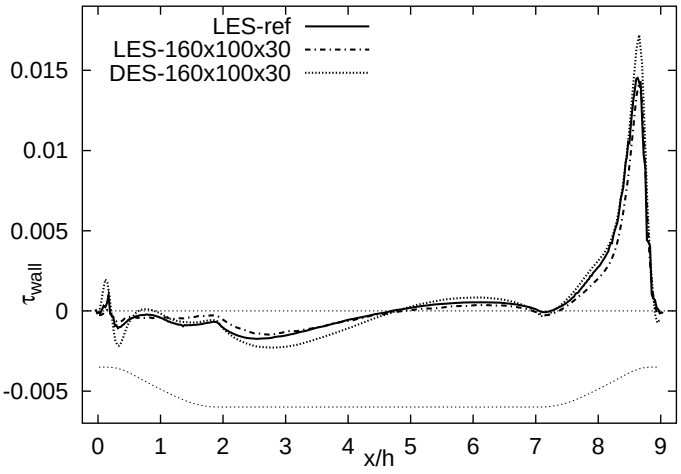

Figure 5.30: Time-averaged wall shear stress distributions on the lower wall: DES vs. LES on the same grid.

cells. Hence, the considered grids are 'not coarse enough'. One could assume that for higher Reynolds numbers this might not be the case any more and DES might finally achieve significant advantages over LES on the same grid.

5.3.4 Influence of the LES–RANS Interface Location

Finally, the influence of the position of the LES–RANS interface on the performance of DES is investigated. For this purpose, coarser grids are generated simply by decreasing the spanwise resolution of the standard grid. An additional configuration is created by removing every second grid point in the streamwise direction (grid: $80 \times 100 \times 60$). In both cases the original wall-normal cell distribution is intentionally maintained to provide different positions of the LES–RANS interface which is dictated by grid design. Fig. 5.31 displays profiles of the mean streamwise velocity and Reynolds shear stress obtained for different DES. No significant differ-

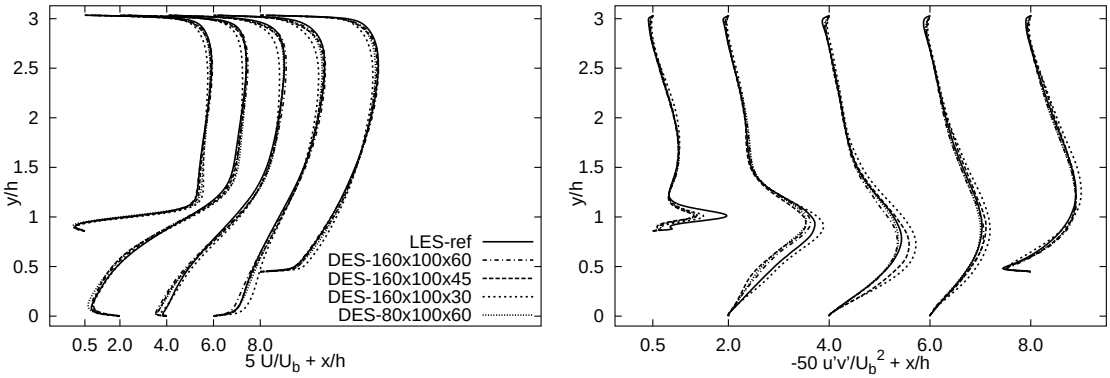

a) b)

Figure 5.31: Influence of grid resolution on DES: a) mean streamwise velocity, b) Reynolds shear stress u'v'.

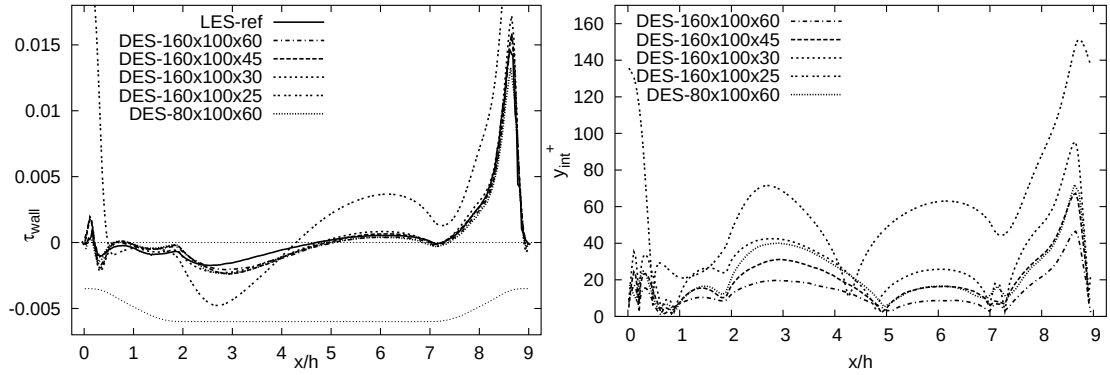

a) b)

Figure 5.32: DES with different grids and locations of the interface. a) time-averaged wall shear stress distributions on the lower wall, b) position of the LES–RANS interface.

ences between the results are observed except for the computation DES2-SJ which predicts an earlier reattachment. However, overpredictions of the shear stresses and a too fast recovery of the boundary layer are observed downstream of reattachment. Results of DES on an even coarser mesh containing only 25 spanwise cells are included in Fig. 5.32 showing the wall shear stress distribution and the positions of the LES–RANS interface for the corresponding computations. As the number of spanwise cells is decreased from 60 down to 45 and 30, the position of the LES–RANS interface shifts away from the wall as depicted in Fig. 5.32b. Predictions of the wall shear stress are consistently deteriorating, but only within the range of $x/h = 0 - 0.5$, whereas the separation point is still captured reasonably well. As the number of spanwise cells is ultimately decreased from 30 to 25, the profile changes dramatically, resulting in extremely poor predictions. This is explained by the LES–RANS interface position which is now beyond the (time-averaged) boundary layer thickness of $\delta \approx 0.1h$ at this location. Hence, for 25 grid cells in the spanwise direction, i.e., an LES–RANS interface at 0.117 h, DES is clearly used outside its intended framework.

Detached-eddy Simulations were scrutinized for predicting turbulent channel flow with periodic hill constrictions at a Reynolds number of 10,595 based on bulk velocity and height of the hills. Different flow solvers were used by independent research groups to establish independence of the results from numerical methods and particular implementations. The DES data was compared to results obtained using a highly resolved LES. While discrepancies to the reference data were observed, the DES performed overall well considering the coarse grid. However, for the flow configuration chosen for the present investigation, LES or an alternative hybrid LES–RANS method yielded results of similar quality. Further coarsening of the grid did not alter the performance of DES substantially unless the interface between LES and RANS mode moves outside the boundary layer on the crest of the hill, deteriorating the results substantially.

The predictive capabilities of various CFD methods were evaluated for the three representative complex separated flow configurations. It seems to be unlikely that any existing RANS model, regardless of its complexity, can provide the accurate predictions needed in a number of complex separated and vortical flows. Despite numerous experimental studies conducted on separated flows, their contribution to the understanding of the flow physics and fundamental mechanisms of separation and reattachment is very limited. Computational strategies like LES and DES are expected to provide information on turbulence structure and separation process of the flow. Of particular interest is understanding of many complex flow interactions and modifications of turbulence structures occurring in separated flows subjected to active flow control. Capability of simulation strategies to predict the mean flow and turbulence in separated flows relevant to AFC will be studied in the next chapters.

6 Periodically Perturbed Separated Flow over a Backward-facing Step

The main results of the performed numerical simulations are presented next. The two selected test cases relevant to AFC applications, including the baseline configurations (without flow control) as well, will be considered. A periodically-perturbed backward-facing step flow at low Reynolds number is investigated in this chapter, followed by the next one dealing with the computational study of locally forced separated flow over a wall-mounted hump at high Reynolds number. Prior to discussion of the results, the reference experiments and their important outcomes are described. The main features of the numerical simulations and case specific details will be introduced in order to facilitate proper analysis and comparison of the results.

6.1 Separated Flow over a Backward-facing Step

The backward-facing step flow is a well-known test case for studying the influence of local streamline curvature. The flow separates at the step edge, forming a curved shear layer which bifurcates at the reattachment region; one branch flowing back creates a separation bubble behind the step, another branch creates a new boundary layer downstream. The level of turbulence in the separated shear layer aligned with the mean dividing streamline bordering the separation bubble is of decisive importance when controlling reattachment length. A higher level of shear stress implies an enhancement of the fluid entrainment into the shear layer - higher momentum transport - and consequently shortening of the recirculation bubble. In addition to the strong mean flow gradient in the vertical direction, representing the main source of turbulence production, and a curvature-generated turbulence production, turbulence can be further generated by introducing a high-velocity jet into the shear layer. The flow perturbation created in such a way causes an intensive flow stretching (mean flow deformation enhancement, especially with respect to the axial velocity component) leading consequently to an enhanced turbulence level.

6.2 Experiments

The backward-facing step flow configuration considered here (Fig. 6.1; $Re_H = U_c H/\nu = 3700$) has been investigated experimentally by Yoshioka et al. [76, 77, 78]. The experiments were performed in the test section consisting of the backward-facing step mounted in the closed-loop water channel as described in Yoshioka et al. [76]. The step height H was 20 mm, resulting in the expansion ratio of 2:3

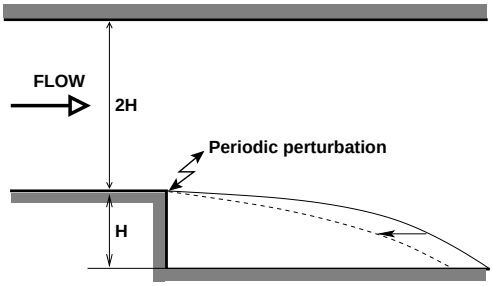

Figure 6.1: Schematics of the periodically perturbed backward-facing step flow.

whereas the aspect ratio based on H and the channel span was 1:12. A slit of 1 mm width was opened at the step edge along the span. The periodic perturbation was introduced through this slit as a direct, alternating suction/injection in the direction inclined 45° relative to the horizontal axis of the channel. The injection velocity was designed to follow a sinusoidal law: $v_e = V_e \sin\phi$, V_e being the velocity amplitude ($V_e = 0.3U_c$) and ϕ the phase angle. Perturbation frequencies, f_e ($\phi = 2\pi f_e t$), corresponding to the Strouhal numbers $St = 0.08, 0.19$ and 0.30 were investigated ($St = f_e H/U_c$, U_c being the centerline velocity in the inlet channel). The flow at the inlet of the test section was a fully developed turbulent channel flow with the estimated friction velocity corresponding to $Re_\tau = 199$.

The turbulence statistics of the flow was obtained employing a two-dimensional particle imaging velocimeter (PIV). The reattachment length varied with the applied perturbation frequency, being reduced by 30% at the optimum frequency, $St = 0.19$. The promotion of the flow reattachment in time-averaged flow was well correlated with the increase in the production of the Reynolds shear stress. The phase-averaged flow field revealed existence of the organized fluid motion in the separated shear layer. The region with strong deformation appeared between the vortex structures, which promoted the production of the Reynolds stress.

6.3 Numerical Simulations

The results obtained by various statistical models are available from the 9^{th} ERCOFTAC workshop on refined turbulence modeling (Jakirlić et al., [30]). One can recall that the workshop results exhibited a certain scatter and are probably not suitable for a very detailed comparison. Generally speaking, independent of the modeling level, all turbulence models have exhibited a weaker sensitivity to the perturbation compared to the experimental results. The reduction of the reattachment length was predicted in all unsteady RANS computations (URANS); however, compared to the reference case without perturbation, the magnitude of the reduction was far below that observed in the experiment. Hence, it is challenging to compute the flow considered by LES and DES, the CFD techniques which are expected to reproduce unsteady flows better than statistical turbulence models. In particular, it is interesting to see how the same model (S-A) performs in two different computational frameworks: RANS and DES.

6.3.1 Computational Details

The size of solution domain adopted behind the step is $L_x \times L_y \times L_z = 30H \times 3H \times \pi H$. Different grid configurations were employed comprising between 190.000 (142×82×16) and 590.000 (220×82×32) grid cells, but preserving the number ($N_y = 82$) and distribution of the cells in the wall-normal direction. The two grids specified were finally adopted for the reference DES and LES computations respectively. In the course of grid sensitivity study different grid resolutions and spanwise dimensions were also tested (see Table 6.2 for more details). The grid resolution in the near-wall region was chosen to ensure between 6-8 grid cells within the viscous sub-layer for all the cases computed. One of the main difficulties in tackling this flow with LES or DES is to impose the proper inflow boundary conditions. The inlet data corresponding to a fully developed channel flow are generated by separate pre-cursor simulations, using both LES and DES methods. It should be noted that the majority of LES and DES runs are performed with the LES inlet profiles, having the same wall-normal and spanwise grid spacing, as well as the time step, avoiding any interpolation at the inlet plane. However, the additional DES of the backward-facing step flow with the inlet profiles generated by DES of the channel flow (with spanwise domain size extended to $4H$ and finer grid in the wall-normal direction), indicate that the results are not expected to differ significantly, whatever inlet data is taken (LES or DES). LES computations are performed with the Smagorinsky constant C_s set to 0.065, without damping in the near-wall region. The primary reason for this selection is the fact that a plane channel flow is computed with the same C_s value. Some additional simulations of the channel flow using different settings (C_s=0.1 with and without inclusion of the standard Van Driest damping of the Smagorinsky coefficient) have shown a small influence of both the C_s value and its near-wall damping. This might be due to a very low flow Reynolds number corresponding to $Re_\tau \approx 190$.

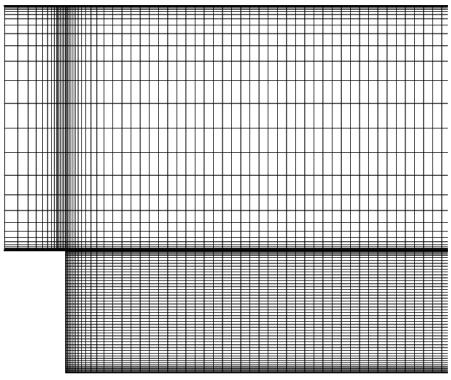

Figure 6.2: Grid detail in region around the step.

The instantaneous inlet velocities generated by the pre-cursor LES are prescribed at the inlet placed at $L_i = H/2$ upstream of the channel expansion. The periodic boundary conditions are employed in the spanwise direction, whereas the convective

Table 6.1: Plane channel flow simulations

Run	$\frac{L_x}{H}$	$\frac{L_z}{H}$	Re_τ	$\frac{\Delta t U_c}{H}$	Δx^+	Δy^+ $\frac{min}{max}$	Δz^+
$LES - 64 \times 32 \times 32$	2π	π	188	0.047	18.5	$\frac{0.14}{37.7}$	18.5
$LES - 100 \times 60 \times 32$	2π	4	188	0.019	11.8	$\frac{0.56}{14.2}$	23.5
$LES - 48 \times 96 \times 48$	2π	π	196	0.047	19.2	$\frac{0.05}{13.3}$	12.8
$DES - 100 \times 60 \times 32$	2π	4	181	0.019	11.4	$\frac{0.54}{13.6}$	22.7

boundary condition:

$$\frac{\partial \overline{U}_i}{\partial t} + U_{con} \frac{\partial \overline{U}_i}{\partial x} = 0 \tag{6.1}$$

is imposed at the outflow plane, the convective velocity being set to the mean streamwise velocity integrated across the exit plane. The computational grid typically consists of four blocks, two upstream (one comprising the region of the narrow opening and one upstream of it) and two downstream of the step edge (one situated behind the step covering one third of the corresponding channel height and one above it). The grid detail of the inlet region and the part of the domain around and just downstream of the step edge is shown in Fig. 6.2. A simple, periodically oscillating jet discharging with a uniform velocity profile ($v_e = V_e \sin(2\pi f_e t)$) is assumed at the slit ($0.05H = 1\ mm$ wide), which is covered by five grid cells.

Tables 6.1 and 6.2 summarize the basic computational details, providing also the notation used throughout when presenting the results. The dimensions of the computational boxes in both streamwise (only for channel flow) and spanwise directions, and position of the inlet plane (L_i) are in line with the conclusions drawn from the works of Moin and Kim [46] and Akselvoll and Moin [2]. The simulations are started with the flow field obtained by RANS, which is initially perturbed, or with the previous LES or DES flow field in the subsequent runs. Depending on the initial conditions, the flow is computed for a period of 2-6 flow-through times before taking the statistics. The statistics are then sampled over a period of 6-8 flow-through times. The CFL number, representing the time step chosen, is less then unity over the majority of the solution domain. The exceptions are the narrow region around

Table 6.2: Backward-facing step simulations

Run	$\frac{L_z}{H}$	St	$\frac{\Delta t U_c}{H}$	Δx^+ $\frac{min}{max}$	Δy^+ $\frac{min}{max}$	Δz^+
$LES - 220 \times 82 \times 32$	π	*all*	0.047	$\frac{14}{107}$	$\frac{0.14}{37.7}$	18.5
$DES - 220 \times 82 \times 32$	π	0.0	0.047	$\frac{14}{107}$	$\frac{0.14}{37.7}$	18.5
$DES - 142 \times 82 \times 16$	π	*all*	0.047	$\frac{25}{115}$	$\frac{0.14}{37.7}$	37
$DES - 142 \times 110 \times 32$	4	0.0	0.019	$\frac{25}{115}$	$\frac{0.54}{13.6}$	22.7

the thin slit (1 mm) at the step edge, and the long region with refined grid at $y = H$, Fig. 6.2. Here, due to the high grid resolution in the vertical direction and the large normal velocity component caused by the perturbations, the CFL number reaches its maximum value between 1.5 (fine grid-$N_y = 110$, unperturbed case), 5.3 (fine grid-$N_y = 110$, perturbed case) and 13.3 (coarse grid-$N_y = 82$, perturbed case).

6.3.2 Results and Discussion

The predictions of a plane channel flow are presented first, afterwards the backward-facing step simulations will be discussed. In both cases the time-averaged results have been extracted to provide a valuable comparison with available experimental data. The results of some supplementary LES runs will be presented as well. The main goal of these additional simulations is to assess the influence of inlet boundary conditions (unperturbed case) on the mean flow and turbulence predictions, and to extract some phase-averaged quantities (case $St = 0.19$) in order to investigate phase-average behavior of the flow.

6.3.2.1 Pre-cursor Simulations of a Plane Channel Flow

The results of the pre-cursor simulations of a plane channel flow, used to generate the inflow data, are displayed in Figs. 6.3 and 6.4. Besides the experimental data upstream of the step ($x/H = -0.6$), the direct numerical simulations of a fully developed turbulent channel flow at $Re_\tau = 180$ (Kim et al., [36]) are used for comparison. One should keep in mind that the computed Re_τ values differ slightly when compared to the DNS and experimental value (estimated as $Re_\tau = 200$), as shown in Table 6.1. The mean velocity profiles obtained from the simulations with 32 or 60 points in the wall-normal direction are overpredicted in the the log-law region when compared to the DNS and experimental data (Fig. 6.3). This is regarded as an expected outcome with respect to the relatively coarse resolution. Also, a certain underprediction of the velocity in the viscous sublayer is clearly noticeable. In general, the streamwise velocity fluctuations are overpredicted, while the wall-normal fluctuations are underpredicted (Fig. 6.4-left), which can again be attributed to the resolution issue. The Reynolds shear stress profiles, given in Fig. 6.4-right, show the same tendency. The only exception is the run $DES - 100 \times 60 \times 32$. Obviously, it is due to the fact that in this region the DES operates as a RANS. Important information here is the position of the 'interface' between the LES and RANS flow domain parts in the DES framework, which is dictated by the computational grid. They matched at $y^+ = 14.8$ ($y/H = 0.082$), which could be regarded as an upper

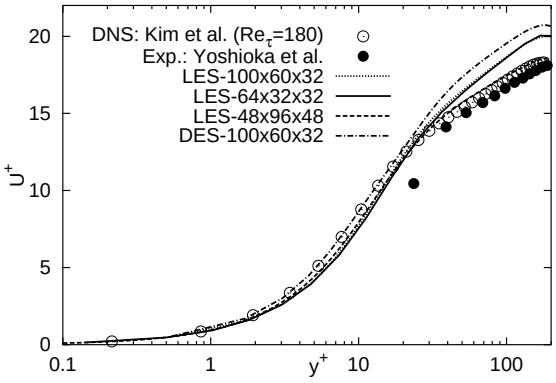

Figure 6.3: Semi-log profiles of the mean velocity.

limit. By placing the interface farther away from the wall, the results return to those obtained by using the S-A RANS model, exhibiting a severe underprediction of near-wall maximum of streamwise stress component (Leschziner, [40]), typical for all linear eddy-viscosity model schemes. On the other hand, the interface penetrating into the viscous sublayer should also be avoided. If the LES region in this hybrid approach resides too close to the wall due to insufficient resolution (one would have actually a resolution typical for RANS in the LES region), too low viscosity and turbulence levels could be obtained, possibly causing poor flow predictions. This explains the reasons for adopting somewhat larger spanwise dimensions ($4H$ instead of πH), providing the proper interface location for the given grid size (the companion run $LES - 100 \times 60 \times 32$ - is carried out just in order to validate the DES results).

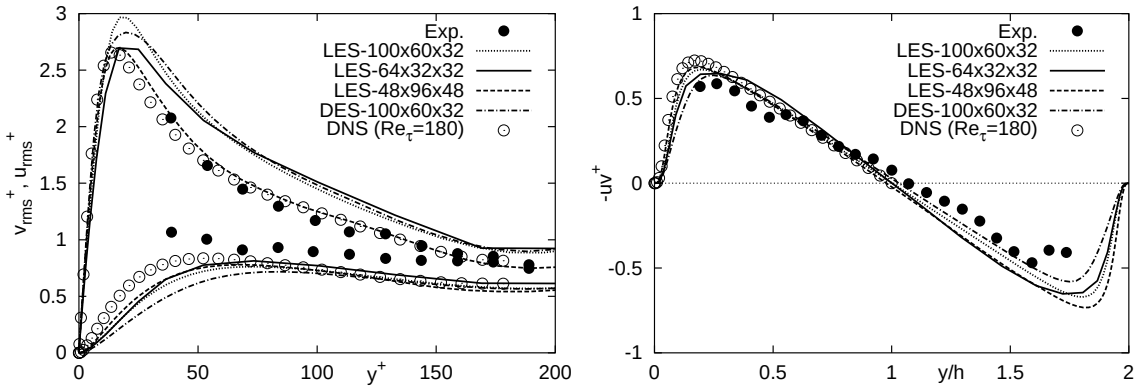

Figure 6.4: Streamwise and wall-normal Reynolds stresses; Reynolds shear stress profiles

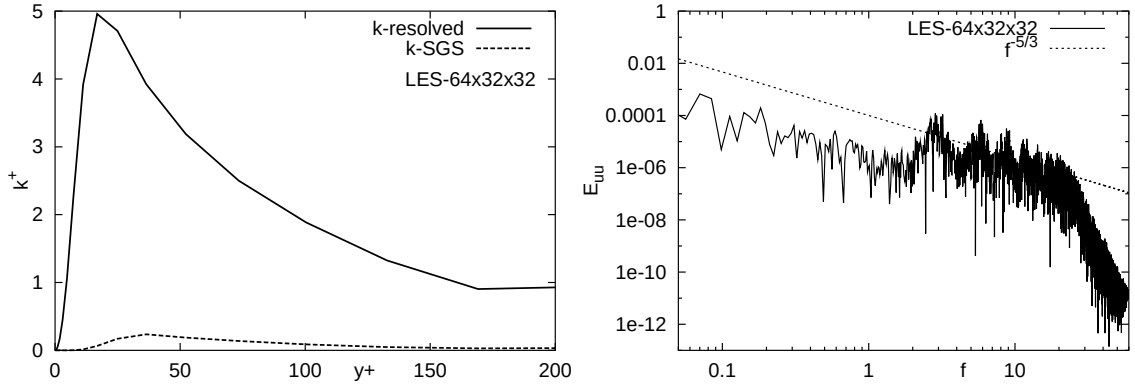

Figure 6.5: Resolved and modelled SGS kinetic energy; Frequency-spectra of the streamwise velocity fluctuations at the symmetry plane ($y^+ = 188$)

It results in a somewhat larger representative mesh size $\Delta_{DES} = max(\Delta x, \Delta y, \Delta z)$ leading consequently to a wider RANS-operating flow domain.

The SGS contribution to turbulence kinetic energy (k) is estimated from the LES using the grid $64 \times 32 \times 32$. This analysis shows a minor contribution to the total k-value. The absolute amount of the modeled SGS kinetic energy (estimated as $k_{sgs} = \Delta^2|S|^2/0.3$, according to Mason and Callen [43]) reaches its maximum in the near-wall region (Fig. 6.5-left) but it is still only about 8% of the resolved kinetic energy. Finally, frequency spectra of the streamwise velocity fluctuations, calculated in the symmetry plane of the channel at $y/H = 1$, is plotted in Fig. 6.5-right. The time scales of the fluctuations may also be interpreted as spatial scales of turbulent fluctuations (the Taylor hypothesis). Despite a relatively coarse resolution in this region of the flow ($\Delta y^+ = 37.7$), one can identify the trend towards a $f^{-5/3}$ range. A regular decay close to $-5/3$ is observed over more than one decade in f, which is indicative of an inertial subrange. It may be concluded that the results obtained in this preliminary simulations with the given grid configurations agree fairly well with the available experimental data. In order to overcome the overprediction of the streamwise stress component and the underprediction of the shear stress, a higher grid resolution in the wall-normal direction is required. It is demonstrated

by performing an additional simulation (these results were not used as inflow for the backward-step simulations). The grid refinement in both the wall-normal and spanwise direction, even with the coarser streamwise resolution (LES $48 \times 96 \times 48$), significantly improves the results. However, underprediction of the velocity in the viscous sublayer is still present even with the finest grid. A still finer grid resolution in both the wall-normal and spanwise direction would be needed to approach the DNS results. It should be pointed out that the channel flow computations were performed as a prelude to the backward-facing step flow simulations. The intention was not to generate a highly resolved data field, but to apply the LES and DES computational schemes as engineering CFD tools used for analysis in parallel with the standard RANS calculations. The goal was to employ a reasonable grid size being limited to 590,000 CV's, which could be easily handled using a single PC.

6.3.2.2 Backward-facing Step Flow, Unperturbed Case

The backward-facing step computations are conducted with the time dependent, velocity inlet profiles obtained initially with the run $LES-64\times32\times32$. The results of the reference baseline case (without perturbation) are considered first. All the results pertain (if not explicitely stated) to the runs $LES - 220 \times 82 \times 32$ (finer grid) and $DES-142\times82\times16$ (coarser grid), which are denoted simply by LES and DES in the remaining text. The position of the interface, which divides the solution domain into a RANS region and an LES region, resulting from the coarser grid used is at $y/H = 0.128$ at the reattachment ($x/H = 5$), $y/H = 0.171$ ($y^+ = 32$) in the recovery region ($x/H = 15$) and $y/H = 0.361$ ($y^+ = 68$) within the new boundary layer ($x/H = 25$) throughout the flow domain. DES computations on the grid with a significantly finer resolution in the wall-normal direction ($N_y = 110$) is additionally performed (Table 6.2). Similar as in DES of the channel flow, the proper interface location is achieved by slightly extending the spanwise dimension from πH to $4H$, preserving the number of grid points $N_z = 32$. Figs. 6.6-6.7 display some selected results obtained with LES, and DES using considerably different grid resolutions. As already mentioned, the unperturbed case is also computed by DES employing exactly the same grid used for LES. The results obtained are almost identical, as illustrated in Fig. 6.6-left displaying the profiles of streamwise Reynolds stresses. Almost overlapping profiles show that the choice of the SGS model is not that significant, which implies a reasonably fine grid resolution. However, the goal was to investigate the DES performance on coarser grids. It can be argued that a more advanced SGS model, here the grid-dependent S-A model (certainly constrained by its calibration in the RANS mode), would cope better with lower grid resolution and an increasingly anisotropic grid than the simpler, standard Smagorinsky model. This expectation is certainly not fulfilled if the results obtained for unperturbed case are compared, Figs. 6.8-6.10. The largest deviation is documented in the post-reattachment region, coinciding with the lowest streamwise grid resolution in the entire flow domain. Flow recovery is significantly overpredicted as seen from the velocity and turbulence profiles at the streamwise locations $x/H = 8$ and 10. One can argue that the position of the RANS – LES interface in this region of the flow

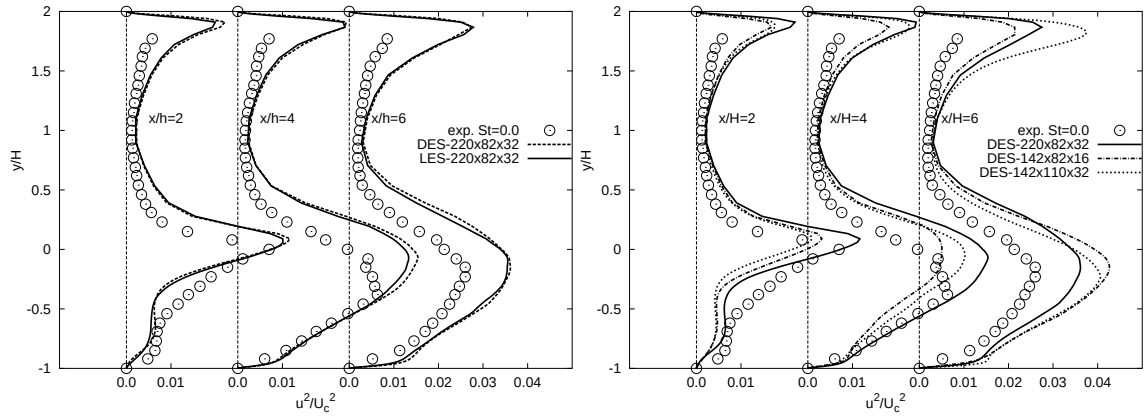

Figure 6.6: LES and DES predictions of the streamwise Reynolds stresses, $St = 0.0$

(around $y^+ \approx 30$) is responsible for such a behavior.

In order to estimate the numerical error in the DES, three different grids are employed for the unperturbed case. Fig. 6.6-right shows computed streamwise Reynolds stresses. At the streamwise location $x = 6H$, one can observe the improvement of results with the grid refinement. However, the reattachment length is still significantly overpredicted due to generally lower grid resolutions, in which case the SGS model plays a more significant role. Presumably, one may expect a larger numerical error in the region just before and just after the reattachment point. This is fortified by comparing the resolved and modeled streamwise Reynolds stresses, as shown in Fig. 6.7.

Figs. 6.8-6.9 show the mean velocity profiles and Reynolds stress components obtained by all three computational schemes (RANS, LES and DES). All computations significantly overpredict the measured reattachment length $X_R/H = 6.0$ (this value represents a corrected value, Obi [52]); the originally reported value corresponds to $X_R/H = 5.5$, Yoshioka et al., [77, 78]: $X_R/H(LES) = 7.18$ (DES using the same grid as LES returns the same reattachment length, see also Fig. 6.6-left for further comparison), $X_R/H(DES) = 8.36$, X_R/H $(RANS\ k-\omega\ SST) = 7.38$

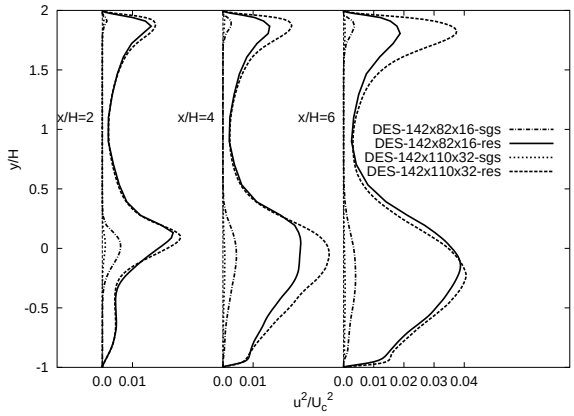

Figure 6.7: Resolved and modelled streamwise Reynolds stresses obtained by DES

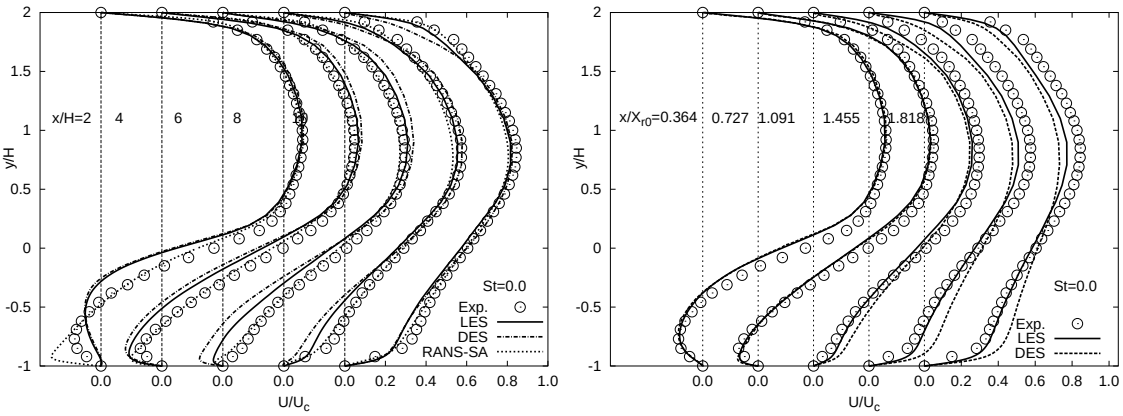

Figure 6.8: Mean streamwise velocity profiles for the unperturbed case ($St = 0.0$) at selected streamwise locations normalized by H (left) and reference reattachment length (right)

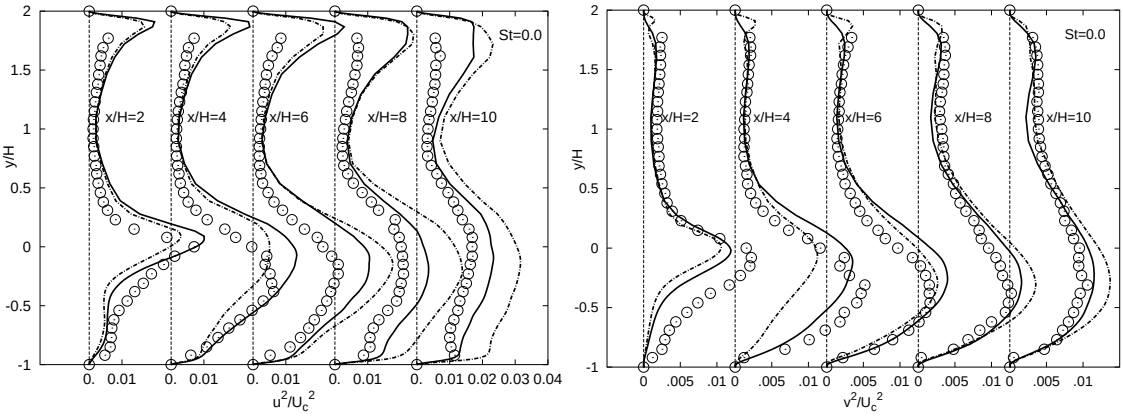

Figure 6.9: Profiles of streamwise and wall-normal stress components, $St = 0.0$

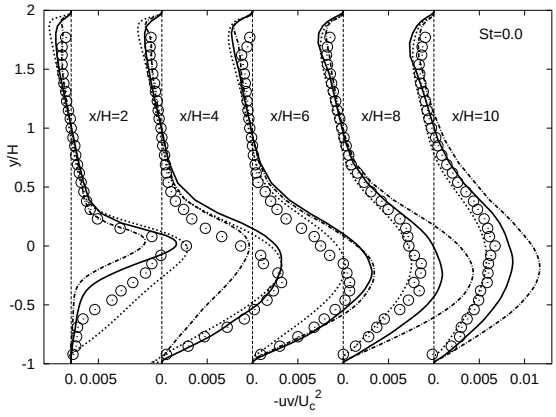

Figure 6.10: Shear stress profiles, $St = 0.0$

and $X_R/H(S-ARANS) = 6.81$. One can observe that the S-A RANS outperforms the LES and DES at all the stations except $x = 2h$. A fact that the reattachment length obtained by S-A RANS is the shortest one and consequently closest to the experimental result is not surprising for this steady case in which the 2-D RANS computation use substantially higher wall-normal resolution $N_y = 110$, whereas the LES and DES use lower grid resolutions (Table 6.2). It is well-known that the eddy-viscosity-based RANS models return traditionally a shorter corner bubble (secondary recirculation zone; it represents an outcome of the action of the normal stress components, which are not reproducible by an eddy-viscosity model scheme) as well as the backflow of a lower intensity, especially in the reattachment region (see e.g., velocity profile at $x/H = 6$ in Fig. 6.8-left). However, the conditions under which the experimental results were obtained should also be pointed out. Particularly important is the aspect ratio based on the channel height after expansion ($3H$) and its spanwise dimension, which was only $1 : 4$. This is regarded as too short for providing a 2-D flow in the mid-span plane. Possibility that the side walls contaminated the results is very high. As already discussed in the previous chapter, Kasagi and Matsunaga [35] performed experiment at a comparable Reynolds number ($Re_H = 5,540$) for the same expansion ratio, whereas the above-mentioned aspect ratio was $1 : 6.7$. Accordingly the reattachment length is substantially larger $X_R/H = 6.51$. In favor of the computational results obtained here is the LES of the same configuration ($St = 0.19$) performed by Dejoan et al. [15], where a reattachment length of $X_R/H = 7.0$ was obtained. Finally, comparison of the velocity profiles at the selected streamwise locations normalized by the corresponding reattachment length (instead of step height) shows very good agreement between LES, DES and experiment in the region of flow reversal, Fig. 6.8-right. Fig. 6.9 shows that the mean Reynolds stresses obtained by LES and DES agree reasonably well with the experimental results in the near field immediately downstream of the step at $x = 2H$ and $4H$. The S-A RANS model generally fails to catch the peak in the separated shear layer. At the last three streamwise locations the streamwise stresses are overpredicted, which is characteristic for a somewhat lower grid resolution in this flow region. The performance of LES and DES may be explained by the following facts: the inflow data, grid resolution and spanwise dimension may have a great impact on the results. Underprediction of the computed turbulence intensities in the precursor channel flow simulations could lead to such an overestimate of the reattachment ($7.18H$), compared to the measured value ($6.0H$; Obi, [52]). Indeed, the influence of inflow turbulence is crucial for predicting the flow downstream as will be discussed later. Furthemore, the grid resolution, especially in the spanwise direction, might be insufficient. At the same time, the spanwise domain size of πH could be responsible for the overprediction of the reattachment length. Arnal and Friedrich [5] indicated that the choice of the spanwise dimension is of decisive importance. They concluded that an overprediction of the reattachment length up to 30% could occur if the size of the flow domain in the spanwise direction was of the order less than $4H$. They found that $L_z \geq 8H$ was necessary to eliminate the influence of the periodic inlet/outlet through the side planes of the computational box. In order to check the latter, two additional simulations with substantially refined grid

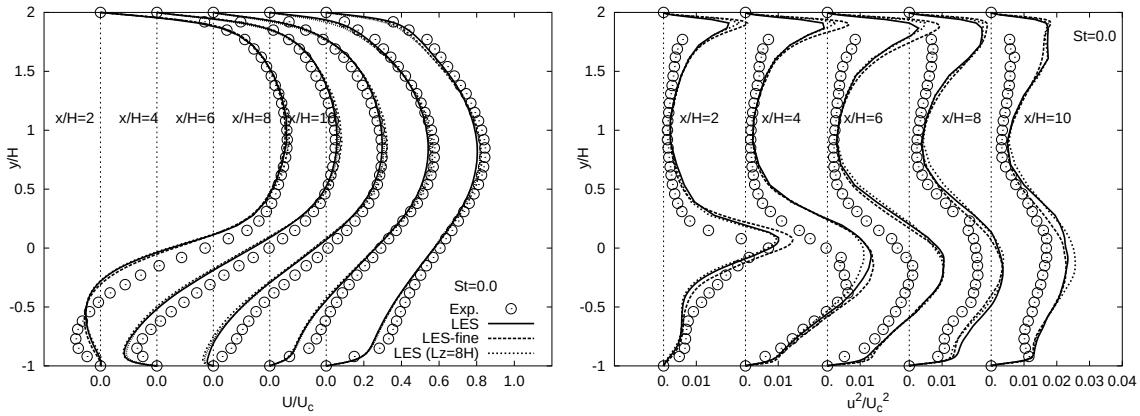

Figure 6.11: Influence of the grid resolution and spanwise domain size: mean streamwise velocity and Reynolds stresses obtained by LES, $St = 0.0$

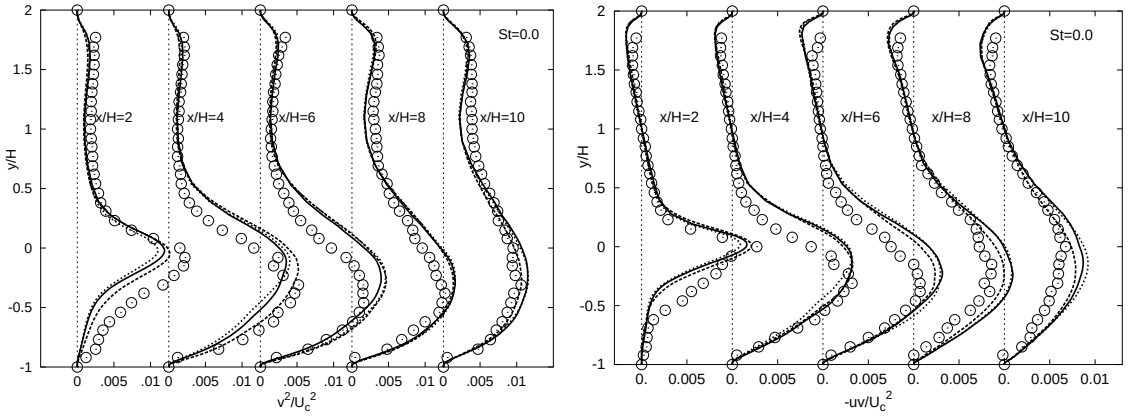

Figure 6.12: Influence of the grid resolution and spanwise domain size: Wall-normal and shear stresses obtained by LES, $St = 0.0$

(LES - $354 \times 110 \times 32$) and significantly larger spanwise domain dimension (LES - $220 \times 82 \times 64$, $L_z = 8H$) are performed. The results for both first and second moments show no significant differences in comparison with the reference LES (LES - $220 \times 82 \times 32$, $L_z = \pi H$) as demonstrated in Figs. 6.11 and 6.12. Hence, the grid sizes adopted for the reference simulations can be regarded as the optimal ones. Though normalization by the reference reattachment length X_{R0} might partially compensate for the 3-D contamination which was likely present in the experiments, the results normalized by the step height H will be compared henceforth. The main issue is to study the effects of perturbations on flow characteristics compared to the reference unperturbed flow. The results of simulations of the perturbed flow configurations are presented and compared with the reference data in the following section.

6.3.2.3 Backward-facing Step Flow, Perturbed Cases

A computational investigation is undertaken focussing on the influence of the oscillatory blowing/suction on the reattachment pattern for all perturbation frequencies

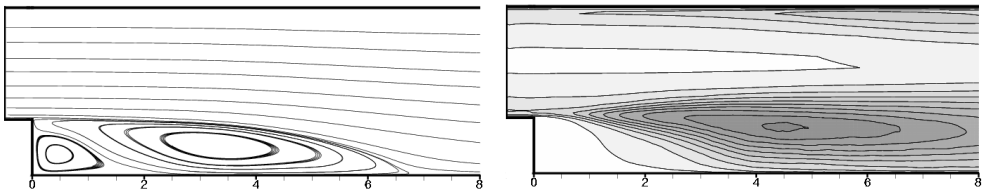

Figure 6.13: Time-averaged streamlines and turbulent kinetic energy contours ($St = 0$)

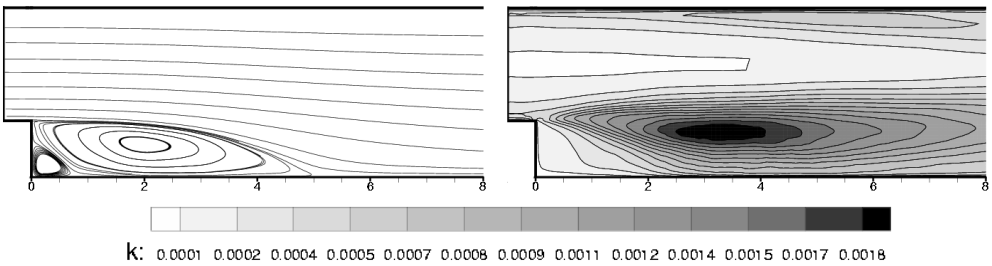

Figure 6.14: Time-averaged streamlines and turbulent kinetic energy contours ($St = 0.19$)

treated experimentally: $St = 0.08, 0.19$ and 0.30. The main effect of the oscillatory blowing on a separated shear layer is that it reattaches earlier due to momentum transfer enhancement caused by an increase in turbulence production. Figs. 6.13 and 6.14 display the time-averaged streamlines and contours of the kinetic energy of turbulence behind the step obtained by LES for both perturbed ($St = 0.19$) and unperturbed ($St = 0$) flow cases. The increase in turbulence intensity in the shear layer (denoted by a dark area) and consequent shortening of the mean recirculation zone are clearly recognizable. The main effect of the perturbation is reproduced by LES and DES as illustrated in Fig. 6.15, where the perturbation effectiveness can be deduced by analysing the mean skin-friction distributions at the bottom wall. Secondary corner separation bubble is captured by all simulations. The size of the bubble appears to be significantly reduced only for higher perturbation frequencies ($St = 0.19$ and 0.30). At the same time, the maximum and minimum levels of skin-

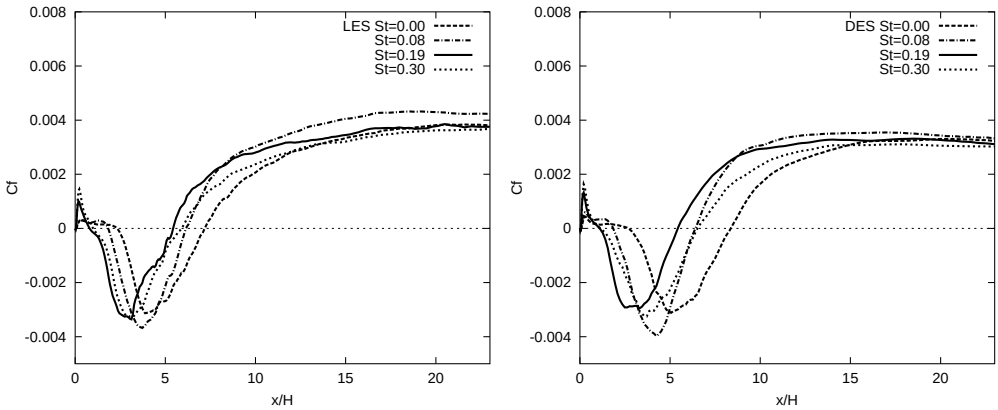

Figure 6.15: Skin-friction coefficient at the bottom wall downstream of the step for various perturbation frequencies

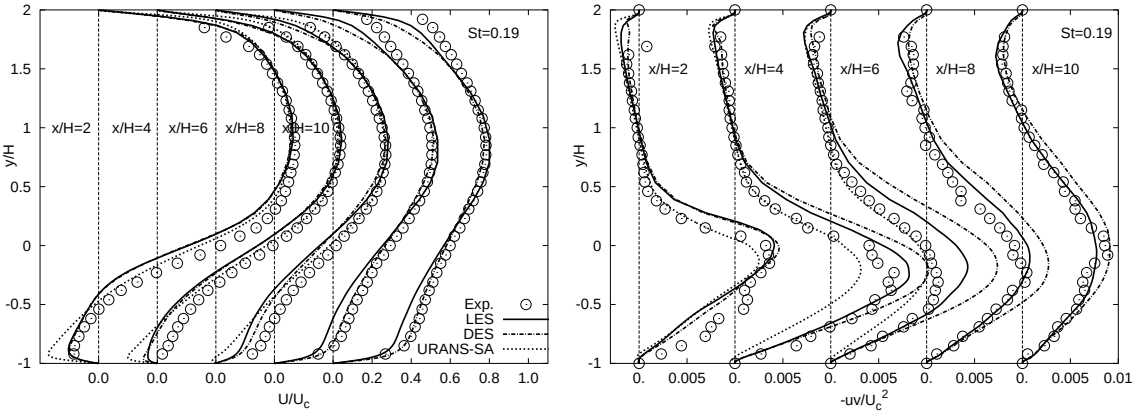

Figure 6.16: Mean streamwise velocity (left) and shear stress (right) profiles, St=0.19

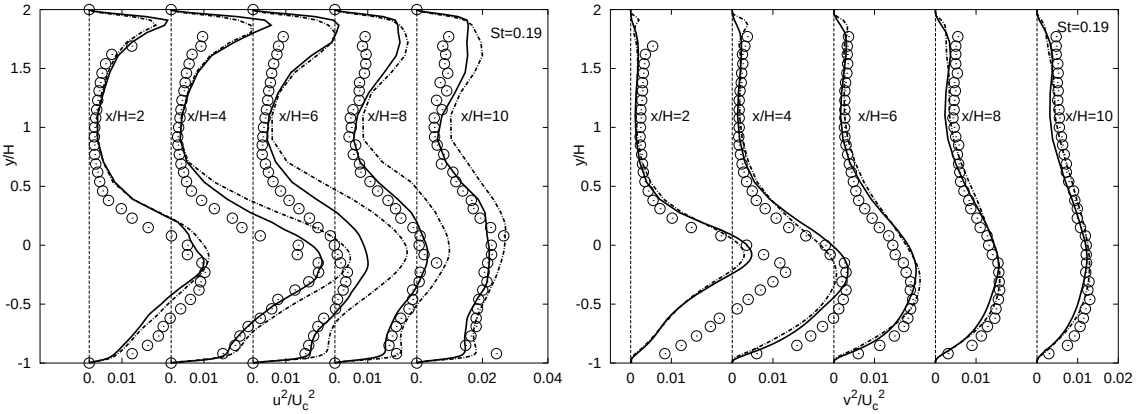

Figure 6.17: Profiles of streamwise and wall-normal stresses, St=0.19

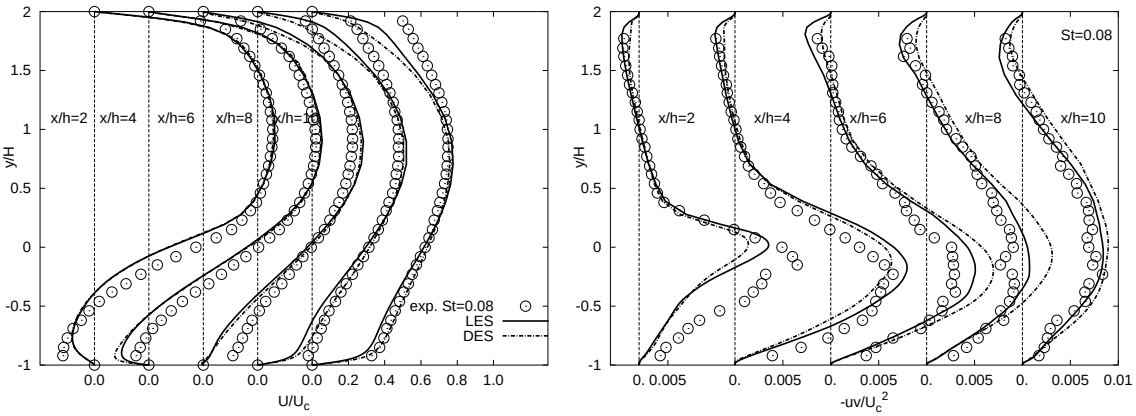

Figure 6.18: Mean streamwise velocity (left) and shear stress (right) profiles, St=0.08

friction obtained by LES and DES are not significantly affected by the perturbation, except for the lowest frequency case ($St = 0.08$). At this perturbation frequency DES, and particularly LES predictions, indicate that flow recovery downstream of the reattachment is promoted.

Figs. 6.16 to 6.17 display the profiles of mean axial velocity and three Reynolds stresses ($\overline{u^2}$, $\overline{v^2}$ and $\overline{uv}$) for the optimum perturbation frequency in all characteristics regions behind the step: within the recirculation zone ($x/H = 2$ and 4), close to reattachment ($x/H = 6$), and in the flow recovery region ($x/H = 8$ and 10). It can be seen that both the LES and DES predictions are generally in better agreement with the experimental data, when compared to the unperturbed case. Similar behavior is obtained for the other two perturbation frequencies, $St = 0.08$ and $St = 0.30$, as demonstrated in Figs. 6.18-6.21. Exceptions are observed at the stations $x = 4H$ and $6H$. These discrepancies in the lower near-wall region are associated with a slight underprediction of the inlet turbulence, as will emerge later. On the other side, underprediction of the streamwise velocity in the upper near-wall region in the post-reattachment zone at $x = 8H$ and 10 can be attributed to insufficient grid resolution. A noticeable difference can be seen in the wall-normal stress profiles, which are consistently underpredicted at the position immediately downstream of the step ($x = 2H$) for all frequencies investigated. This may be related to the inlet boundary conditions (note underprediction of the $\overline{v^2}$ stress component in Fig. 6.4-left).

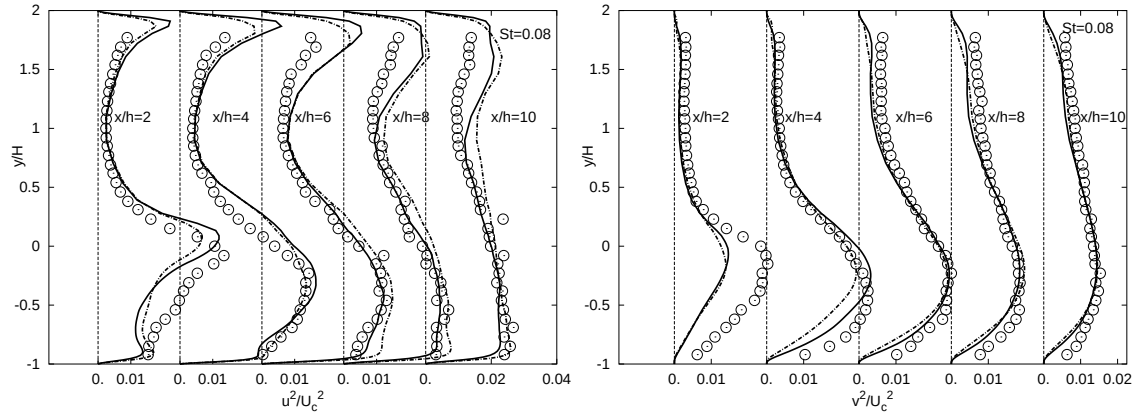

Figure 6.19: Profiles of streamwise and wall-normal stresses, St=0.08

The influence of perturbation frequency on the intensity of backflow in the mean recirculation zone, as well as on the size (length and height) of separation bubble itself, is documented in Fig. 6.22-left. The obvious shortening of the reattachment length can also be deduced from the position of zero value of the mean velocity, being closest to the wall in case of the optimal frequency, $St = 0.19$. Fig. 6.22-right shows the profiles of streamwise stress component for all perturbation frequencies considered, closely following the experimental results. Fig. 6.23 displays evolution of the reattachment length (normalized by the reattachment length obtained for the unperturbed case X_{R0}) with the imposed perturbation frequency. Although the quantitative agreement between experimental and computational results is rather poor, it is encouraging to see that also the URANS computations using S-A and $k-\omega$

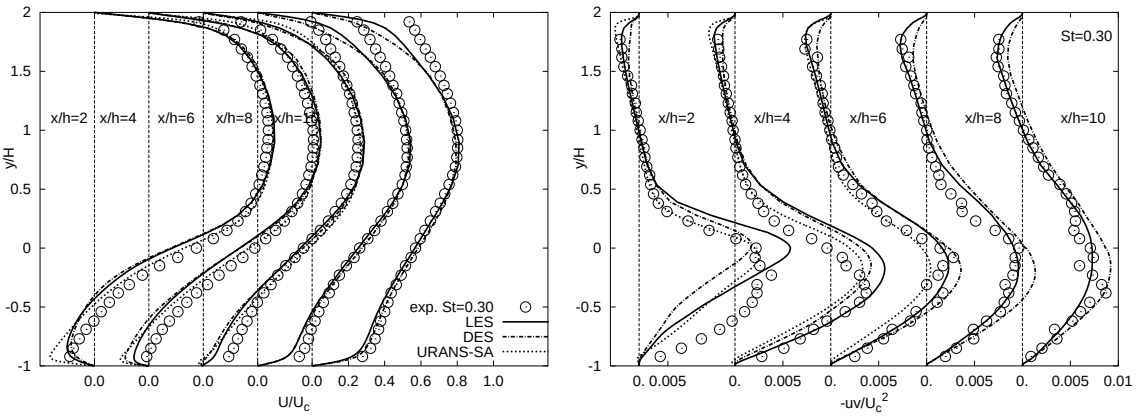

Figure 6.20: Mean streamwise velocity (left) and shear stress (right) profiles, St=0.30

SST statistical models reproduce a reduction of the reattachment length with respect to the unperturbed case ($St = 0.0$), and that the minimum reattachment length is reached at the position $St = 0.19$, comparing well with experiment. However, the relative decrease is too small. The URANS method employing S-A (only 5.9 % compared to the unperturbed case) and $k - \omega$ SST (12.9 %) models results in a very weak sensitivity to the perturbation. Contrary, very close agreement with experiment is obtained with the DES (24.5 %) and LES (35 %) methods. Fig. 6.23-right documents the well-known weakness of RANS models, namely very low turbulence intensities (here the shear stress component is shown) in the separated shear layer. As already discussed, the proper level of turbulence in this region is of crucial importance for accurate prediction of the flow reattachment. The reason for such a result lies in the unsteady nature of the flapping motion of the separated shear layer (Fig. 6.24-left) and oscillation of the instantaneous reattachment point (Fig. 6.24-right), which cannot be fully reproduced by RANS models.

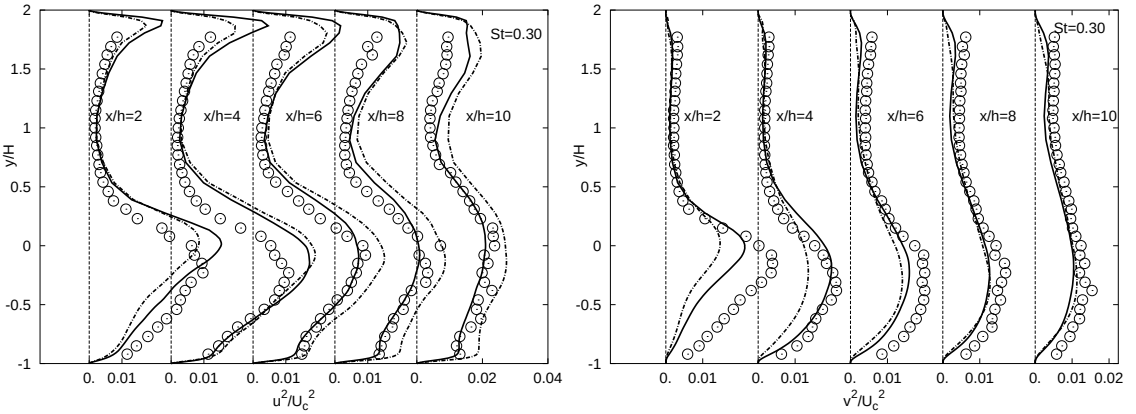

Figure 6.21: Profiles of streamwise and wall-normal stresses, St=0.30

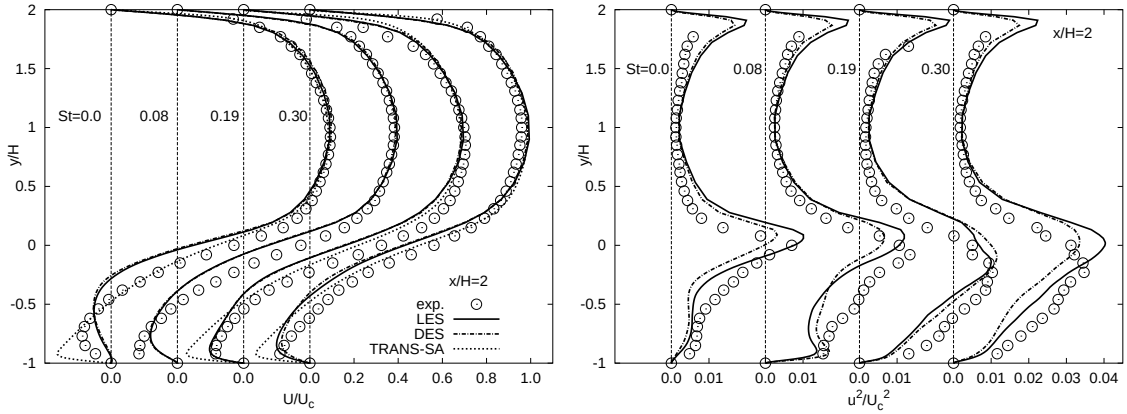

Figure 6.22: Mean velocity and streamwise stress dependence on the perturbation frequency in terms of St

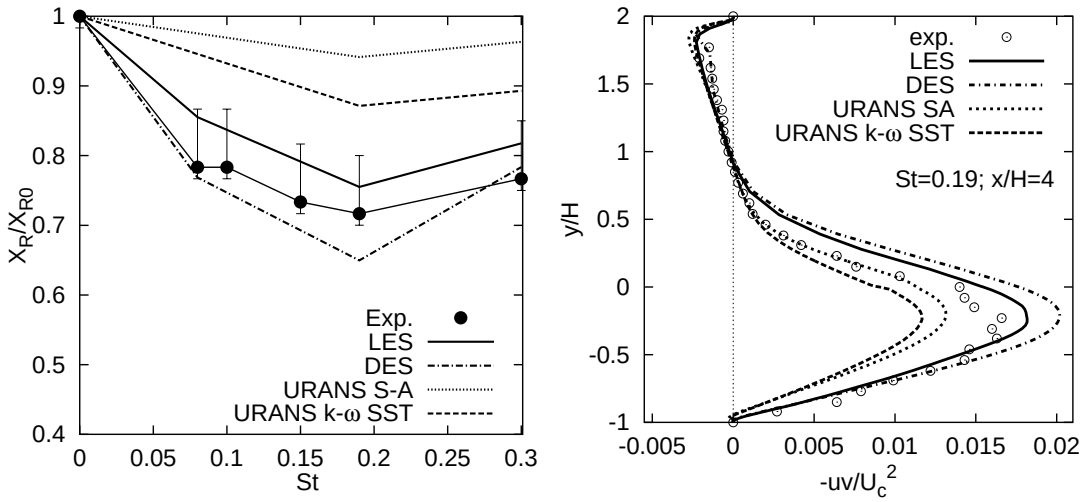

Figure 6.23: Evolution of the relative reattachment length (left); Predictions of the peak shear stress in the separated shear, $St = 0.19$

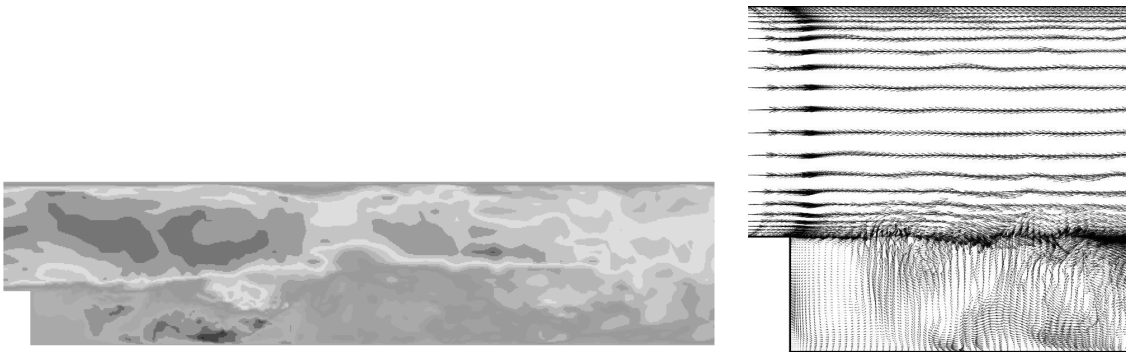

Figure 6.24: Instantaneous velocity contours and vectors, $St = 0.19$

6.3.2.4 Frequency Characteristics of the Mean Flow Structure

As LES and DES are found to significantly outperform RANS method, the results obtained by LES and DES for all perturbation frequencies will be compared against the experiment at various streamwise locations. The frequency character-

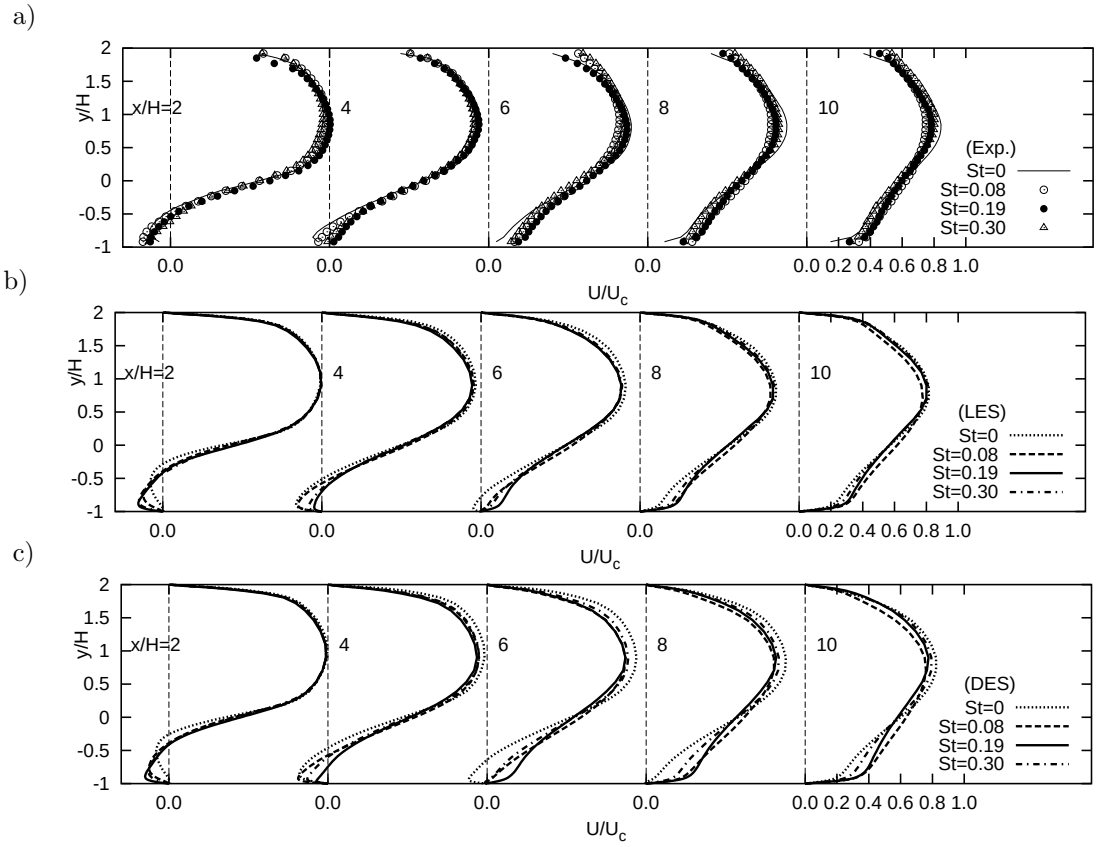

Figure 6.25: Overall comparison of mean streamwise velocity profiles at various streamwise locations, $St = 0, 0.08, 0.19$ and 0.30

istics of the mean flow can be investigated by careful inspection of Fig. 6.25 which displays response of the mean streamwise velocity to the perturbation. In the region immediately behind the step ($x/H = 2$), the experimental results reveal that there is almost no difference among the profiles. The same trend is reproduced by LES and DES, the only exception being the unperturbed case. The issue of 3-D contamination in the experiments, as already discussed, is deemed responsible for this outcome. As shown in Figs. 6.26-6.29, the effect of perturbation at $x/H = 2$ is expressed by an increase in turbulence level across the separated shear layer. The simulations return this increase in both normal and shear stress components. Despite certain underpredictions of the wall-normal stresses in general its striking enhancement relative to the unperturbed case (by a factor 4 for the optimum, and by a factor 3 for other two frequencies) is qualitatively captured. The level of $\overline{v^2}$ may be linked to the momentum transport due to turbulent mixing in the separated shear layer. It is clearly recognized that reduction in the reattachment length follows the evolution of $\overline{v^2}$ at this station, $x/H = 2$.

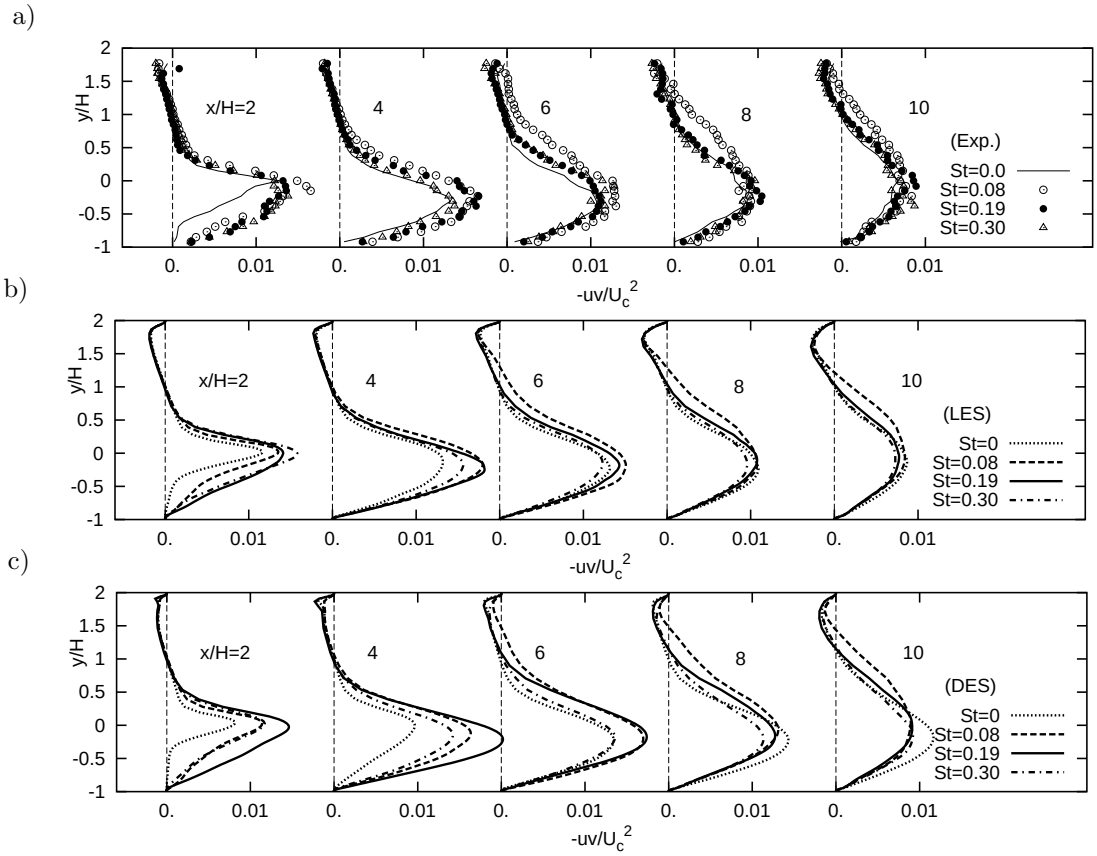

Figure 6.26: Overall comparison of shear stress profiles at various streamwise locations, $St = 0, 0.08, 0.19$ and 0.30

At the following measurement location ($x/H = 4$) one can observe that no reverse flow occurs in the experiment with the optimum-frequency perturbation, $St = 0.19$. Simulations do not fully return this feature, the backflow is still visible, albeit significantly weaker. Nevertheless, a consistent decrease in the backflow velocity depending on the perturbation frequencies is predicted by both LES and DES. The level of turbulent stresses is correctly represented by LES, whereas DES yield somewhat poorer results (note substantial overprediction of $\overline{u^2}$ in Fig. 6.27) likely due to insufficient resolution in this highly-strained region of the flow. The simulations follow the position of the $\overline{u^2}$ peak, which is shifted from the central region of the shear layer (at $St = 0.19$) closer to the bottom wall at lower frequency, $St = 0.08$. Interestingly, $\overline{u^2}$ is mostly affected in the near-wall region by the lower frequency perturbation. Furthermore, all stress components are increased in the experiment at $St = 0.08$ in the region of $y/H \geq 0.5$. This behavior is also captured by the simulations. The experiments and simulations suggest that the flapping motion of the separated shear layer, as a mechanism responsible for such a modification of the turbulence field, is most effective at the lower frequency perturbation.

The remaining streamwise locations, $x/H = 6, 8$ and 10 correspond to the regions of reattachment and flow recovery. Regarding mean streamwise velocity profiles, LES and DES follow similarly the tendency observed in the experiments

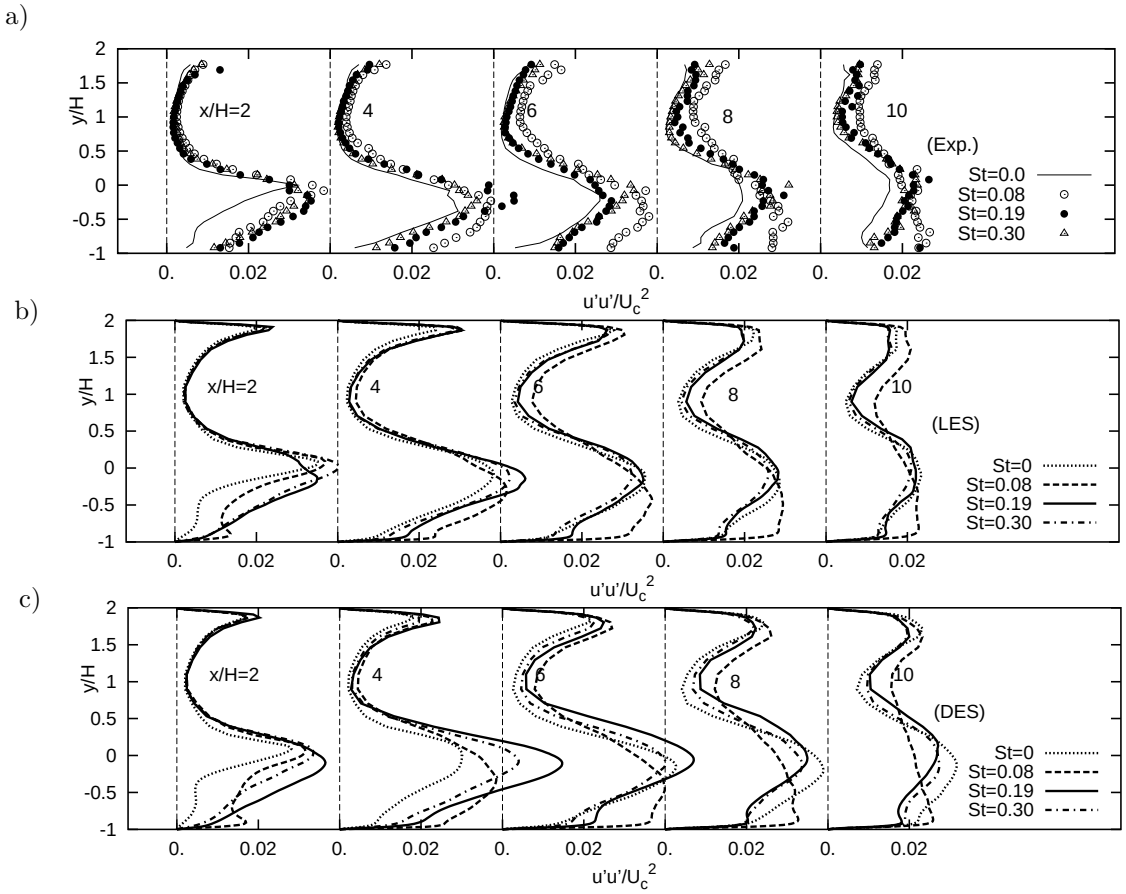

Figure 6.27: Overall comparison of streamwise stress profiles at various streamwise locations, $St = 0, 0.08, 0.19$ and 0.30

at $x/H = 6$. A remarkable difference is present in DES of the $St = 0.19$ case in the near-wall region. Relative to the other two frequencies, flow recovery is overpredicted with respect to the reference data. This is an indication that DES might suffer from insufficient streamwise resolution in this region, which manifests itself by typical overpredictions of both $\overline{u^2}$ and $\overline{uv}$ (Figs. 6.26 and 6.27). Response of the mean flow to the perturbation in the recovery region ($x/H = 8$ and 10) is credibly represented by LES and DES, the only exception being DES of the unperturbed case. It seems that DES, and to a certain extent LES, are more susceptible to the grid resolution in this flow region for $St = 0$. Second moment distributions are also in agreement with the experimentally documented trend. The simulations reproduce experimentally observed increase in turbulence level for the lower frequency case in the region of $y/H \geq 0.5$. It is to be pointed that streamwise stress increase in the near-wall region is fully captured as well. All these observations imply that there exists an increased vortex activity in this flow region. As a consequence of vortex stretching, the spanwise stress increases significantly as displayed in Fig. 6.29 which show LES predictions of this stress component. In accordance with the experiments, the response of the flow turbulence to perturbations is such that three different frequencies can be identified. The optimum frequency, $St = 0.19$,

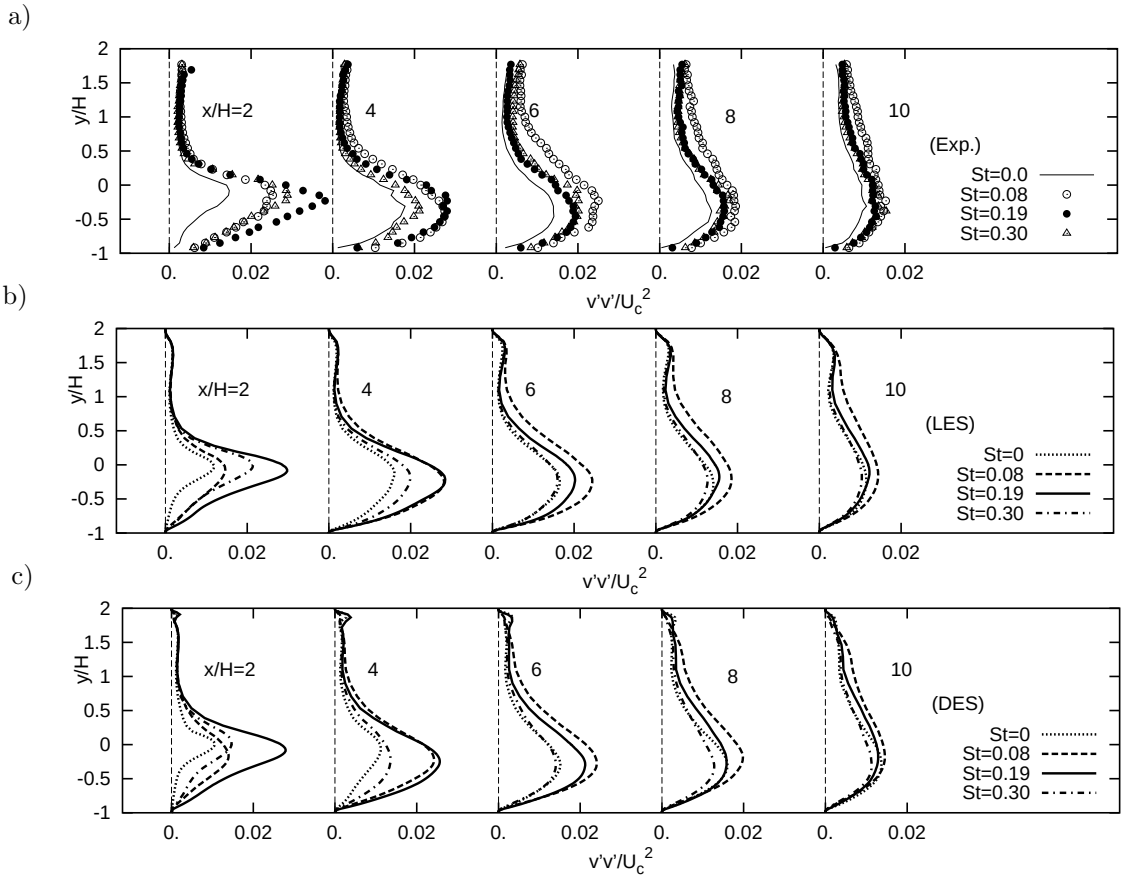

Figure 6.28: Overall comparison of wall-normal stress profiles at various streamwise locations, $St = 0, 0.08, 0.19$ and 0.30

promotes turbulence production in the region behind the step where a substantial increase in the spanwise stress is clearly noted. Unlike the optimum one (the most effective in terms of reattachment reduction), the two remaining frequencies, the lower ($St = 0.08$) and higher ($St = 0.30$), have a comparable influence on the reduction of the reattachment. However, by careful inspection of 6.29, one can distinguish different responses of the flow; at the lower frequency, there exists a significant increase in the spanwise stress in the near-wall region, in particular at the station $x/H = 6$. On the other side, the enhanced turbulence production excited by the higher frequency is evident only just downstream the step (note the peak of $\overline{w^2}$ at $x/H = 2$), dissipating rapidly further downstream. These modifications of the flow structures can be seen in Fig. 6.30 which visualize the flow at various perturbation frequencies. Note that the iso-surfaces of the instantaneous pressure fluctuation are extracted for arbitrary phase angles, thus representing a 'snap-shot' of the flow structure. Nevertheless, one can identify a certain tendency of flow modification with respect to the unperturbed case (Fig. 6.30-a). The optimum frequency (Fig. 6.30-c) gives rise to the enhanced vortical motion in the recirculating region of the flow. Fig. 6.30-b represents the response to the lower frequency excitation, a higher interaction of the vortices with the wall in the post-reattachment region is recognized. Finally, the higher frequency perturbation (Fig. 6.30-d) causes

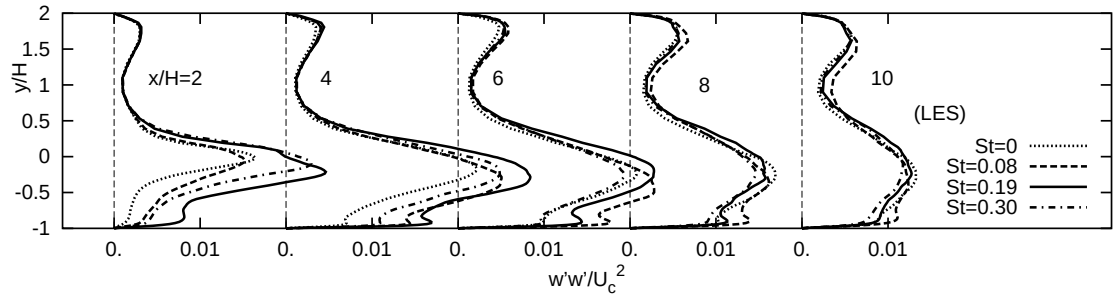

Figure 6.29: LES predictions of spanwise stress component at various streamwise locations, $St = 0, 0.08, 0.19$ and 0.30

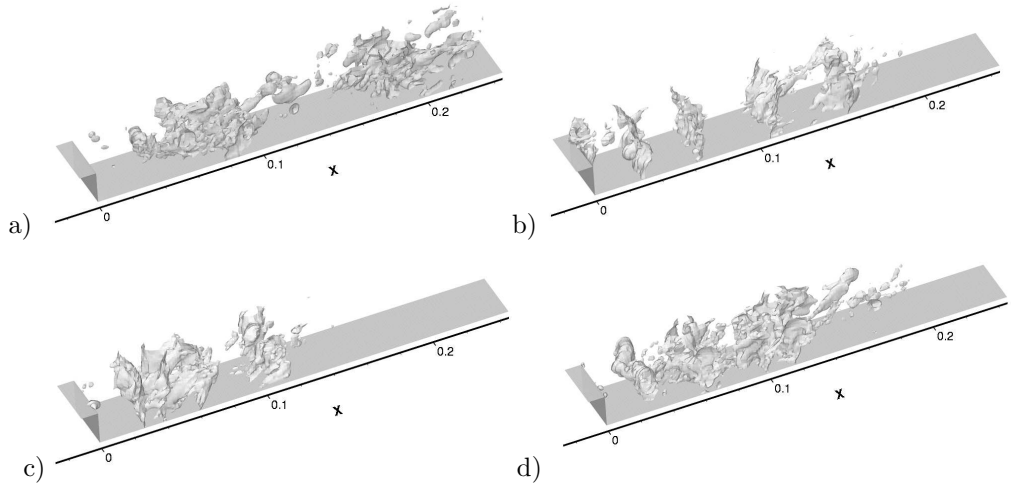

Figure 6.30: Iso-surfaces of pressure fluctuations obtained by LES for different perturbation frequencies: a) $St = 0$, b) $St = 0.08$, c) $St = 0.19$ and d) $St = 0.30$

a remarkable vortex stretching only in the region just behind the step (already confirmed by the peak of $\overline{w^2}$ at $x/H = 2$), rapidly decaying further downstream where the flow structure resembles the one of the unperturbed flow.

6.3.2.5 Influence of the Inlet Boundary Conditions

The influence of the inlet boundary conditions on the flow predictions need some additional considerations. In order to assess sensitivity of the flow to the upstream turbulence, two additional simulations of the unperturbed flow are performed imposing the inlet profiles obtained by another pre-cursor LES of a plane channel flow with the Smagorinsky constant $C_s = 0.065$ used along with the Van Driest damping function in the near-wall region. Fig. 6.31 compares predictions of the mean streamwise velocity and turbulence intensities to the reference simulation used to generate inflow boundary conditions for the majority of LES and DES of the backward-facing step flow. The damping of C_s yields better behavior of the mean velocity in the viscous sublayer but friction velocity is underpredicted ($Re_\tau = 178$ compared to the LES reference value $Re_\tau = 188$), centerline velocity consequently

being overpredicted in the core flow. The turbulence intensities are displayed in Fig.6.31-right. In absence of the near-wall measurements, by careful inspection of the experimental results, one can note the new simulation follows the experimental gradient of the streamwise stress. It seems that capturing the near-wall turbulence, especially the wall-normal component, has an impact on the mean flow downstream the step. Indeed, this assertion is supported by the results of two LES runs (LES1- the standard Smagorinsky model with $C_s = 0.1$ and near-wall damping, LES1-DSM - the dynamic Smagorinsky model) as demonstrated in Fig. 6.32. As it has already been shown that results virtually do not change regardless of the grid or SGS model employed (cf. Figs. 6.6, 6.11 and 6.12) these two LES runs conducted with a somewhat higher inflow turbulent intensity demonstrate the influence of the inlet turbulent intensity on the flow prediction downstream the step. An essential improvement of the results is noted around the reattachment and further downstream, as far as the mean velocity is concerned (6.32-left). On the other side, except the station $x = 4H$ where the resulting $\overline{v^2}$ improves yielding more accurate prediction of the flow reattachment, turbulence profiles are even deteriorated at $x \geq 6H$ (see $\overline{v^2}$ distribution in Fig. 6.32-right). Along with overprediction of the stress level, the position of the stress peak moves towards the wall following the experiment. Keeping in mind all uncertainties associated with the experiment (3-D contamination due to the side-wall effects, possible departure from the fully developed flow conditions at the inlet), it is supposed that the imposed inlet profiles are not significantly influential. Recall that the main issue is to study response of the flow and turbulence to the perturbation relative to the reference case, noting that all simulations have the same inlet boundary conditions. Finally, the LES results of Dejoan et al. [15] for the two cases ($St = 0$ and $St = 0.19$) support this supposition.

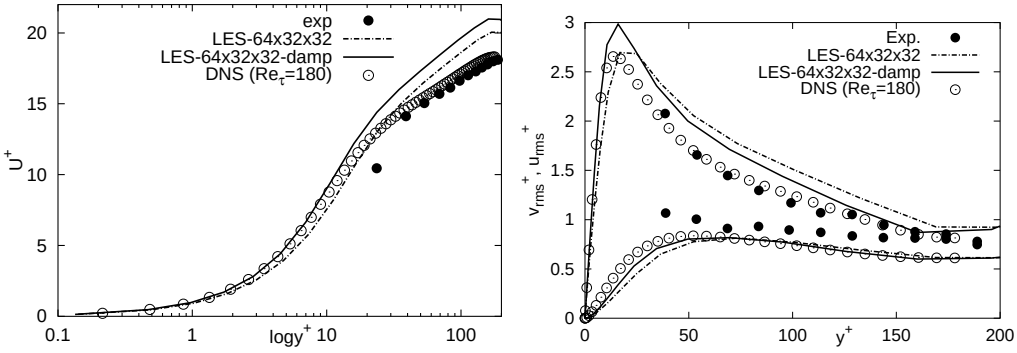

Figure 6.31: Comparison of pre-cursor LES of a plane channel flow: Semi-log profiles of the mean velocity (left) and turbulence intensities (right)

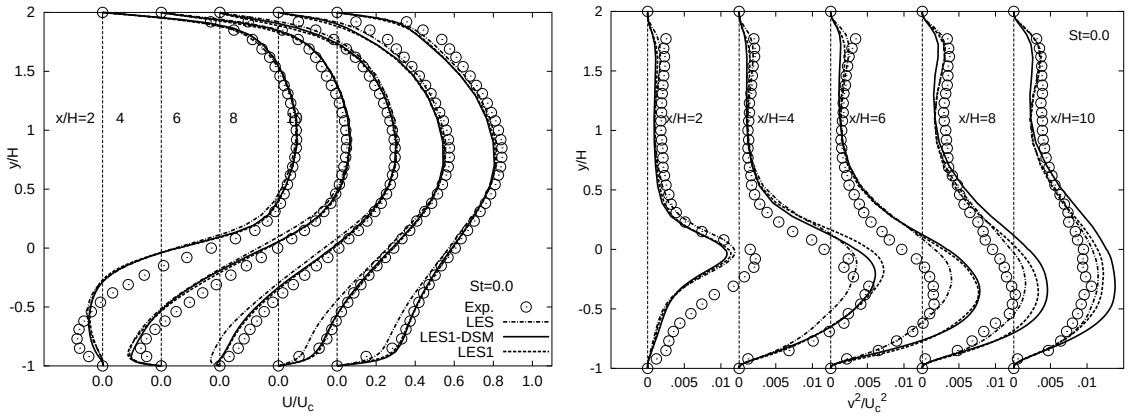

Figure 6.32: Influence of the inlet turbulence on the mean flow downstream the step; Profiles of mean streamwise velocity and wall-normal stresses, St=0

6.3.2.6 Phase-averaged Flow Field

In order to investigate behavior of the phase-averaged flow field, an additional LES run using the above mentioned new inlet data and dynamic variant of the Smagorinsky model is conducted. The samples of instantaneous flow field (for the phase angles ϕ=0, $\pi/2$, π and $3\pi/2$) are collected over a period of 50 injection cycles. The number of samples is limited (Dejoan et al. [15] recently presented the phase-average results based on 15 injection cycles) compared to the experiment (1000 samples), nevertheless, the resulting phase-averaged flow field provide useful information about the mechanisms and processes underlying the flow control by means of periodic excitation. The phase-averaged flow fields at the selected phase angles can be represented by the phase-averaged streamlines displayed in Fig. 6.33-left. Typical presence of two to three vortices observed in the experiment (see Fig. 6.33-right) is reproduced confirming the existence of organized vortex motion behind the step. The large-scale vortices emerging from the step edge are found to move downstream at a velocity roughly equal to 0.3 U_c (this experimental observation is denoted by the dashed lines in Fig. 6.33- right). The present LES compares well with the experiment yielding a convective speed of $U_{cv} = 0.36U_c$ (Dejoan et al. [15] reported a movement of the structures at a speed of $U_{cv} = 0.4U_c$). The experimental findings point to the fact that there exists a remarkable increase in stress production due to the organized vortex motion behind the step. The region between two adjacent vortices is characterized by significant straining of the flow resulting in the stress production. The phase-averaged shear stress profiles obtained by LES are displayed in Fig.6.34, exhibiting a close agreement with the experiment. In order to elucidate a motion of the flow structures in the periodically perturbed flow, the instantaneous iso-surfaces of vorticity colored by pressure at four characteristic phase angles are displayed in Fig. 6.35. At the instant corresponding to the phase angle $\phi = 0$ (Fig. 6.35-a), two vortices are present in the region behind the step. The first one which emerged rolling up from the step is clearly discernable by the pressure minima (dark blue region). The vortex stretching in the spanwise direction is followed by its breakup and consequent helical pairing downstream, whereas the

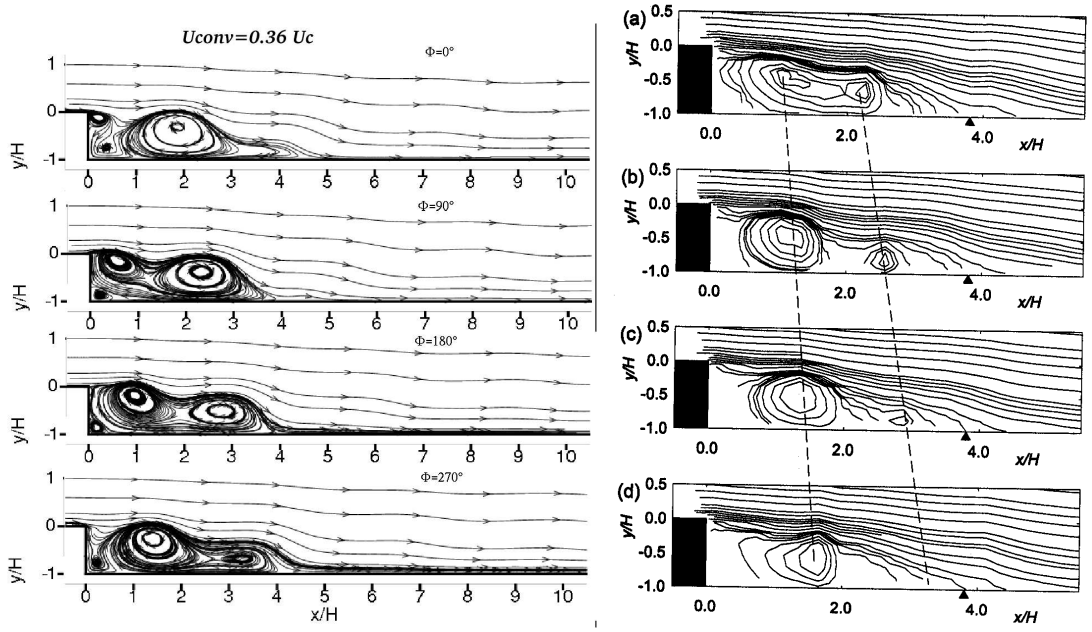

Figure 6.33: Phase-averaged streamline patterns, $St = 0.19$; LES predictions (left), experiment (right)

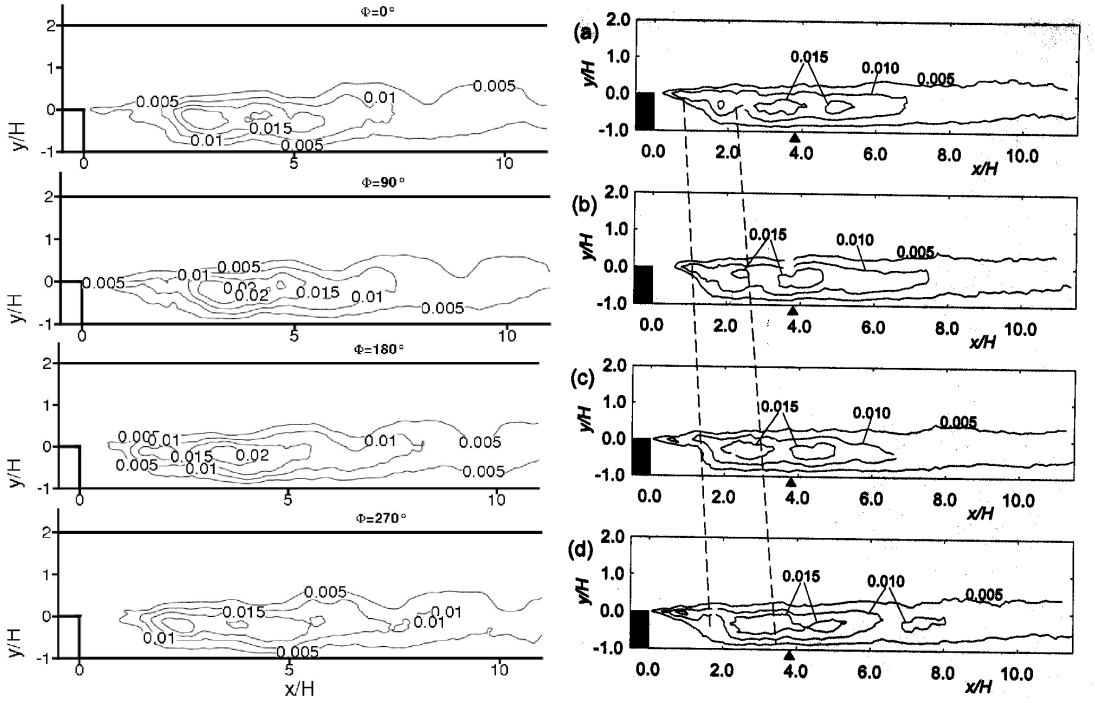

Figure 6.34: Phase-averaged Reynolds shear stress contours $- < uv > /{U_c}^2$, $St = 0.19$; LES predictions (left), experiment (right)

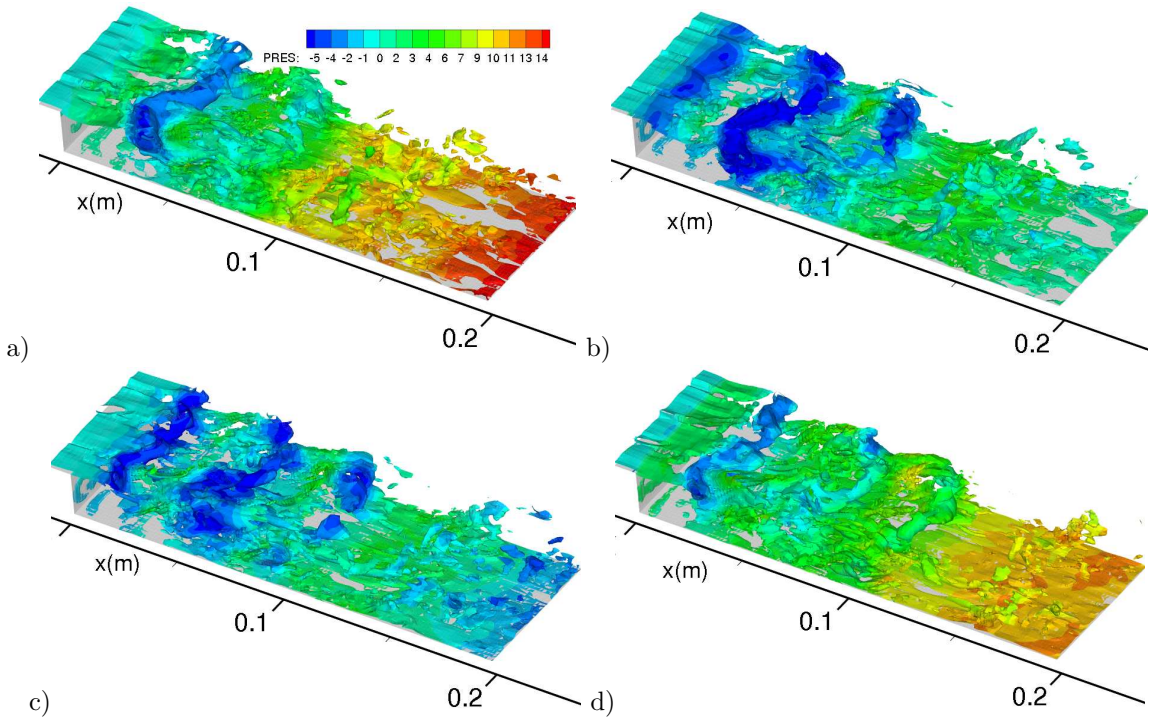

Figure 6.35: Iso-surfaces of vorticity colored by pressure obtained by LES, $St = 0.19$; a) $\phi = 0$, b) $\phi = \pi/2$, c) $\phi = \pi$ and d) $\phi = 3\pi/2$

second vortex interacts with the wall being disrupted with the traces visible further downstream (Fig. 6.35-b). At $\phi = \pi/2$ the injection peak is reached resulting in formation of the next vortex at the step edge. The three vortices (recognized by a dark blue color) are convected downstream without major structural modification as seen in Fig. 6.35-c showing the flow topology at an instant corresponding to the switch from injection to suction cycle ($\phi = \pi$). As the suction peak is reached at $\phi = 3\pi/2$, the abovementioned structures can not be clearly distinguished (see Fig. 6.35-d). One can observe a strong interactions between the vortices with a tendency of pairing and stretching in the streamwise direction. As the injection/suction period is completed, the coherent structures appear to be separated from the step which is also shown by the phase-averaged streamlines in Fig. 6.33 ($\phi = 3\pi/2$).

Concluding Remarks

A potential of the methods for unsteady flow computations: LES, DES and URANS was investigated by predicting the flow and turbulence field for a backward-facing step flow configuration perturbed by a periodic blowing/suction with zero-net-mass flux from a thin slit situated at the step edge. In general, both the LES and DES computations have reproduced all important effects observed in the experiment. The imposed perturbation frequency corresponding to $St = 0.19$ was found to be the optimum, leading to the maximum reduction of the reattachment length. Compared to the measured value of 28.3%, LES and DES exhibit the closest agreement, predicting the reduction of 24.5 and 35%, respectively. URANS underpredicts

substantially the intensity of the reduction with 5.9% (S-A model) and 12.9% ($k-\omega$ SST model), exhibiting a very weak sensitivity to the perturbations. The grid resolution and spanwise size of the computational domain and their relation to an overprediction of the absolute reattachment length for both LES and DES were discussed. However, a further grid refinement, as well as a doubling of the spanwise dimension did not result in any significant change. The wall-normal and shear stress components, including also the wall shear stress at the step edge obtained from the precursor simulation of a plane channel flow were slightly underpredicted compared to the experiment. A computational analysis of the influence originating from the inflow boundary conditions has shown that there is a certain impact of the inlet turbulence intensity on the flow around and downstream the reattachment. However, it is believed that the imposed inlet profiles are not appreciably influential. Since all simulations have the same inlet boundary conditions, it is possible to explore response of the flow and turbulence to the perturbation relative to the reference unperturbed case. Overall comparison of the mean flow and turbulence for different perturbation frequencies has shown a close agreement with the experimentally observed trends. Not only a general enhancement of the turbulence production with the perturbation was reproduced but also the frequency dependence of the Reynolds stress increase. Some peculiarities in the stress field arising from the flapping motion of the perturbed shear layer were captured by LES and DES. Beside a close agreement with the experiment concerning time-mean behavior of the flow for all perturbation frequencies, the extracted phase-averaged LES results for the case with the optimum frequency ($St = 0.19$) compare well with the reference experimental data.

7 High-Re Number Flow over a Wall-mounted Hump with Separation Control

The predictions of the separated flow over a wall-mounted hump at high Reynolds number, which has recently attracted attention of the CFD community, will be presented in the remaining text. The flow separation from smooth surfaces is an important phenomenon relevant to the aircraft dynamics that requires a special attention. The flow complexity and predictive capabilities of CFD for the baseline configuration have already been demonstrated in Chapter 5. A concise description of the experimental configuration and measurements will be outlined next, followed by comparison and discussion of the results for the hump flow with separation control.

7.1 Separated Flow over a Wall-mounted Hump

Originally, this flow has been experimentally studied by Seifert and Pack [64, 65]. The turbulent flow over a wall-mounted hump (Fig. 7.1, simulating the upper surface of a Glauert-Goldschmied type airfoil at zero angle of attack) at a high Reynolds number of $Re_c = 9.36 \cdot 10^5$ (based on the free-stream velocity $U_\infty = 34.6\ m/s$ and the chord length $c = 0.42\ m$) situated in a plane channel (height $0.909c$) was experimentally investigated at the NASA Langley Research Center (Greenblatt et al. [23, 22]) for the purpose of the CFDVAL workshop on computational methods and turbulence models validation (Rumsey et. al [58]). The same test case was studied at the 11^{th} ERCOFTAC workshop on refined turbulence modeling (Johansson and Davidson [33]).

This test case has been considered as the best defined of all three cases considered at the NASA Workshop. It is nominally two-dimensional, although the end plates bring some 3D effects. The hump is 420 mm long with the crest of 53.7 mm and is mounted on a splitter plate of thickness 12.7 mm, which extends 1,935 mm upstream from the hump leading edge and 1,129 mm downstream from the hump leading edge. The hump with the splitter plate is placed in a wind tunnel of 771 mm width and 508 mm height, but the nominal test section height (between the splitter plate and the top wall) is 382 mm and the nominal hump width (between the two end plates) is 584 mm (Fig. 7.1-left). Results containing base plate pressure and friction factor, and PIV of mean U and V velocity, uu, vv and uv stress components are available at different stations for the three cases: the steady flow with no control (baseline) and two cases with flow control accomplished by steady suction through a thin slot (0.004 c wide) situated at approximately 65% of the chord length, immediately upstream of the natural separation point, as well as by

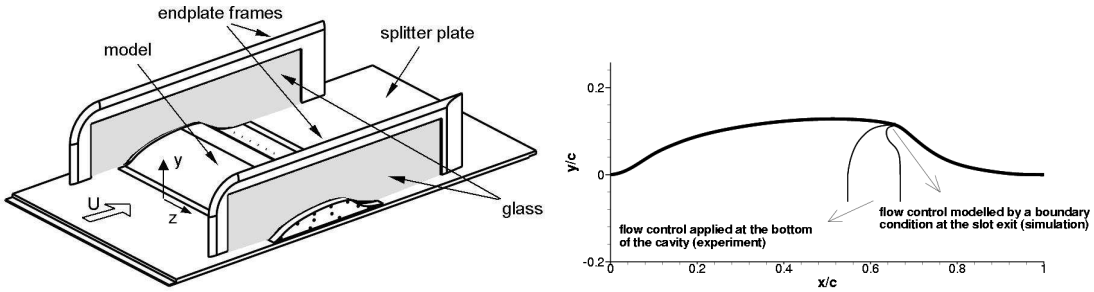

Figure 7.1: Schematic of the hump geometry, left - Greeblatt et al. [22]

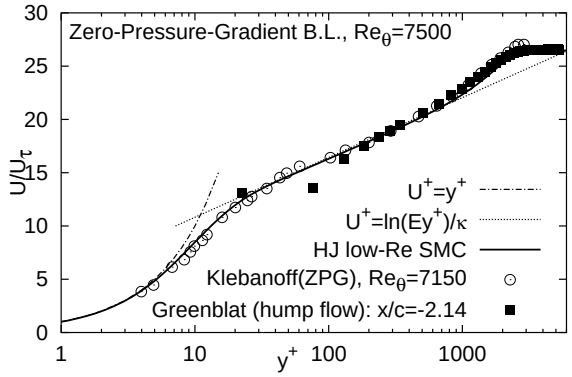

Figure 7.2: Mean streamwise velocity at location $x/c = -2.14$ corresponding to the zero-pressure gradient boundary layer at $Re_\theta = 7500$.

an alternating suction/blowing (zero net-mass-flow rate) of a jet into the boundary layer with nominal peak velocity of 26 m/s and frequency of 138.5 Hz. The oncoming flow is characterized by a zero-pressure-gradient turbulent boundary layer, whose thickness δ is approximately 57% of the maximum hump height ($h_{\max} = 53.74\ mm$) measured at the location about two chord lengths upstream of the hump leading edge (coinciding with the origin of the coordinate system, Fig. 7.1-right), corresponding to the momentum-thickness-based Reynolds number $Re_\theta \approx 7500$. The latter result was obtained applying a near-wall, second-moment closure model, Fig. 7.2. The experimentally measured pressure, reattachment location and spanwise pressure fluctuations reveal that both baseline and controlled flows are basically two-dimensional. Moreover, the selected hump model appears to be virtually insensitive to Reynolds number and inflow conditions. Due to these facts, the experimental data base of the hump flow represents an attractive separation control CFD-validation case. The baseline flow separates at $x/c \approx 0.665$ and reattaches at $x/c \approx 1.1$. As compared to the baseline case, application of steady suction accelerates the flow upstream of the slot and slightly delays separation ($x/c \approx 0.686$), increases the pressure downstream thereof, and shortens the recirculation bubble resulting in the reattachment at $x/c \approx 0.94$. Unlike the steady suction case, zero efflux control results in a relatively small effect on the pressure immediately upstream of the slot. The separation point is not significantly altered occurring at $x/c \approx 0.677$ but the pressure in the vicinity of separation reduces. Oscillatory control is not as effec-

tive as the steady suction, the reattachment being shifted upstream to the location $x/c \approx 1.1$.

Though demonstrated experimentally, unsteady flow separation, featured by the organized, large-scale coherent structures (characterized by both repeatable, but also non-regular unsteadiness of the oscillatory separated regions), remains a challenge for numerical simulation strategies. All three hump flow configurations including both separation control modes, i.e. steady suction and oscillatory blowing/suction, are considered in the present work. The major issue is a computational study of the effects of the boundary layer forcing on the mean flow and turbulence providing a comparative analysis of various methods for unsteady flow computations: Large-eddy Simulation (LES), Detached-eddy Simulation (DES), and Reynolds-Averaged Navier-Stokes method (RANS; both major model groups, Eddy-Viscosity models - EVM and Differential Second-Moment Closure models - SMC, are applied employing both approaches for near-wall treatment: standard wall functions and integration of the governing equations through the viscous sublayer and buffer layer) in such a complex flow situation.

7.2 Computational Method

Majority of the computations are performed with FASTEST 3D code, whereas FAN3D code is used initially to conduct some preliminary coarse LES which would give an insight into main features of a specific flow configuration. FASTEST 3D is parallelized applying the Message Passing Interface (MPI) technique for communication between the processors. Typically three and six processors are utilized when doing DES and LES, respectively. The sub-grid scales in the LES are modelled by the most widely used model formulation proposed by Smagorinsky with $C_s = 0.1$. A one-equation turbulence model by Spalart and Allmaras, based on the transport equation for turbulent viscosity, is employed to model the influence of the smallest, unresolved scales on the resolved ones within the DES computational scheme (e.g. Travin et al. [73]). The S-A turbulence model is also applied in the RANS mode. Various statistical turbulence models were examined by computing the baseline and steady-suction cases. They include the standard high-Reynolds number $k-\varepsilon$ model and its near-wall adaptation due to Launder and Sharma (LS $k-\varepsilon$; 1974 [39]) as well as the low-Reynolds number Reynolds-stress model developed by Hanjalić and Jakirlić (HJ RSM; 1998 [24]) employing the homogeneous part of the total viscous dissipation rate as a scale-supplying variable (Jakirlić and Hanjalić, [29]) and its high-Reynolds number asymptote due to Gibson and Launder (GL RSM; 1978 [21]). The length scale correction proposed by Hanjalić and Jakirlić [24] is introduced in the latter models to prevent the back-bending of the mean dividing streamline at the reattachment. The convective transport of all variables is discretized by a second-order, central differencing scheme (CDS) when performing LES, DES and RANS-EVM calculations. In the case of the Reynolds-stress model computations a blended 1st-order-upwind/2nd-order-central differencing scheme, implemented in a deferred-correction manner, is applied with the value of blending factor 0.7 corre-

sponding to the CDS scheme. Time discretization is accomplished by the (implicit) Crank-Nicolson scheme.

7.2.1 Solution Domain and Computational Grid

The solution domain (dimensions: $L_x \times L_y \times L_z = 6.14c \times 0.909c \times 0.152c$) is meshed with almost 4 Mio. ($426 \times 145 \times 64$) grid cells when applying LES. A grid used in the 2D RANS calculations (426×145) is extruded in the spanwise direction to create 3D grid configurations used for LES and DES. The solution domain employed for DES with a somewhat larger spanwise dimension ($L_z = 0.2c$) is meshed by approximately 1.7 Mio. ($426 \times 145 \times 28$) grid cells. As revealed at the two relevant workshops, the RANS computations have not shown remarkable difference in the solutions obtained if the computation domain was extended further upstream ($6.39c$) as in the experiment (e.g. Krishnan et al. [38]). Some additional simulations are conducted on purpose employing the coarser grid ($426 \times 145 \times 32$) grid cells within a domain of dimensions: $L_x \times L_y \times L_z = 6.14c \times 0.909c \times 0.152c$). Motivation, case specific details and important results of these runs will be presented as well.

7.2.2 Inflow conditions

It has been demonstrated experimentally that due to the selected hump geometry resulting separated flow is insensitive to the upstream boundary conditions and Reynolds number. Therefore, in all LES and DES computations available steady profiles (the mean experimental velocity profiles) were imposed at the inlet plane placed at $2.14c$ upstream of the hump leading edge. This is in accordance with the findings of the CFDVAL workshop on computational methods and turbulence model validation [58]. Moreover, You et al. [79] recently employed LES to predict the same flow configuration. These computations have actually followed the present study and reproduced to a large extent its main results. Particularly encouraging is agreement among the results, since the authors applied unsteady inlet boundary conditions.

The Reynolds-stress model computations require more elaborated profiles of all turbulence quantities including dissipation rate of the turbulent kinetic energy at the inlet cross-section (despite insensitivity to the inflow conditions, note that only the profiles of mean velocity and streamwise stress component are available from the reference experiment). For this purpose, the inflow data are generated by doing a separate computation of the zero-pressure gradient (ZPG) boundary layer with the same free-stream velocity $U_\infty = 34.6\ m/s$, using the same near-wall second-moment closure model (denoted by HJ low-Re SMC). The profiles obtained at the streamwise location corresponding to the boundary layer thickness $\delta = 30.5\ mm$ ($Re_\theta \approx 7,500$, Figs. 7.2 and 7.3), being in accordance with the experimental results at $x/c = -2.14$, are taken finally at the inlet plane of the solution domain for the RANS computations. The obtained results show good agreement with the available experimental data. In addition, the results of the boundary-layer measurements

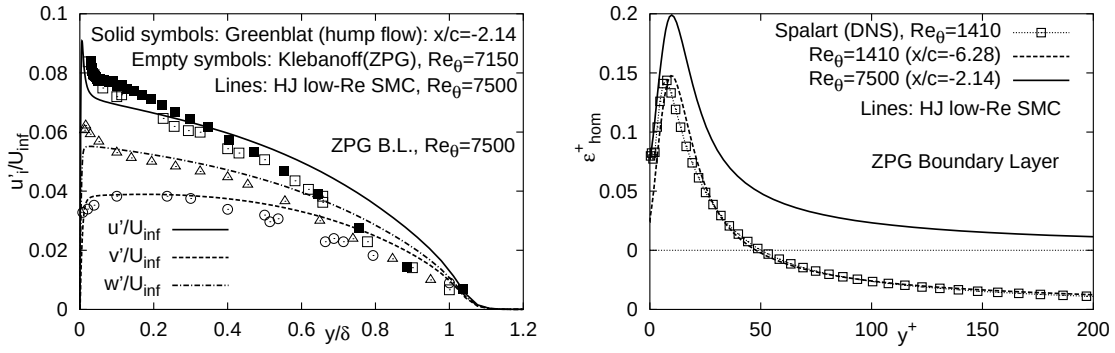

Figure 7.3: Reynolds stresses (left) and dissipation rate (right) at location $x/c = -2.14$ corresponding to the zero-pressure gradient boundary layer at $Re_\theta = 7500$. $\epsilon_{hom} = \epsilon - 0.5\mathcal{D}_k^\nu$

performed by Klebanoff [37] at the location corresponding to $Re_\theta = 7,150$ are also displayed, confirming the ZPG boundary-layer structure of the flow at this location. Fig. 7.3 (right) shows the profile of the homogeneous dissipation rate which differs from the total viscous dissipation rate only in the immediate wall vicinity (up to $y^+ \approx 20$) for one half of the molecular diffusion of the kinetic energy of turbulence: $\epsilon_{\text{hom}} = \epsilon - 0.5\mathcal{D}_k^\nu$. In order to quantify this computational result at such a high Reynolds number $Re_\theta \approx 7,500$ (solid line in Fig. 7.3-right), for which no reference data (neither experimental nor from a DNS) exist, the profile obtained at an upstream location $x/c = -6.28$ corresponding to $Re_\theta = 1,410$ is compared with the Direct Numerical Simulation (DNS) of Spalart [69], exhibiting very good agreement. The latter comparison is important with respect to the credibility of the dissipation rate prediction. It should be noted that the energy dissipation rate obtained by this near-wall SMC model is also used for the resolution assessment (cf. Fig. 7.8).

7.2.3 Boundary Conditions and Time Step

A further important outcome of the CFDVAL workshop was that the modeling of the flow within the cavity/nozzle (Fig. 7.1) was not found to be critical for the flow predictions, as far as the baseline and steady suction flow control cases are concerned. Although there is no forced flow within/through the cavity in the baseline case, the experiment was performed using the opened slot. Accordingly, a low-speed flow through the cavity opening could be generated due to the pressure difference. However, the S-A RANS computations of the baseline and suction cases show that modeling of the cavity opening does not result in noticeable differences (cf. Fig. 7.4. Consequently, different flow configurations are computed by imposing the appropriate boundary conditions directly at the control slot. Steady suction is achieved by adopting the spatially uniform suction velocity at the slot corresponding to the mass flow rate of 0.01518 kg/s. Oscillatory suction/blowing is simulated by imposing a sinusoidal zero net-mass-flow jet at the slot with the frequency of 138.5 Hz. Different velocity amplitudes are examined. If the measured peak slot velocity of 26.6 m/s is taken, the resulting mass flow rate becomes twice as high as the experimental

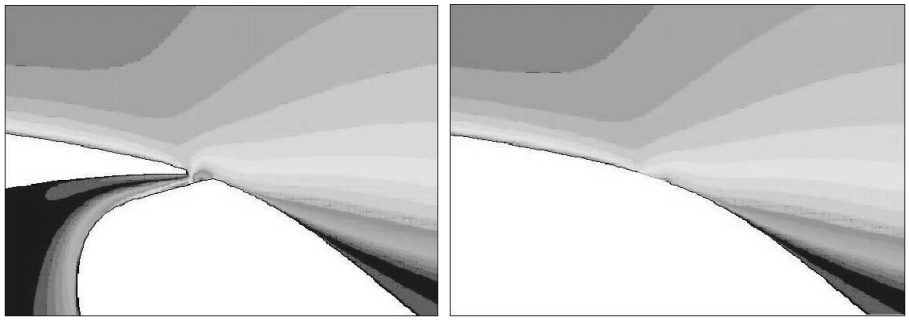

Figure 7.4: Contours of the mean streamwise velocity for the suction case obtained by the S-A RANS model without taking into account the cavity (left), with the cavity included in the computational domain (right)

one. Hence, a more realistic boundary condition is to impose the slot velocity corresponding to the experimental mass flow rate. Interestingly, boundary conditions in the oscillatory case are not influential as far as the gross flow characteristics like locations of flow separation and reattachment are concerned. However, the latter boundary condition turns out to be more adequate, yielding superior predictions of the flow velocity and turbulence field. Influence of the modeling of the control slot on the flow predictions in the oscillatory case will be addressed later in discussion of the results. No-slip boundary conditions are applied at both walls resolving the wall boundary layer fairly well when performing LES and DES. The dimensionless wall distance ${y_1}^+$ of the wall-closest computational nodes were ${y_1}^+ < 1$ for the lower wall and ${y_1}^+ = 1.0 - 1.75$ for the upper wall. The values of ${y_1}^+$ of the wall-nearest grid point were between 0.5 for the low-Re number, RANS calculations and 15 for the high-Re number RANS calculations. In the case of the high-Re number RANS computations, the standard wall functions are utilized. In the LES and DES computations, the convective outflow conditions are applied at the outlet and periodic boundary conditions along the spanwise direction. The dimensionless time steps of 0.005 and 0.003 (based on the hump chord length and free stream velocity) are used in the DES and LES, respectively, providing a CFL number less than unity throughout the largest portion of the solution domain. The only exception is the narrow region around the thin slot at the hump (1.7 mm wide) in the oscillatory blowing/suction case, where a high velocity jet is introduced into the separated shear layer. The CFL number reaches its maximum value being around 15 in a very few cells in this region which is characterized by a strongly refined grid. Additionally, some preliminary simulations of the oscillatory blowing/suction case employing finer time steps (0.0016 and 0.003) reveal that the results are not significantly affected by the time step refinement. Fig. 7.5 compares the results obtained by both LES and DES employing the standard time step size (0.005) and three times finer time step. The computed case is the oscillatory flow control which is expected to be more demanding regarding the time resolution. Moreover, the slot velocity is assumed to be equal to the experimentally measured peak value of 26 m/s, thus yielding approximately twice as high mass flow rate peaks compared to the experimental ones. Evidently, time step refinement affects, but interestingly does not improve

the streamwise velocity profiles, only in the region downstream of the reattachment. Hence, the time step adopted in majority of LES and DES appears to be an optimum compromise with respect to the time resolution and required CPU time.

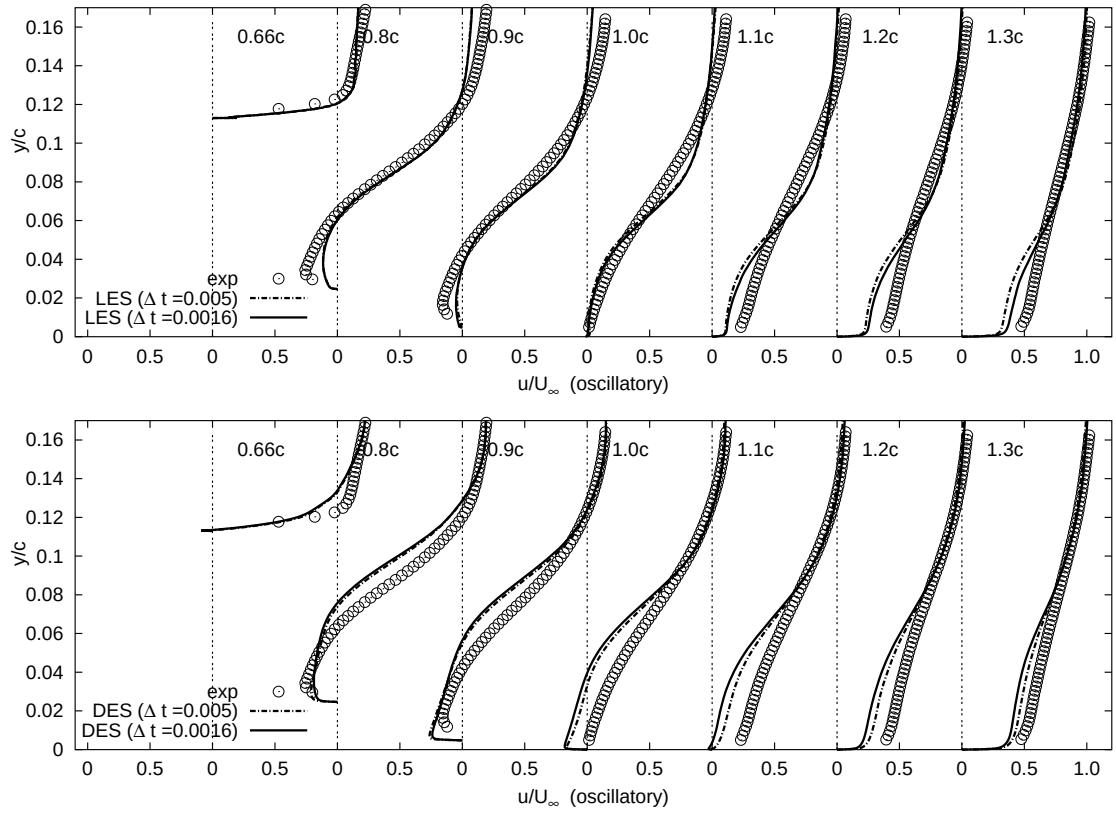

Figure 7.5: Influence of the time resolution on the mean streamwise velocity; LES (upper) and DES (lower) of the oscillatory control case (note that the slot boundary condition yields approximately twice as high mass flow rate peaks compared to the experimental ones).

7.2.4 Grid Density Study

The flow region of interest just downstream of the slot including the region around the reattachment was meshed to provide $(\Delta x^+)_{max} = 80$, $\Delta y^+ = 1 - 80$, $(\Delta z^+)_{max} = 150$ (DES grid), and $(\Delta x^+)_{max} = 100$, $\Delta y^+ = 1 - 100$, $(\Delta z^+)_{max} = 60$ (LES grid). The grid resolution (in wall units) along the bottom wall is displayed in Figs. 7.6 and 7.7. Compared to DES, the LES resolution is significantly finer with $(\Delta z^+)_{max} = 60$ because of the finer grid ($N_{z,LES} = 64$ vs. $N_{z,DES} = 32$) and a somewhat smaller spanwise domain size ($L_{z,LES} = 0.152c$ vs. $L_{z,DES} = 0.2c$). Admittedly, the resolution adopted is coarser than it would be required for resolving the near-wall streaky structures, which demands a spacing of order $\Delta y^+ = O(1)$, $\Delta x^+ = O(50)$ and $\Delta z^+ = O(20)$ [25]. The reason for the slightly extended spanwise dimension $L_{z,DES} = 0.2c$ is shifting of the LES–RANS interface away from the wall in order to provide its optimal position for the given grid size, i.e. to avoid that the

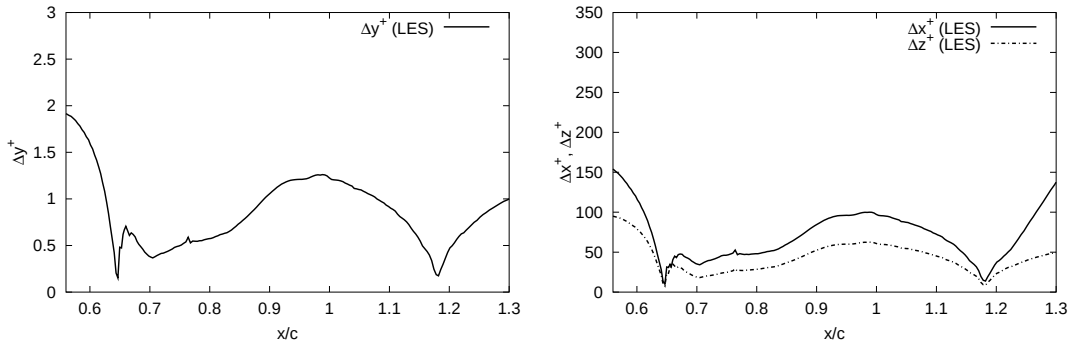

Figure 7.6: Grid resolution in terms of the wall units; LES of the baseline flow.

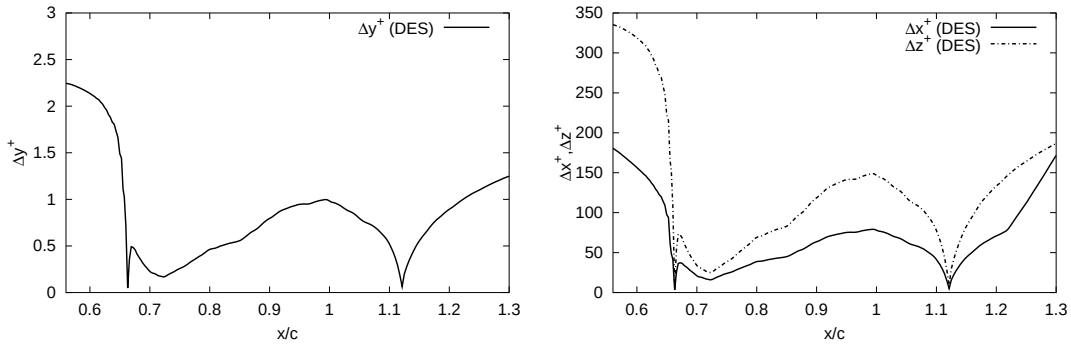

Figure 7.7: Grid resolution in terms of the wall units; DES of the baseline flow.

interface penetrates too deeply into the boundary layer. If the LES region would reside too close to the wall due to insufficient resolution (one would have actually a resolution typical for RANS in the LES region), lower viscosity and turbulence levels could be obtained, possibly causing a premature separation and poorer flow predictions. It is recalled that the interface position corresponds to the DES-filter ($C_{DES} \max(\Delta x, \Delta y, \Delta z)$); $C_{DES} = 0.65$.

The ratio of the grid length scale to the Kolmogorov length scale (Δ/η_k; $\eta_k = (\nu^3/\epsilon)^{1/4}$), representing to a certain extent the position of the cut-off in the frequency spectra, is displayed in Fig. 7.8. Three positions along the gridlines in the streamwise direction are considered, two of which reside in the near-wall region (j=20, 40), whereas location j=60 corresponds to the separated shear layer (Fig. 7.8). The Kolmogorov length scale is estimated from the dissipation rate obtained from the RANS computation of the baseline case employing the Reynolds stress model formulation of Hanjalić and Jakirlić (1998). In absence of the turbulence-energy budget, the dissipation rate obtained from the second-moment closure can provide an insight into the grid resolution (see Fig. 7.3 (right) to check capability of the HJ RSM model to capture dissipation profile correctly). Based on this assessment it appears that the near-wall region has a sufficient resolution for LES (ideally, a value of $\Delta/\eta_k \leq 10 - 12$ would provide the spectral cut-off being fairly close to the high-frequency wave-number range, corresponding to the dissipative part of the spectra [19, 14]), while the grid resolution in regions away from the walls, including

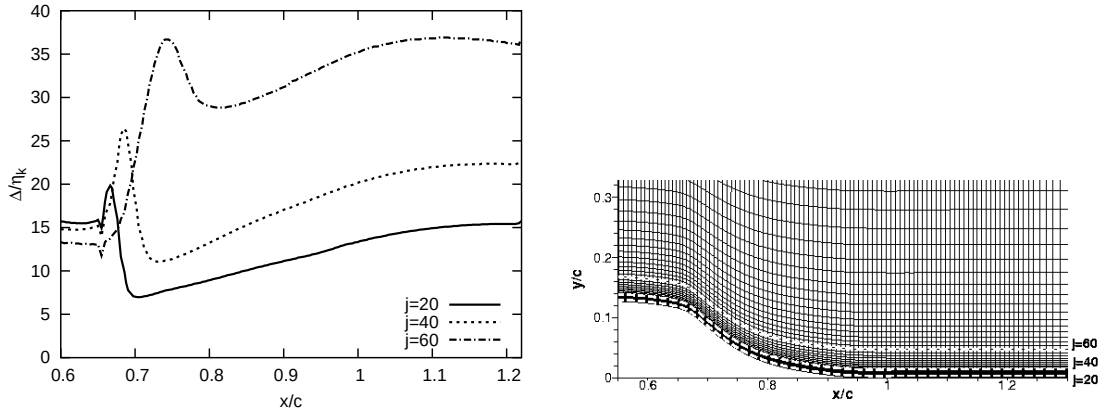

Figure 7.8: Ratio of the grid scale to the Kolmogorov length scale and locations of the grid resolution assessment.

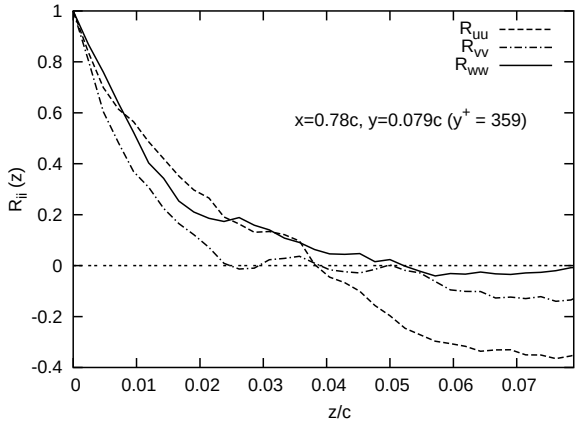

Figure 7.9: Spanwise autocorrelation functions R_{uu}, R_{vv} and R_{ww} obtained by LES (baseline case) along a spanwise line within the separated shear layer at $y/c = 0.079$ ($y^+ = 359$) at the streamwise location $x/c = 0.78$ corresponding to the middle of the separation bubble.

the separated shear layer, seems to be coarser. However, the employed resolution still provides modelled turbulent kinetic energy (estimated as $k_{sgs} = \Delta^2|S|^2/0.3$, according to Mason and Callen, 1986) which does not exceed 5% to 9% of the resolved one and the ratio of the instantaneous SGS viscosity to the molecular one remains typically between 5 to 13 (maximum values apply within the region around the hump).

The spanwise autocorrelation functions R_{uu}, R_{vv} and R_{ww} obtained by LES along a spanwise line within the separated shear layer at $y/c = 0.079$, i.e. $y^+ = 359$, at the streamwise location $x/c = 0.78$ (corresponding to the middle of the separation bubble) are plotted in Fig. 7.9 in order to check the adequacy of the spanwise size of the solution domain. The spanwise extent of the vortical structures corresponds approximately to double the value of the correlation length representing the distance between the origin and the separation where the correlations drop off to zero. Apart from the correlation of the v fluctuations, the correlations remain at $15-35\%$ at the

largest separation ($z/c = 0.075$). Such an increased correlation length is typically a consequence of the spanwise rollers in the shear layer. This analysis provides a clear indication that the correlations do not vanish within the half of domain size in the spanwise direction. Therefore, the adopted spanwise dimension is not entirely sufficient to ensure spanwise decorrelation. The spanwise extent adopted in the detached-eddy simulation is somewhat larger ($L_{z,DES} = 0.2c$). Looking at the flow structures presented in Chapter 5 (Fig. 5.15), it could be regarded as sufficient. It should be furthermore recalled that the main objective of the work is comparative analysis of the most widely used method for unsteady flow calculations, such as LES and DES, and they both are carried out under comparable conditions. At this point, it should be noted that Krishnan et al. [38] have used a substantially smaller spanwise dimension ($L_z = 0.121c$) to perform DES of the hump baseline flow.

7.3 Results and Discussion

Flow statistics are taken over 5 to 7 flow-through times and the time-averaged results are extracted to provide comparison with the available experimental data. The results comprise the wall pressure distribution, skin-friction coefficient, time-averaged streamlines, corresponding profiles of mean velocity field and turbulence quantities at the characteristic locations within the separation zone and post-reattachment region, as well as the instantaneous flow field: velocity field, pressure fluctuations, spanwise and streamwise vorticity. Finally, some phase-averaged results extracted from the LES of oscillatory control case will be compared to the experiment.

The separation and reattachment locations for the computed configurations are summarized in Table 7.1 and Fig. 7.10. The effect of the flow control on the recirculation zone shortening can be clearly recognized. Both the LES and DES (except

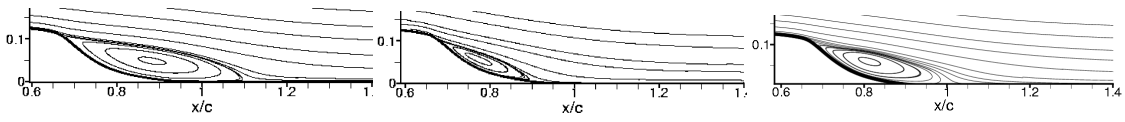

Figure 7.10: Time-averaged streamlines obtained by LES method; baseline (left), steady suction (middle) and oscillatory flow control (right) case.

the steady suction case) results are in a very close agreement with the reference experiment with respect to both separation and reattachment locations. The experimental observation, that the steady suction represents the most effective flow control mode, that is the case with the minimum reattachment length, is confirmed by both computational methods. These results will be discussed in more details in the following sections. The predictions of the separated flow over a wall-mounted hump for the configurations without flow control (baseline) and steady suction flow

Table 7.1: Separation and reattachment locations

		$(x/c)_S$	$(x/c)_R$
Baseline	Exp.	0.673	1.110
	LES	0.667	1.114
	DES	0.663	1.121
	S-A	0.667	1.259
	Std. $k-\epsilon$	0.672	1.125
	LS $k-\epsilon$	0.670	1.125
	GL RSM	0.670	1.158
	HJ RSM	0.660	1.195
Suction	Exp.	0.686	0.940
	LES	0.671	0.947
	DES	0.674	1.105
	S-A	0.674	1.098
	Std. $k-\epsilon$	0.684	1.005
	LS $k-\epsilon$	0.683	0.988
	GL RSM	0.680	1.032
	HJ RSM	0.670	1.073
Oscillatory	Exp.	≈ 0.677	≈ 1.0
	LES	0.671	1.050
	DES	0.662	1.110

control will be discussed first. Afterwards, LES and DES of the case with oscillatory (sinusoidal) suction/blowing flow control will be presented, including both the time-mean and phase-averaged flow fields.

7.3.1 Baseline Configuration

Prior to discussion of the results, a due attention has to be payed when designing the numerical grid. Each of the flow configurations is initially computed (FAN-3D employing the LES method) on the coarser grid ($426 \times 145 \times 32$, domain: $L_x \times L_y \times L_z = 6.14c \times 0.909c \times 0.152c$) so as to provide certain guidelines for the subsequent simulations. In particular, the grid design for DES is known to be the most critical point. As already mentioned, if not properly selected, the position of the LES–RANS interface that is dictated by the grid may cause serious deterioration of the flow predictions. To shed some light on this issue and demonstrate DES sensitivity to the interface position, DES and LES are performed on exactly the same grids. First, LES of the baseline flow is conducted on the grid $426 \times 145 \times 32$, the mean streamwise velocity profiles being shown in Fig. 7.11-upper. Despite the coarse spanwise resolution ($(\Delta z^+)_{max} \approx 120$), a credible representation of the mean flow is obtained except in the region of flow separation. The DES performed on the same grid yields extremely poor predictions downstream of the separation. On the other side, the same flow is recomputed but now employing the coarser grid ($426 \times 145 \times 28$)

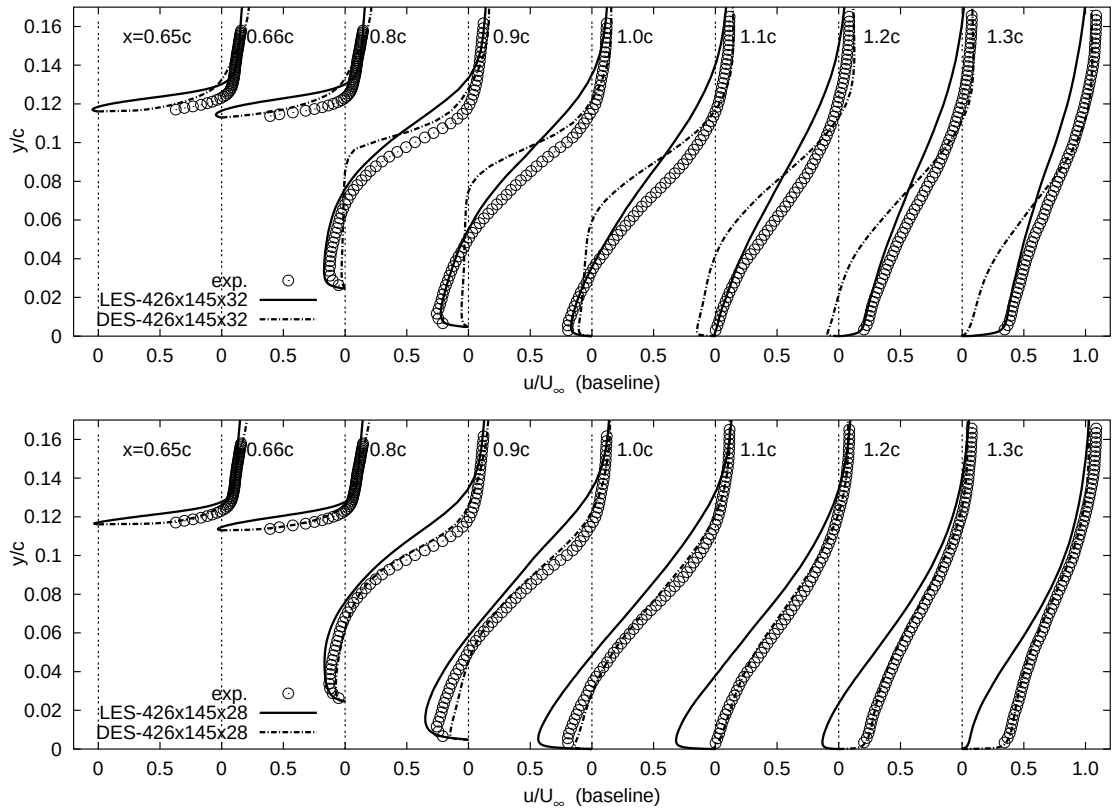

Figure 7.11: DES vs. LES on the same coarse grid; superiority of DES over LES (coarser spanwise resolution)-upper, poor performance of DES compared to LES (finer spanwise resolution)-lower.

and larger spanwise computational domain ($L_x \times L_y \times L_z = 6.14c \times 0.909c \times 0.2c$).

LES performs poor due to the coarser resolution as much expected. However, the DES results improve strikingly despite substantially coarser spanwise resolution. This can be attributed to the position of the LES–RANS interface whose distribution is depicted in Fig. 7.12. By grid refinement in the spanwise direction, the interface is shifted too close to the wall, penetrating deeply into the oncoming boundary layer. The resolution in this region is not sufficient to support LES, resulting in extremely low turbulence levels (see shear stress profiles in Fig. 7.13). The separation point is captured, quite fortuitously, but due to the underpredicted turbulence, poor predictions downstream of the separation occur. Underpredicted turbulent shear stress implies insufficient mixing (note an excessive shear strain at $x/c = 0.9$ in Fig. 7.11-upper) in the separated shear layer which reattaches far too late. Hence, a detrimental effect of the LES–RANS interface position is evident. Refinement of the LES grid by doubling the spanwise resolution ($426 \times 145 \times 64$) leads to a significant improvement of the results as demonstrated by mean streamwise velocity profiles shown in Fig. 7.14. Note that henceforth, unless otherwise specified, LES and DES refer to the computations employing the grids and domain sizes specified in sec. 7.2.1.

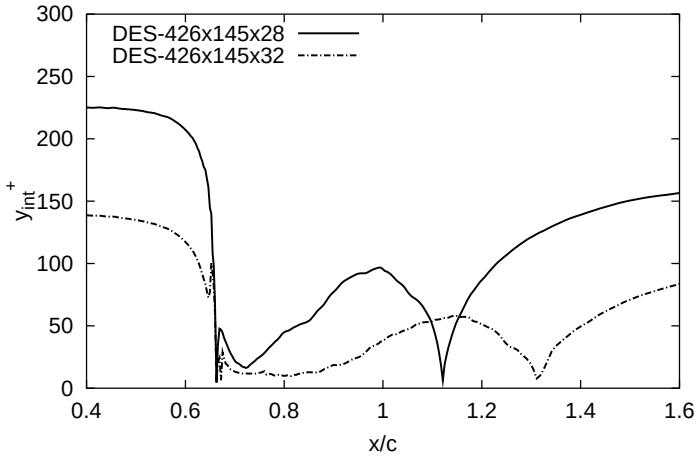

Figure 7.12: Position of the LES–RANS interface dictated by the grid; DES of the baseline flow employing different computational grid and domain size.

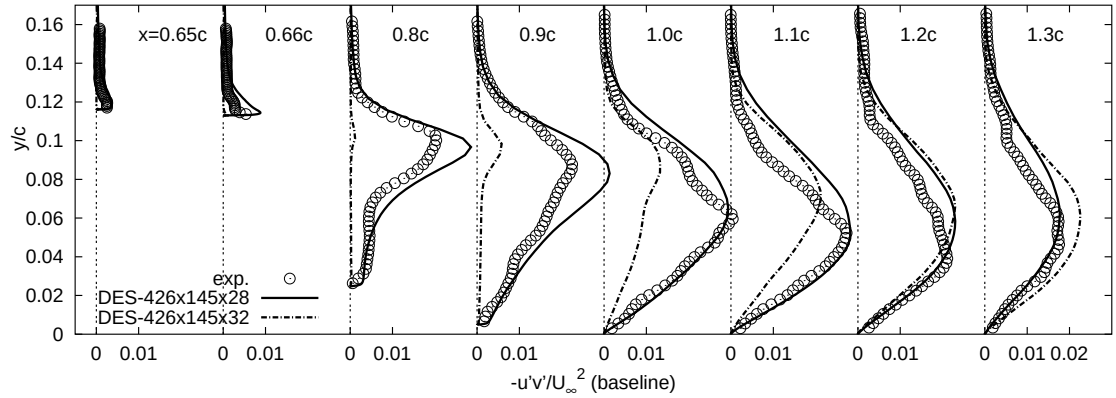

Figure 7.13: Shear stress profiles obtained by DES employing different computational grid and domain size.

Predictions of the pressure coefficient for the baseline case are shown in Fig. 7.15. The LES and DES results agree better with the measurements than the ones obtained by the 2D S-A RANS. However, the peak suction pressure is underpredicted with all methods (cf. Fig. 7.15-left). This can be explained by blockage effects from the wind tunnel side walls, not accounted for in the computations. Indeed, the additional baseline experiment performed without side plates has corroborated the existence of the wall-blockage effect. It is noteworthy to emphasize an excellent agreement of the pressure coefficient obtained by DES with this experiment in Fig. 7.15-right. It is believed that the fact that blockage effects are not accounted for in the simulations does not invalidate a study of the flow configurations subjected to flow control.

Predictive capability of various RANS closures with respect to the baseline flow configuration was already evaluated in section 5.2. Herein, the S-A RANS model will be included in comparison with the experimental data along with the results obtained by DES and LES. All RANS models overpredict the reattachment

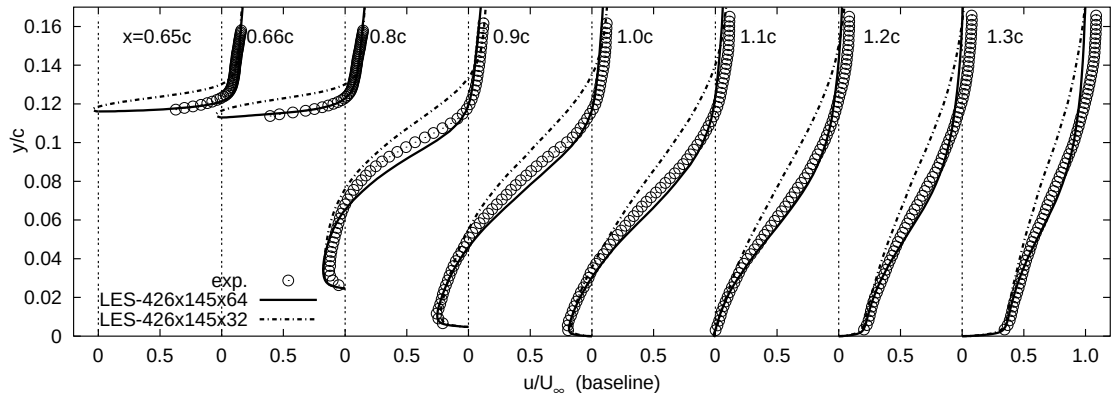

Figure 7.14: Mean velocity profiles obtained by LES with the spanwise grid refinement

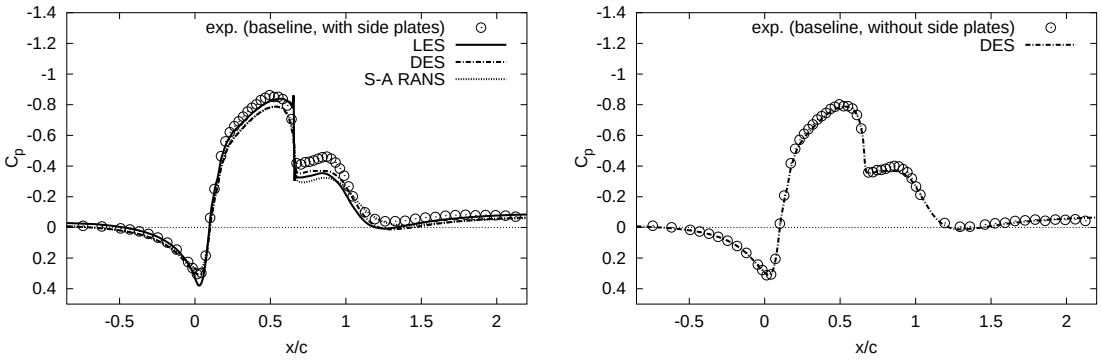

Figure 7.15: Pressure coefficient for the baseline configuration with (left) and without (right) side plates in the experiment.

length despite partially correct capturing of the separation location (see Table 7.1 for the quantitative comparison). The mean streamwise and wall-normal velocity profiles are compared in Fig. 7.16. The LES and DES results agree closely with the experimental data. It is interesting to see that DES predictions are even better than the ones obtained by the conventional LES especially in the region of the velocity profile inflection, that is the region with zero value of its second derivative (see also the shear stress profiles in Fig. 7.17). The reason for such an outcome could be justified by a more suitable modeling of the oncoming wall boundary layer (near-wall Spalart-Allmaras model in the DES framework vs. mixing-length-hypothesis-based Smagorinsky model), the fact coming especially into focus under conditions of a lower grid resolution. It should be noted here that the channel (height = $0.909c \approx 381.78mm$) constriction due to hump ($h_{max} = 53.74$) is not too strong (only about 14%), causing the separation point as well as the separated-shear-layer structure (and consequently the size and shape of the separation zone itself) largely depend on the oncoming wall boundary-layer prediction. Furthemore, the available measurement of the mean skin-friction coefficient for the baseline case reveal the superiority of DES in the post-reattachment region. As shown in Fig. 7.18, flow recovery is accurately reproduced by DES illustrating the main advantage of this

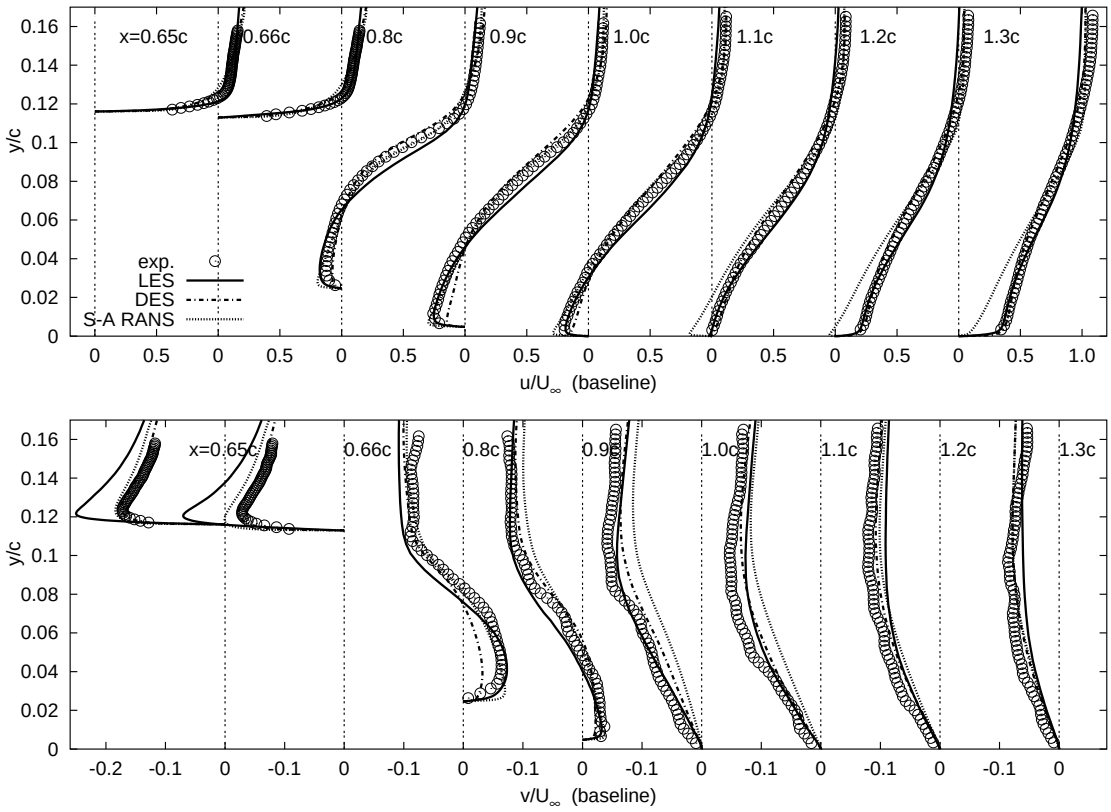

Figure 7.16: Mean streamwise (upper) and wall-normal (lower) velocities obtained by LES, DES and S-A RANS (baseline case)

hybrid method. Feasibility and advantage of the DES as a hybrid LES–RANS approach is further expressed by the fact that these results are obtained using a coarser grid (1.7 Mio. in total vs. 4 Mio. for LES).

The Reynolds shear stress evolution presented in Fig. 7.17 demonstrates how crucial it is to capture the correct level of turbulence in the separated shear layer with respect to the mean flow features downstream, especially to the reattachment location. The correct LES and DES predictions of the shear stress in the region aligned with the mean dividing streamline lead eventually to the correct predictions of the reattachment length. By careful inspection of the shear stress profiles obtained by LES, one can see the influence of grid resolution in different regions of the flow. As a consequence of the under-resolved boundary layer upstream of the separation location, LES typically returns too a high level of shear stress (locations $x/c = 0.65$ and 0.66). Likewise, due to a coarser resolution, underprediction of the shear stresses is observed downstream at $x/c > 1.0$: in the shear layer (at $x/c = 1.0$, $y/c \approx 0.08$) and in a new shear layer (where a strong interaction between the new wall boundary layer being generated in the post-reattachment region and the bulk flow occurs; cross-sections at $x/c = 1.1, 1.2$ and 1.3). The coarser grid in this region causes high dissipation and consequently lower turbulence level. Nevertheless, it is to be noted that close agreement with the measured shear stresses, and particularly wall-

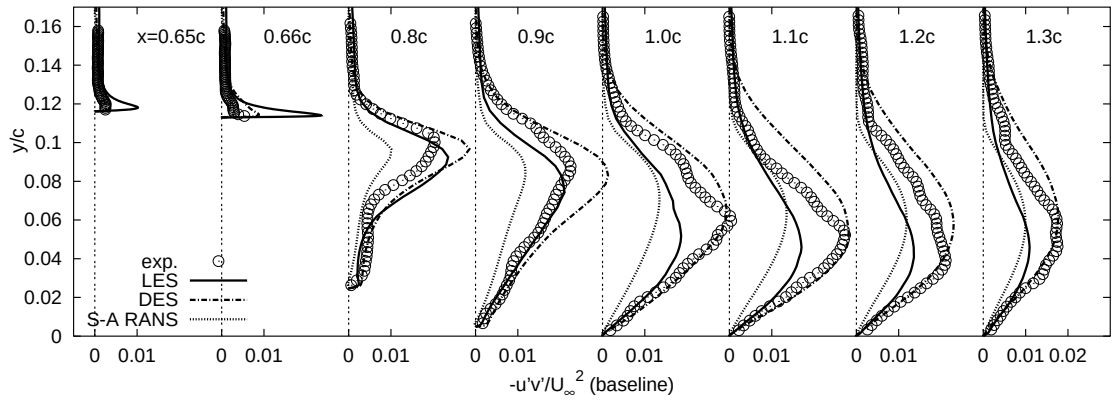

Figure 7.17: Shear stress profiles obtained by LES, DES and S-A RANS (baseline case)

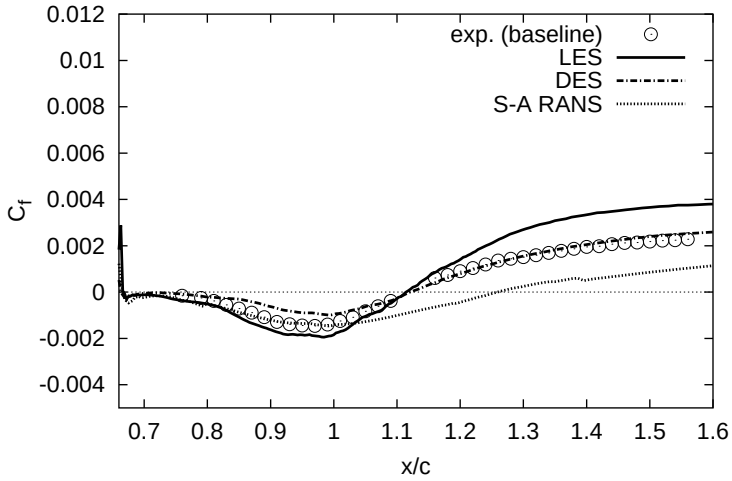

Figure 7.18: Mean skin-friction coefficient obtained by LES, DES and S-A RANS (baseline case)

normal stresses (see Fig. 7.19-lower), near the wall complies with the supposition of a sufficiently fine grid in this region. Conversely to LES, DES yields correct levels of the shear stress upstream of the separation point and consequently downstream at $x/c > 1.0$. Certain overpredictions at the locations $x/c = 0.8$ and 0.9 are likely associated with the grid resolution. In this region, the DES suffers from insufficient streamwise resolution as indicated by remarkable overpredictions of the streamwise stresses (7.19-upper), but one should recall that the maximum uncertainty in the measured stresses is estimated to be 20%.

7.3.2 Steady Suction Flow Control

Compared to the baseline case, regardless of modeling level, the RANS predictions of the steady suction case appear to be even less accurate. The representative results are displayed in Fig. 7.20. As found in the experiments, the flow subjected to the steady suction control experiences a significant acceleration at the ramp ($x/c = 0.65$ and 0.66). By careful inspection of the velocity profiles at these

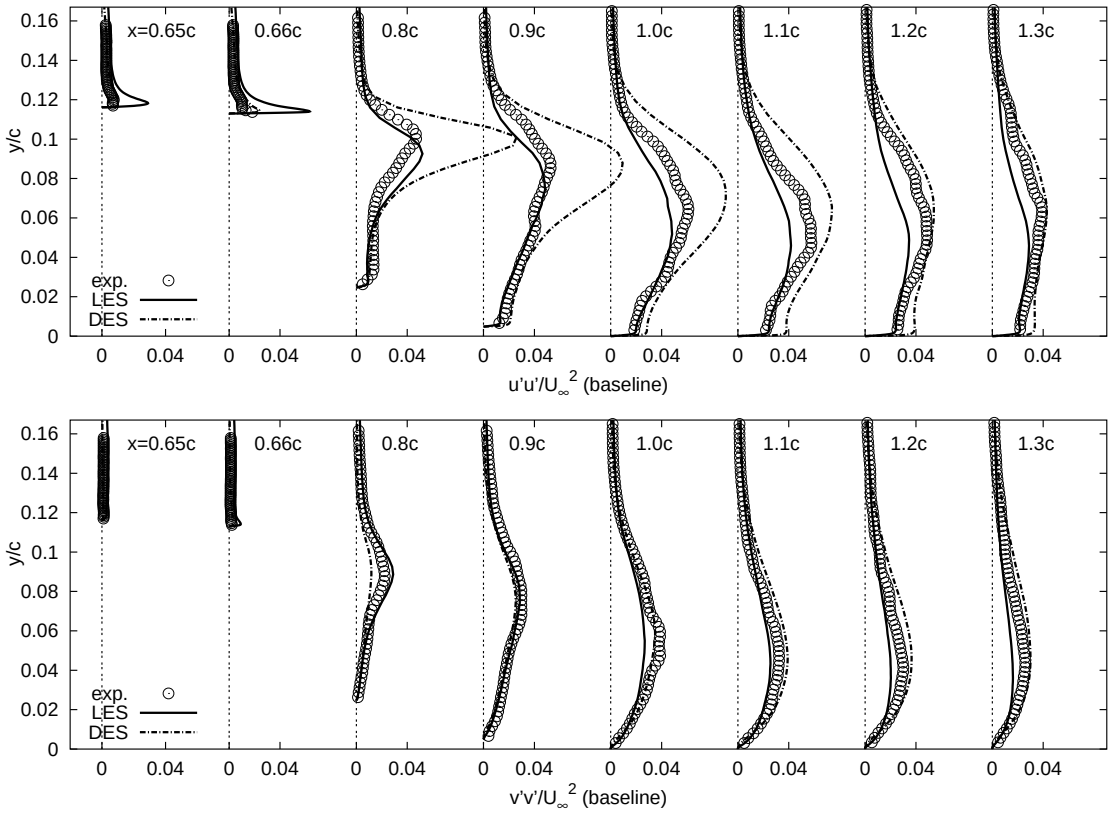

Figure 7.19: Streamwise (upper) and wall-normal stress profiles obtained by LES and DES (baseline case)

location, one can see that RANS does not fully reproduce this feature of the flow. The streamwise velocity remains consequently underpredicted within the separation bubble and further downstream of the reattachment. The enhanced turbulence production in the separated shear layer can not be captured by the RANS models as documented by consistently too a low level of the shear stress (cf. Fig. 7.20-lower). Inspite of that, the main response of the flow to the suction flow control, i.e. a reduction of the reattachment length, is qualitatively reproduced as can be seen in Table 7.1.

The pressure coefficient distributions for the steady suction flow control case are presented in Fig. 7.21. Underprediction of the peak suction pressure is present in the suction case as well. Contrary to the baseline case, advantages of the DES over the S-A RANS predictions are not observed in the pressure distributions, noting that both the RANS models and DES fail to capture the correct reattachment location (Table 7.1). On the other hand, LES shows in general very close agreement with the experimental data despite using the same grid as for the baseline case, which was regarded as not sufficiently fine. Such a behavior can be explained by the fact, that the suction applied at the natural (baseline) separation point reduces to a certain extent the necessity for a highly resolved wall boundary layer approaching the hump. For instance, by activating the flow suction through a narrow opening

at the hump crest, the intermittency of the separation region is damped to a large extent leading to an almost fixed separation point. A slight overprediction of the pressure coefficient along separation and recovery regions may be attributed to the blockage effects.

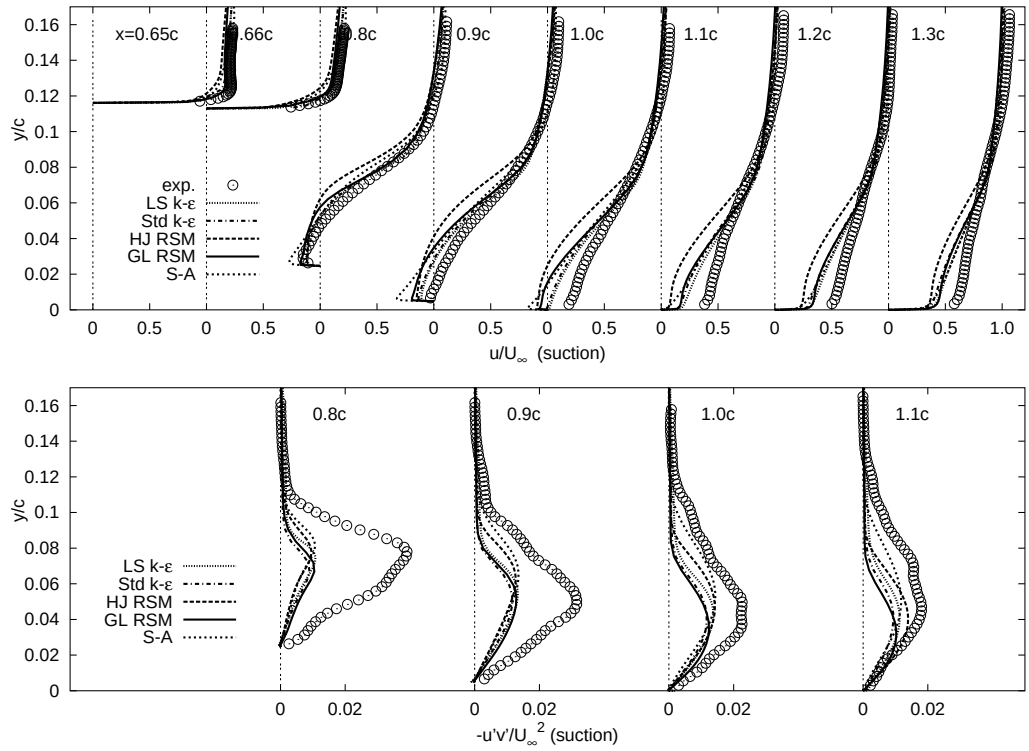

Figure 7.20: Mean streamwise velocity (upper) and shear stress (lower) profiles obtained by various RANS closures (suction case)

Mean velocity profiles shown in Fig. 7.22 support the previous observation expressed regarding the pressure distribution. The deviations from the experimental results with respect to the backflow intensity within the recirculation bubble are clearly visible, influencing strongly the flow around reattachment and in the recovery region downstream (it applies to the S-A RANS and DES). LES predictions of the mean velocity are in very good agreement with the experiment in spite of the slightly underpredicted separation location. Reynolds shear stress profiles are presented in Fig. 7.23-upper. The intensification of the mean straining due to local flow forcing in the suction case results in an enhanced turbulence level, representing the basic mechanisms of active flow control. Compared to the S-A RANS and DES, LES captured the increased turbulence level in the separated shear layer region very well. Moreover, profiles of streamwise and wall-normal stresses (Fig. 7.23-middle and lower) confirm credibility of LES predictions, both qualitatively and quantitatively. An excessive gradient of the streamwise velocity returned by DES (see Fig. 7.22-upper) results in insufficient turbulent mixing in the separated shear layer. This is clearly visible from remarkable overpredictions of the wall-normal velocity (Fig. 7.22-lower) and particularly low level of the corresponding stress

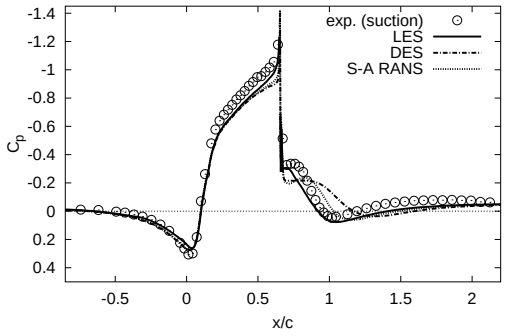

Figure 7.21: Pressure coefficient for the steady suction case.

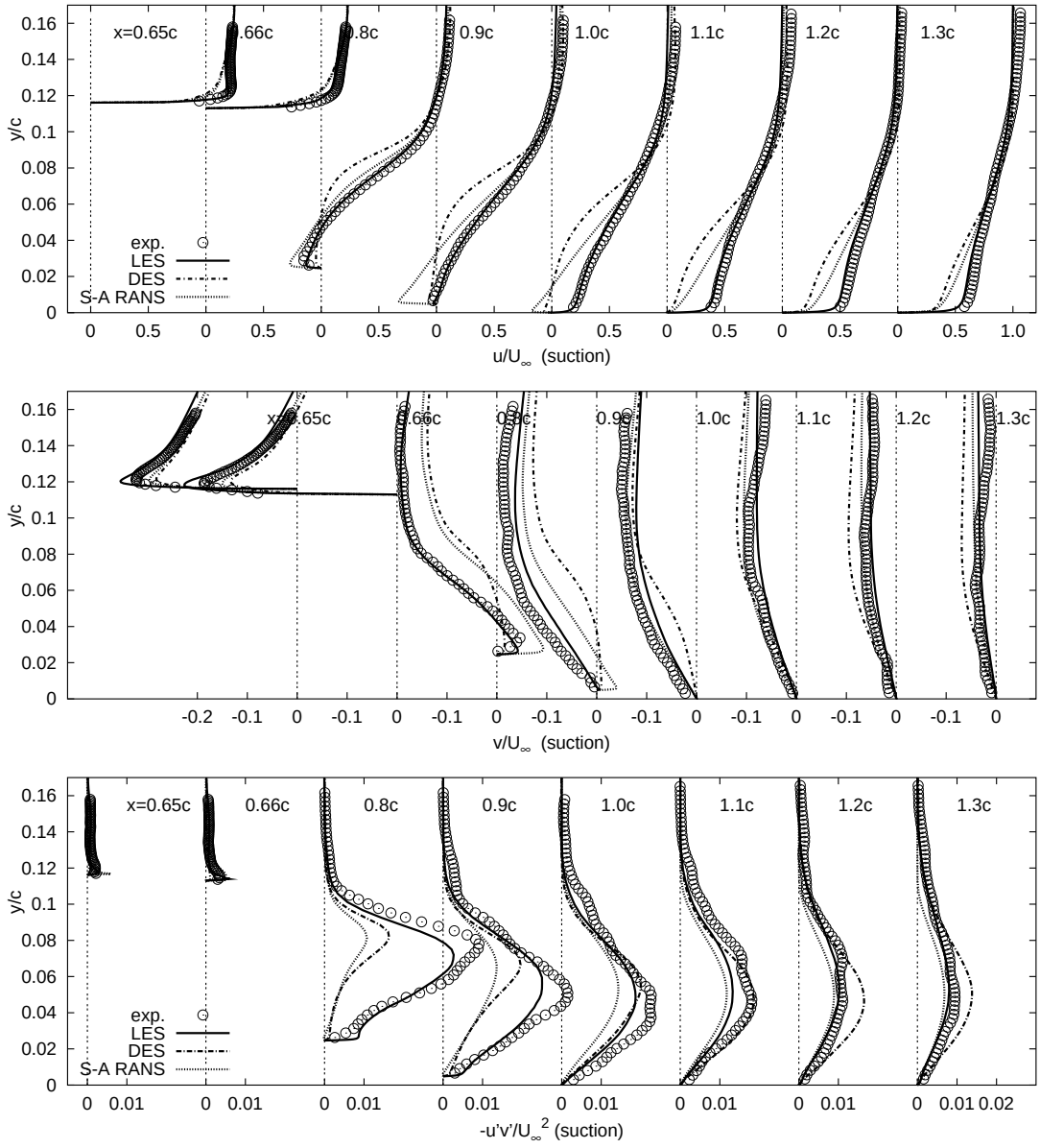

Figure 7.22: Mean streamwise (upper) and wall-normal (middle) velocities, shear stress (lower) obtained by LES, DES and S-A RANS (suction case)

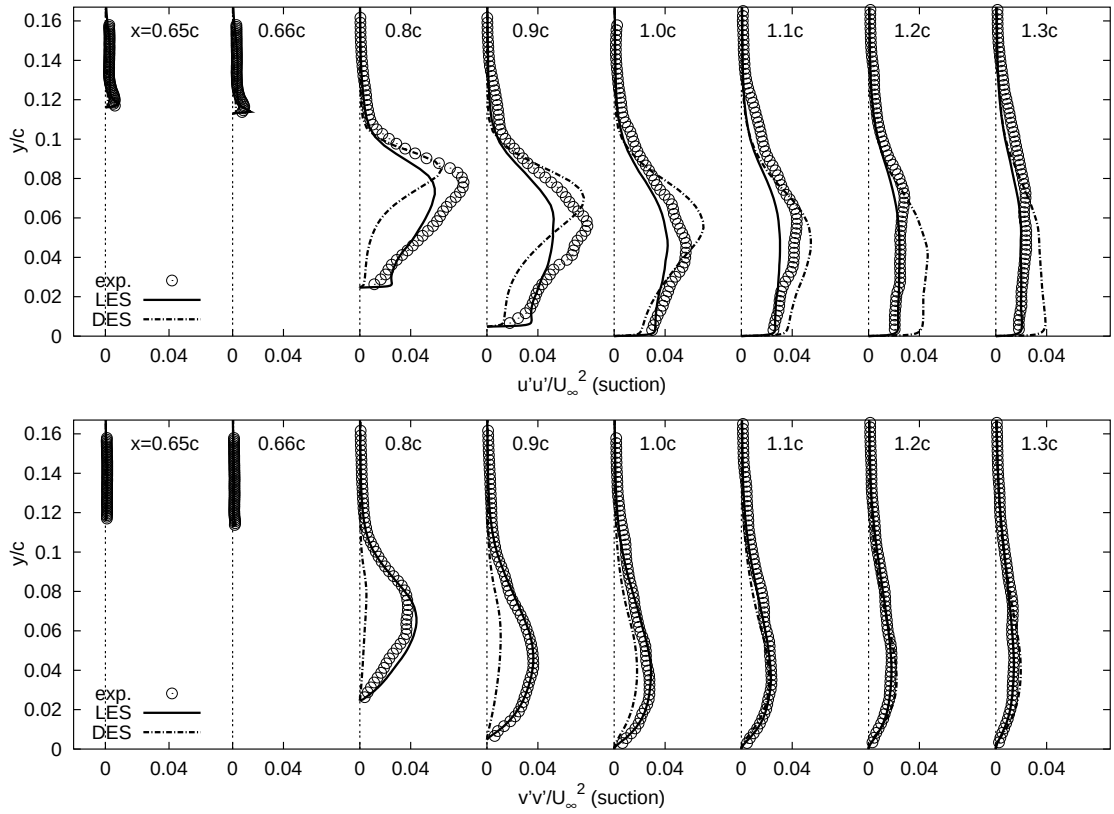

Figure 7.23: Streamwise (upper) and wall-normal stress (lower) profiles obtained by LES and DES (suction case)

component $\overline{v'v'}$. The results presented so far imply that, in order to reproduce main characteristics of the hump flow, it is extremely important to capture the correct level of wall-normal stress just upon the separation location. Qualitatively different performance of DES compared to LES in two different flow configurations employing the same grid (DES performs very well in the baseline case, but poor in the suction case) indicates the importance of the grid design within the DES framework. Interestingly, Krishnan et. al (2004) have also reported the poor DES predictions of the suction case compared to the baseline configuration. Nevertheless, DES is capable of predicting basic response of the flow subjected to the steady suction. To strenghten this assertion, some additional experiments performed using different suction rates are considered. Steady suction, as a means to control the hump flow, has been proven to alter the pressure distribution without affecting the mean flow reattachment. Fig. 7.24-left shows that, if the suction rate is increased by approximately 80% percent, the pressure upstream of the separation increases whereas decrease in the pressure is observed downstream. DES of the hump flow with a comparably increased suction rate clearly captures this effect of the suction mass flow rate on the mean pressure coefficient C_p (Fig. 7.24-right).

The issue of the LES–RANS interface, whose position is dictated by the grid adopted (independent of the flow structure), appears to be crucial for exploiting

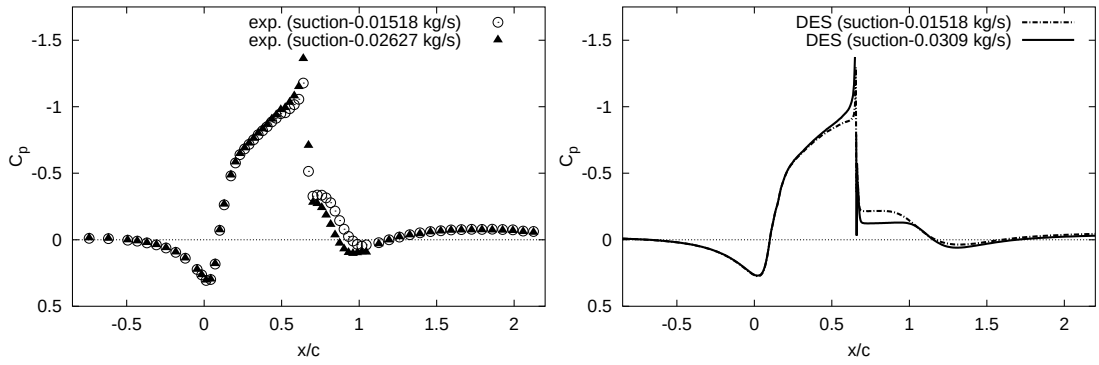

Figure 7.24: Effect of the steady suction mass flow rate on the mean pressure coefficient; experiment (left), DES (right).

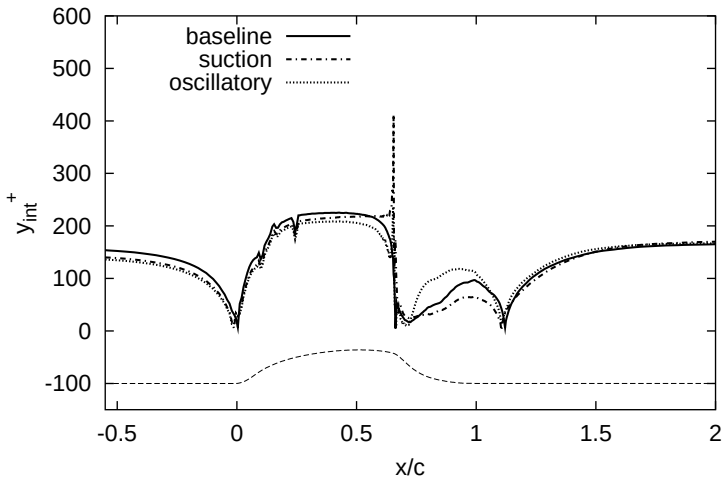

Figure 7.25: RANS-LES interface in DES computations.

advantages of both RANS and LES strategies in different regions of the flow. In the suction case, the position of the interface in terms of the wall units is significantly increased around the slot as shown in Fig. 7.25. Here, the suction control is responsible for thinning of the turbulent boundary layer. It seems that the position of the LES–RANS interface needs to be shifted towards the wall to improve predictions of the flow featuring such a shallow separation. Hence, an important outcome regarding hybrid simulations of flows with separation control in general can be recognized. As flow control affects the structure of the boundary layer on the verge of separation, the LES–RANS interface changes in terms of the wall units but actually remains fixed in absolute sense. The question that arises is whether a grid used for the baseline case can be successfully utilized to predict different flow control scenarios as well, i.e. suction and oscillatory flow control?

7.3.3 Oscillatory Suction/Blowing Flow Control

The LES and DES results of the oscillatory case computations will be assessed next. Among the flow configurations considered, the oscillatory case seems to be the most challenging one. Influence of the modeling of the control slot on the flow predictions in the oscillatory case is addressed first. Predictions of the time-mean velocity and turbulence fields will be then compared with the experimental data. The flow topology and effect of the oscillatory control on the flow structure will be investigated by some snap-shots of the instantaneous flow field. In addition, the phase-averaged behavior of the flow field will be examined by comparing the LES against the phase-averaged quantities available from the measurements.

7.3.3.1 Influence of the Control Slot Modeling

Unlike the steady suction case ($\dot{m}_{suc} = 0.01518\ kg/s$), the oscillatory flow control is achieved applying the zero efflux blowing with the peak mass flow rate of $\dot{m}_{osc-peak} = 0.0179\ kg/s$. As the experimental conditions are specified in terms of the peak slot velocity ($V_{peak} = 26\ m/s$), which is a *locally* measured value, a due attention has to be payed if meaningful velocity boundary conditions are to be applied at the slot. For this reason, a series of simulations, both LES and DES, is performed in order to assess the effect of alternative choice of velocity boundary conditions for modeling the slot jet instead of simulating the flow inside cavity. Initially, the measured peak velocity of $V_{slot-normal} = 26\ m/s$ (normal to the slot) is assumed at the slot. Consequently, the resulting peak mass flow rate is doubled compared to the measured value. Alternatively, the axial velocity component is imposed as $U_{slot} = 26\ m/s$ while the remaining velocity component is adjusted to match the experimental mass flow rate. Finally, the slot normal velocity of $V_{slot-normal} = 13.52\ m/s$, corresponding to the experimental mass flow rate, is adopted as a velocity boundary condition. Table 7.2 summarizes the separation and reattachment locations obtained by the simulations employing different velocity boundary conditions. The results indicate that control effects on the hump flow are almost unaffected by the choice of velocity boundary conditions. Based on the

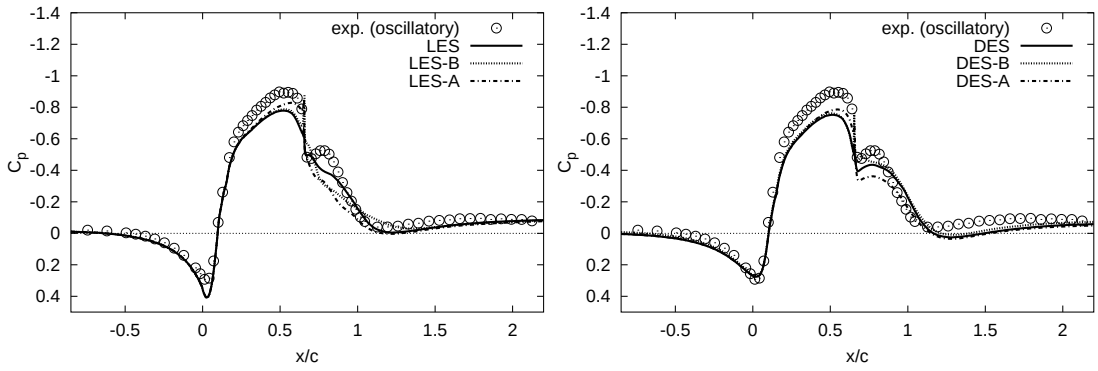

Figure 7.26: Effect of the slot velocity boundary condition on the mean pressure coefficient; LES (left), DES (right).

Table 7.2: Separation and reattachment locations obtained by LES and DES applying different velocity boundary conditions at the control slot

	B.C. at the control-slot	$(x/c)_S$	$(x/c)_R$
Exp.	$\dot{m}_{exp-peak} = 0.0179\ kg/s$	≈ 0.677	≈ 1.0
LES	$\dot{m}_{exp-peak}$, $V_{slot-normal} = 13.52\ m/s$	0.671	1.050
LES-A	$\dot{m}_{exp-peak}$, with $U_{slot} = 26\ m/s$ imposed	0.675	1.026
LES-B	$\dot{m}_{peak} = 0.0344\ kg/s$, $V_{slot-normal} = 26\ m/s$	0.672	1.057
DES	$\dot{m}_{exp-peak}$, $V_{slot-normal} = 13.52\ m/s$	0.662	1.110
DES-A	$\dot{m}_{exp-peak}$, with $U_{slot} = 26\ m/s$ imposed	0.669	1.095
DES-B	$\dot{m}_{peak} = 0.0344\ kg/s$, $V_{slot-normal} = 26\ m/s$	0.660	1.114

predictions of flow separation and reattachment, a slightly closer agreement with the measured values is observed in the simulations LES-A and DES-A which impose the axial velocity of 26 m/s at the slot with the remaining velocity component conforming to the experimental mass flow rate. Profiles of the mean streamwise velocity displayed in Fig. 7.27 - upper and middle reveal somewhat better DES-A predictions whereas LES-A does not show any evident sign of superiority compared to the other boundary conditions. Therefore, no solid conclusion can be drawn based solely on the first moments. The same holds for the pressure coefficient distributions plotted in Fig. 7.26. However, one can distinguish a better performance of DES and LES runs in the recirculation region. Indeed, this boundary condition, i.e. the normal slot velocity corresponding to the experimentally measured peak mass flow rate, seems to be the most realistic approximation to the experiments, as far as this grid topology is concerned. This is clearly visible if the profiles of shear stress shown in Fig. 7.27-lower are examined. Hence, in what follows the predictions of two runs denoted simply by DES and LES (see Table 7.2) will be compared with the time-averaged results of the oscillatory control experiment.

7.3.3.2 Time-mean Velocity and Turbulence Fields

The control mechanism of the oscillatory case turns out to be less effective than the one of steady suction, as observed in the experiment as far as the separation delay and recirculation zone shortening are concerned (Table 7.1). A reduction of the reattachment length compared to the baseline case is reproduced by both LES and DES, but DES overpredicts the reattachment location. The mean pressure coefficient distributions shown in Fig. 7.28 reveal even more pronounced wall blockage effects in the experiment with the oscillatory control. DES and LES perform comparably well

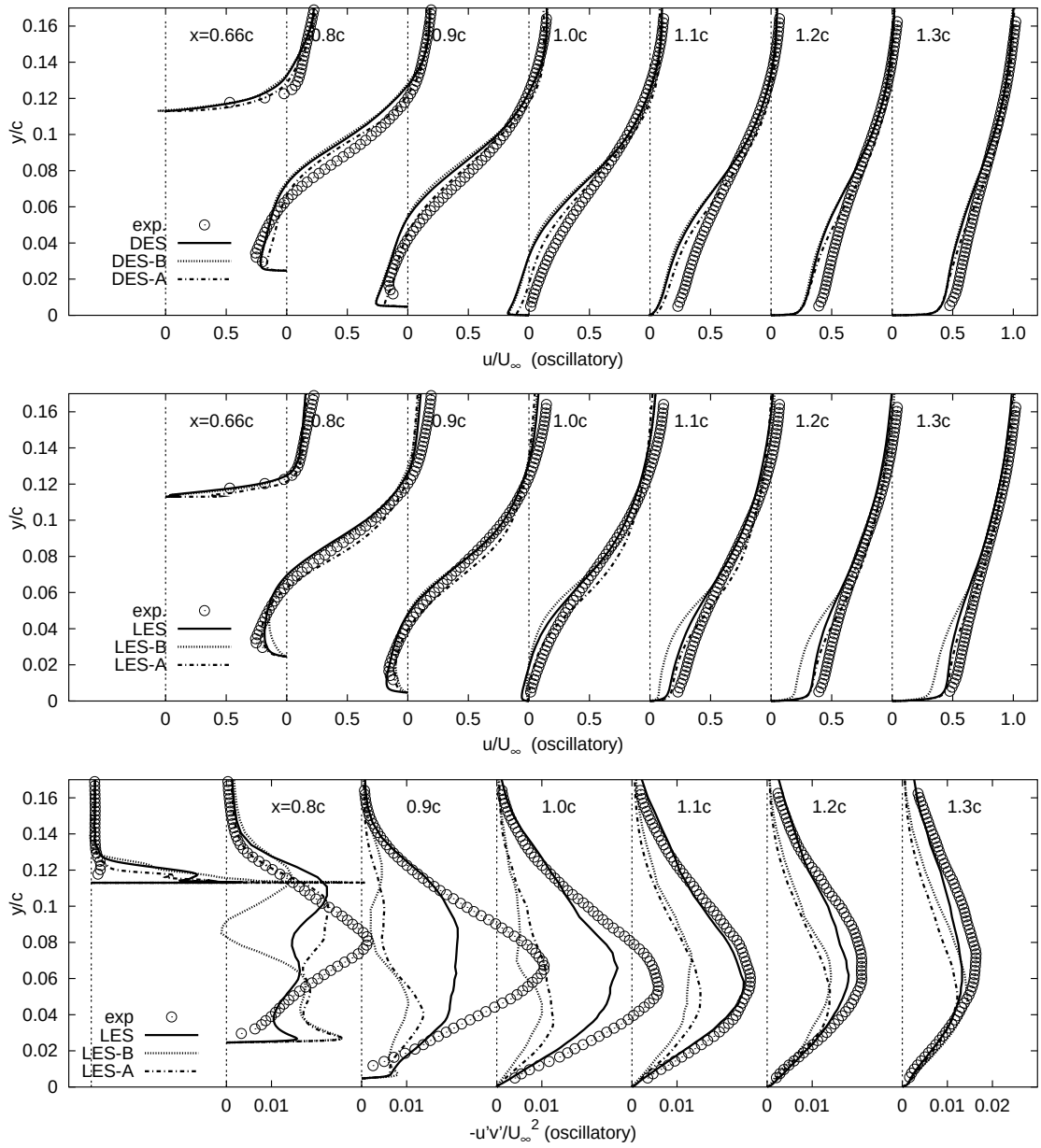

Figure 7.27: Influence of the slot velocity boundary conditions on the hump flow (oscillatory case); Mean streamwise velocity profiles obtained by DES (upper) and LES (middle); shear stress profiles obtained by LES (lower)

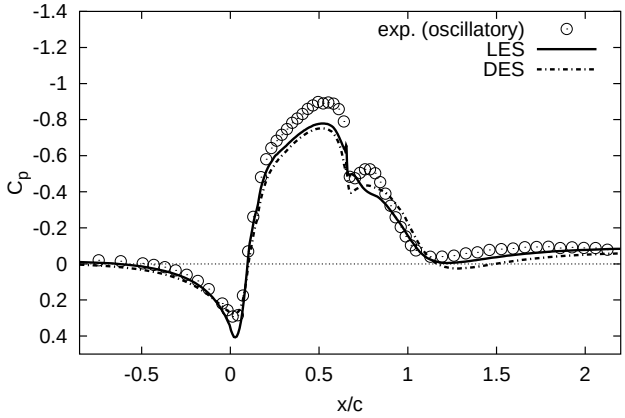

Figure 7.28: Mean pressure coefficient profiles (oscillatory case)

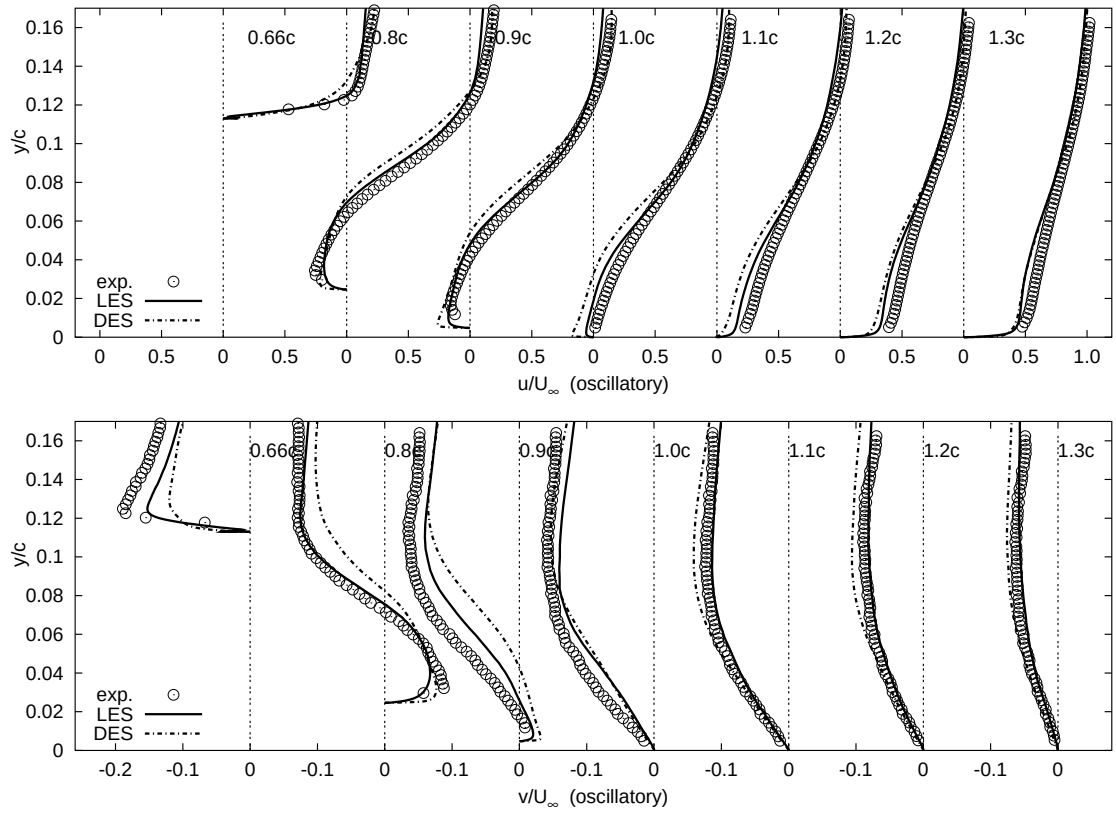

Figure 7.29: Mean streamwise (upper) and wall-normal (lower) velocities obtained by LES and DES (oscillatory case)

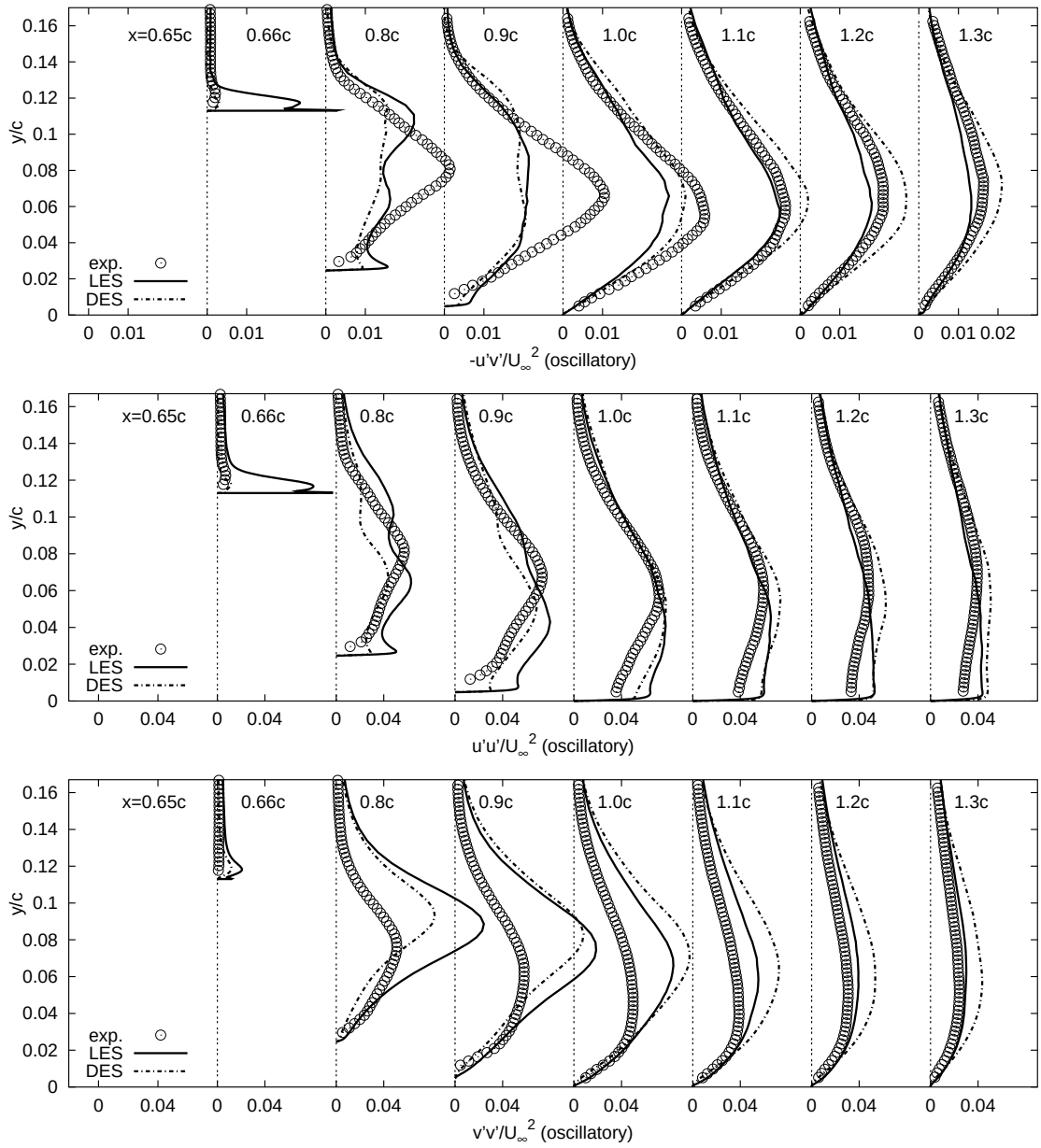

Figure 7.30: Shear stress (upper), streamwise (middle) and wall-normal stress (lower) profiles obtained by LES and DES (oscillatory case)

upto the separation location. Further downstream, LES fails to capture the pressure minimum in the recirculating region whereas DES reproduces the behavior of C_p in this region of the flow. Downstream of the flow reattachment DES overprediction of the pressure recovery is observed. Predictions and measurements of the mean streamwise and wall-normal velocities are compared in Fig. 7.29. Compared to DES, LES yields more accurate velocity predictions, particularly in the recirculation region. Shear stress profiles are shown in Fig. 7.30-upper. An overprediction of the shear stress at the location $x/c = 0.66$, which was observed in the baseline case, is extremely pronounced and could be attributed to the grid resolution which is not sufficiently fine for the oscillatory flow configuration. Some wavy profiles of the shear (Fig. 7.29-upper) and streamwise stresses (Fig. 7.29-middle) might be an indicator of poor data convergence. However, the flow statistics taken over a period of five flow through times ($FTT = L_x/U_\infty$) are monitored and compared during the simulations as displayed in Fig. 7.31. The results demonstrate that even two

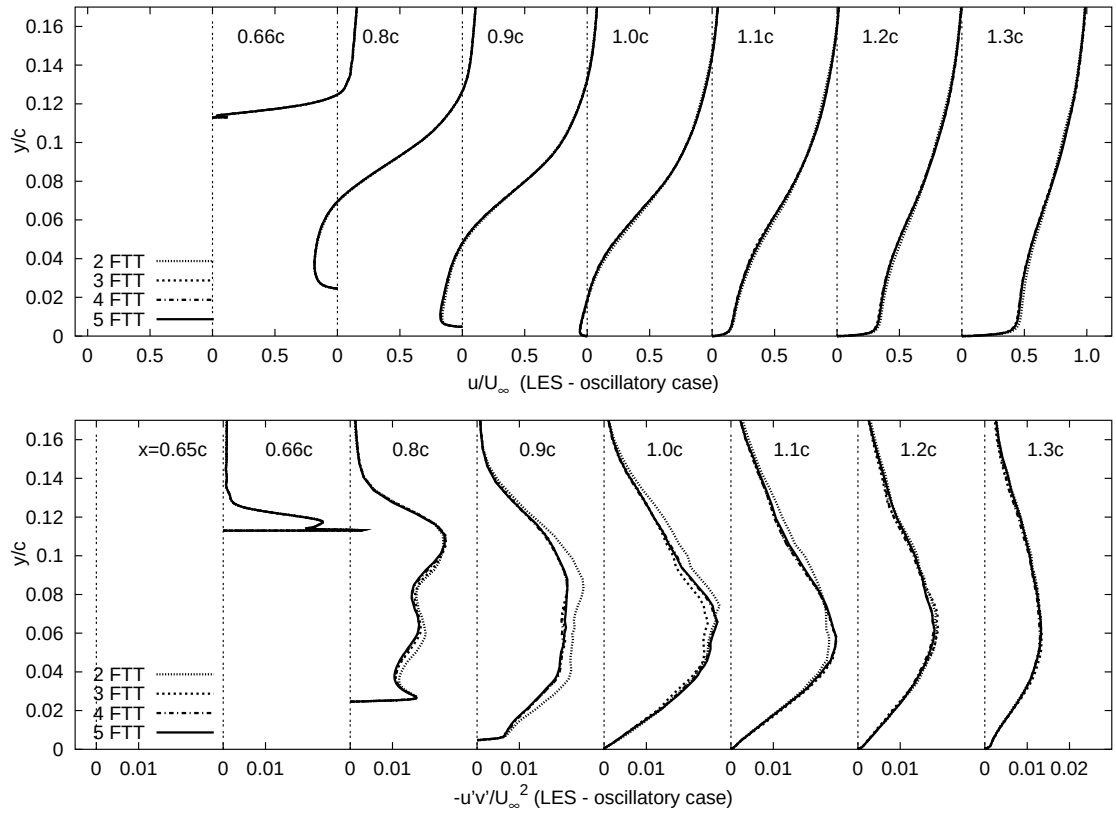

Figure 7.31: Convergence of the streamwise velocity and shear stress statistics taken over different periods of the flow-through times (oscillatory case)

FTT are sufficient to obtain reliable first moments, whereas second moments, e.g. shear stresses, require a somewhat longer time integration period of at least four FTT. In general, with respect to the flow Reynolds number and grid resolution, all stress components are predicted fairly well. Underpredictions of the shear stress and overpredictions of the wall-normal stress in the separated shear layer are a

consequence of insufficient grid resolution. Since the oscillatory flow control induces large-scale vortical structures in the separated shear layer, the flow structure is substantially modified. Therefore, the resolution requirements for the baseline flow become inadequate in the oscillatory case. For instance, a strong interaction of the structures in the separated shear layer with the wall leads to an intensification of the turbulence in the near-wall region. A coarse grid resolution often results in the overpredicted streamwise stress which is consistently present in this region of the flow (see Fig.7.30-middle). On the other side, it is remarkable that comparison of the mean velocity profiles reveals more accurate DES predictions than in the suction control case.

7.3.3.3 Effects of the Flow Control

The effects of the flow control on the velocity and turbulence field are clearly visible. Experiments have shown that shortening of the recirculation bubble by 42% and 26%, compared to the baseline case, is achieved by applying steady suction and oscillatory flow control respectively. LES predictions of the control effectiveness are in close agreement; the same tendency of the mean velocity field is achieved (Fig. 7.32), while shortening of the recirculation bubble is slightly underpredicted: 38% and 25% for the two control mechanisms. Not only qualitative but also quantitative

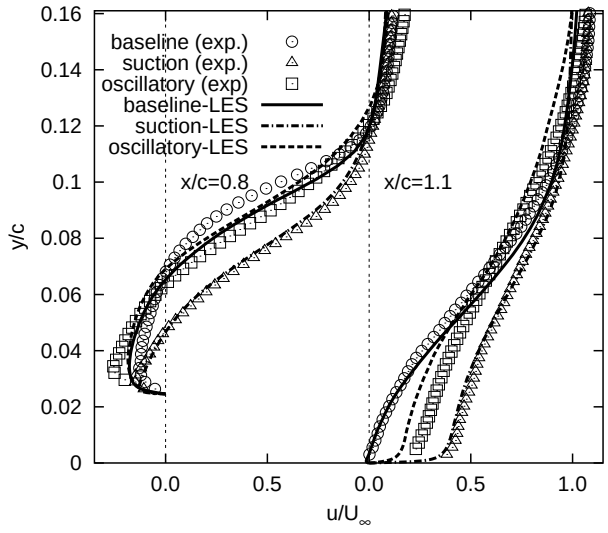

Figure 7.32: Effect of the flow control on the mean velocity profiles at x/c=0.8 and x/c=1.1 (LES vs experiment)

agreement of LES with the measurements is observed as documented by the mean velocity and shear stress profiles in Fig. 7.33. Just upstream of the separation location ($x/c = 0.66$), LES closely follows the trend of streamwise velocity modification. In particular, a strong flow acceleration due to the suction is clearly reproduced. As discussed previously, LES suffers from a coarser resolution in this flow region which comes into play when the flow control is applied. Consequently, in both control cases the shear stress is overpredicted at this station. Further downstream at $x/c = 0.8$

and 0.9 LES returns response of the flow to the suction control whereas the oscillatory control effect is not fully reproduced. This is confirmed by the shear stress distributions at these locations which clearly show the movement of the peak shear stress towards the wall (suction case) that is an indication of enhanced turbulent mixing. Due to disagreement just upstream, LES fails to produce a distinct shear stress peak at $x/c = 0.9$ (oscillatory case). However, at the remaining locations ($x/c \geq 1.0$) LES consistently follows the trend in velocity and shear stress distributions. A remarkable increase in the shear stress in the region corresponding to $y/c \geq 0.06$ is captured which should be actually expected from LES since this region is populated by large-scale vortices induced by the oscillatory jet.

7.3.3.4 Instantaneous and Phase-averaged Flow Fields

Isosurface of the instantaneous pressure fluctuation obtained by DES is shown in Fig. 7.34-a. This visualization shows the roll-up of the spanwise vortex, which is formed in the region of the contol slot, experiencing disruption due to high streamwise vorticity just downstream of the slot. By inspection of the vorticity magnitude (colored by pressure) in Fig. 7.34-d, one can observe that the oscillatory control mechanism tends to reorientate the spanwise vorticity field into streamwise vortices. This can be explained by increased velocity fluctuations in the separated shear layer, in both the wall-normal and particularly spanwise direction as demonstrated in Fig. 7.35. In order to elucidate coherent flow structures, isosurface of the spanwise vorticity is displayed in Fig. 7.34-b. The DES treatment of the separated region results in clearly visible resolved vortical structures. Evolution of the large-scale spanwise vortices downstream of the slot is observed as a result of the imposed oscillatory perturbation. Despite an effectively two-dimensional flow field, the three-dimensional instantaneous flow structures (vortices disrupted in the spanwise direction) can be identified. Evidently, the spanwise domain of $0.2c$ employed for DES appears to be sufficient for capturing streamwise vortices displayed in Fig. 7.34-c.

One of the experimentally observed features of the oscillatory case is that typically two to three vortices were present in the PIV-measurements region covering the entire separation bubble and the reattachment region up to $x/c = 1.3$ at any instant. This can be seen in Fig. 7.36, showing the instantaneous velocity field snap-shots for different phase angles produced by LES. It displays generation, roll-up and shedding of the vortices through the phase angles of 90° (blowing peak), 180° (switch from blowing to suction), 270° (suction peak) and 360° (switch from suction to blowing). By careful inspection of this figure one can discern the movement of separation point as found in the experiment. A picture of the flow is completed by the phase-averaged velocity fields displayed adjacent to the instantaneous ones. It is to be noted that the sample LES data set is limited to 50 blowing/suction cycles, yet it provides a useful and credible information about the phase-averaged behavior. At the instant corresponding to the blowing peak ($\Phi = 90°$) the separation zone moves upstream towards the slot, the shear layer being lifted off the wall. This is in accord with the experimental findings so that one can speak of actual promotion of the separation at this phase angle. At the same time the reattachment length is reduced

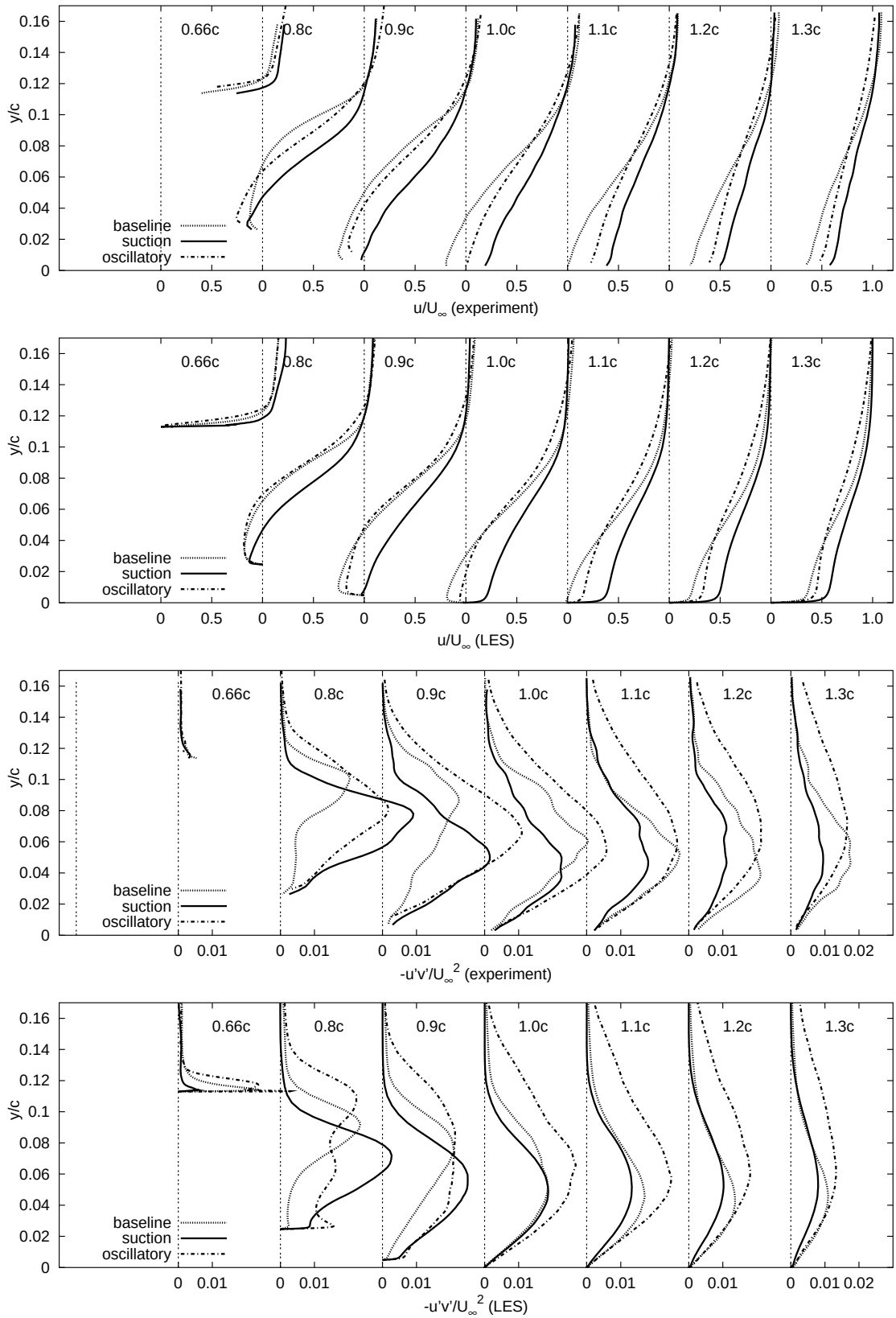

Figure 7.33: Effects of the flow control on the streamwise velocity and shear stress; Mean streamwise velocity profiles: a) experiment, b) LES; Shear stress profiles: c) experiment, d) LES

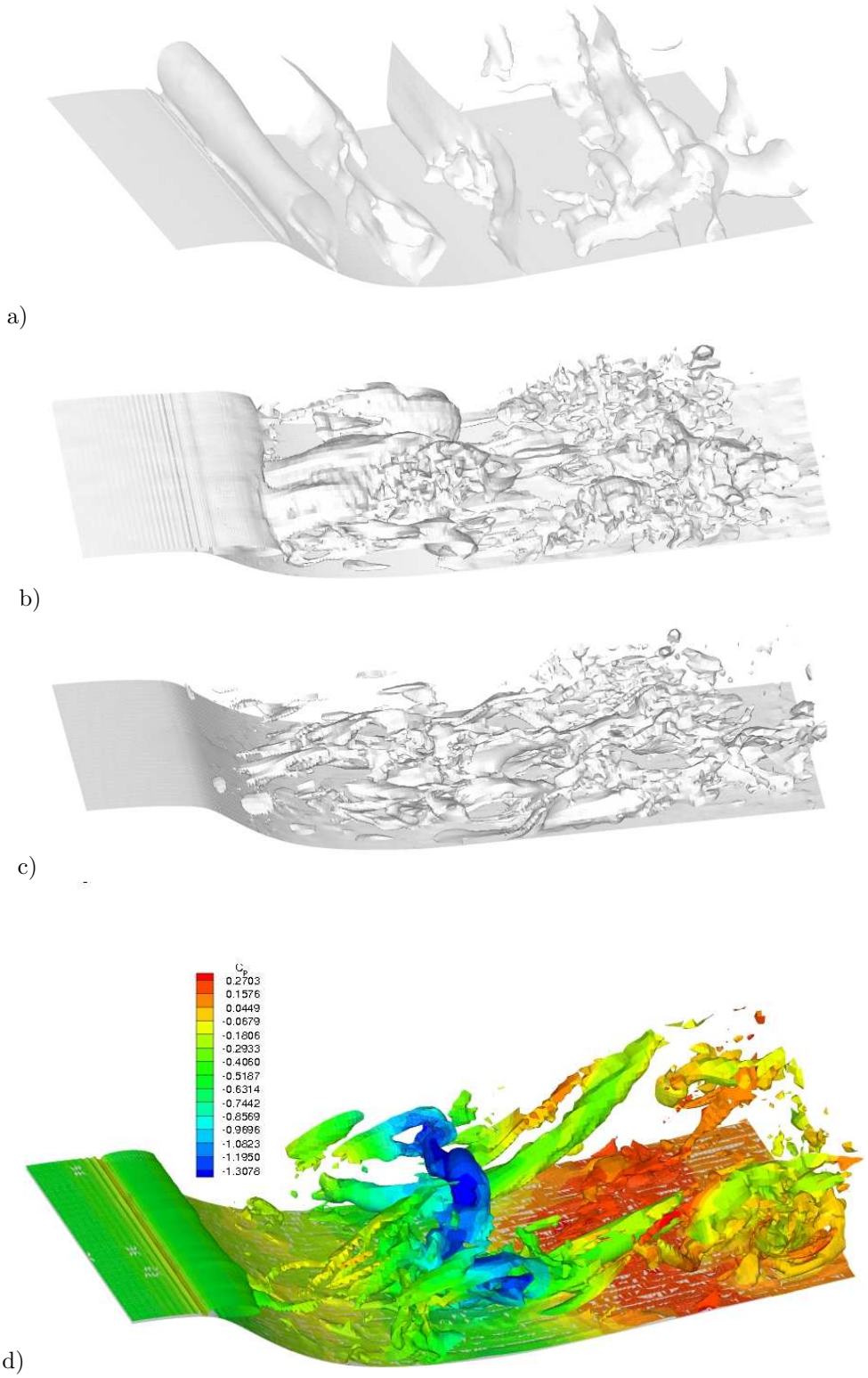

Figure 7.34: DES predictions of the oscillatory flow control case: Iso-surfaces of the instantaneous pressure fluctuation (a), spanwise vorticity (b), streamwise vorticity (c) and vorticity magnitude colored by pressure coefficient (d)

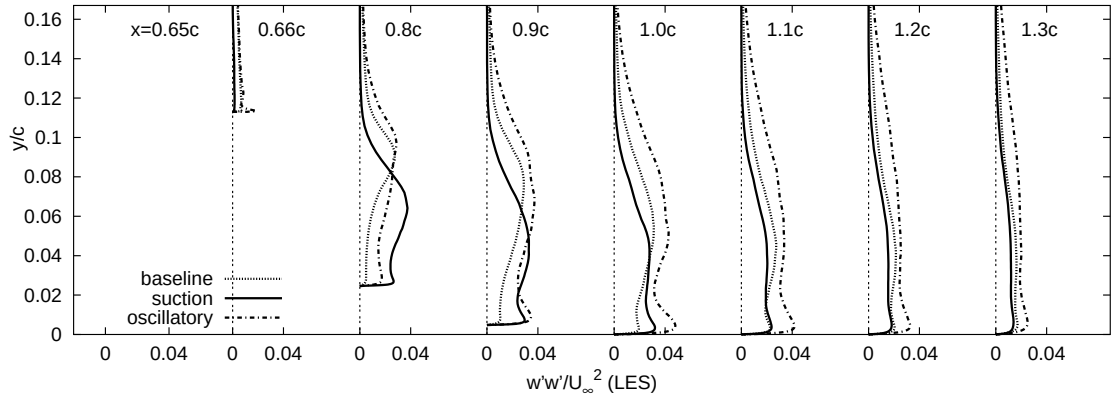

Figure 7.35: Effect of the flow control on the mean spanwise stress profiles (LES)

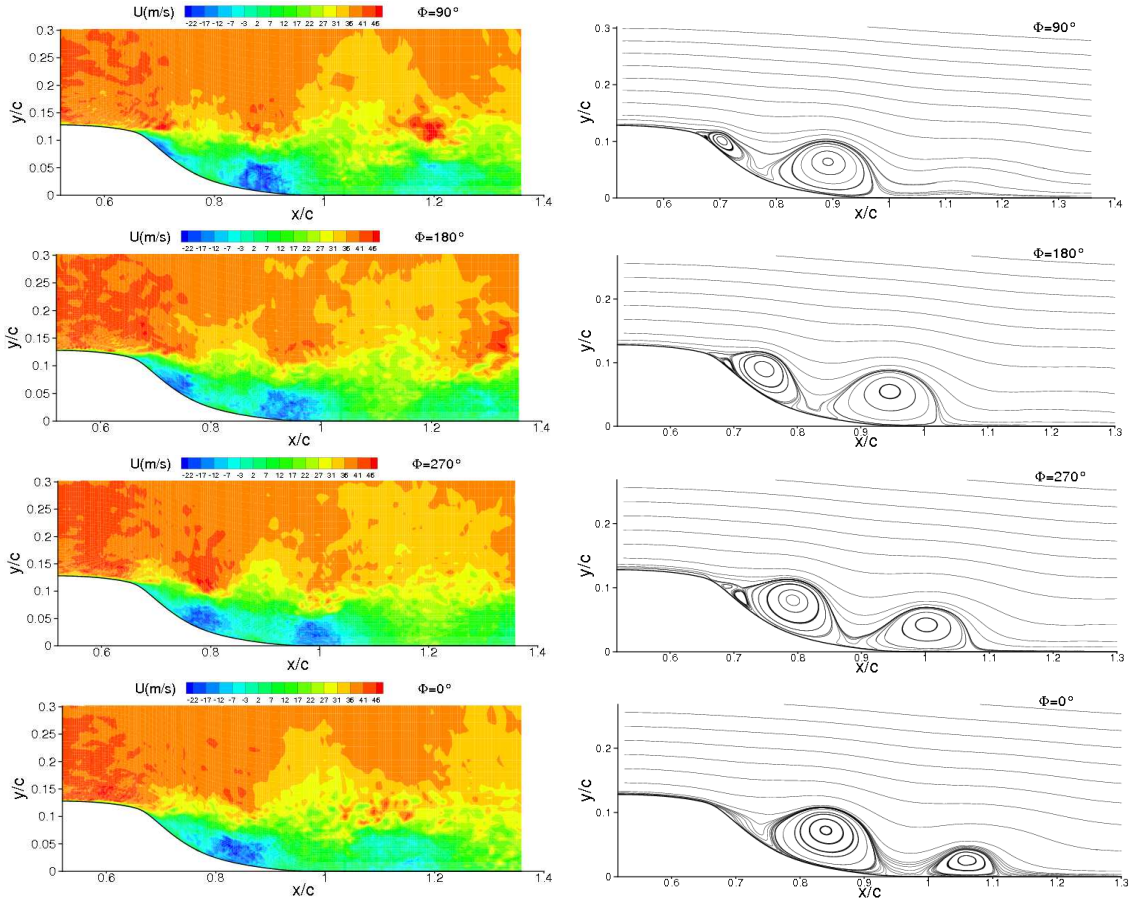

Figure 7.36: Instantaneous streamwise velocity field obtained by LES for various phase angles

significantly as can be seen by close inspection of the phase-averaged skin-friction coefficient shown in Fig. 7.37. A vortex that is rolled-up at this stage is convected downstream noting concomitant formation of a secondary small vortex visible at $\Phi = 180°$ as the control switches from blowing to suction. As the suction peak is reached ($\Phi = 270°$), the shear layer is pulled towards the wall and separation point moves downstream of the slot. The skin-friction at this phase reveals a movement of the flow reattachment downstream exceeding the long time-averaged value. A small secondary vortex just downstream of the slot is disrupted into two smaller vortices which eventually vanish as the control switches from suction to blowing ($\Phi = 0°$). Based on the skin-friction evolution (Fig. 7.37) one can observe that the reattachment location at this phase angle reaches its maximum. Concerning existence of two to three vortices within the instantaneous recirculation zone, it is recalled that a similar observation in the periodically perturbed backward-facing step flow was reported by Yoshioka et al. [77]. It is encouraging that LES accurately predicts the convective speed of the vortices estimated as $U_{cv} \approx 0.36U_\infty$, the measured value being $U_{cv} \approx 0.35U_\infty$. A curious result obtained both experimentally and numerically (LES) is that convective velocities at which the large-scale vortices (emerged either from the step or from the control slot) move downstream are very close to each other, $0.3U_c$. vs. $0.35U_\infty$.

Phase-averaged coherent part of the pressure coefficient obtained for the four representative phase angles by subtracting the long time-averaged C_p ($\tilde{C}_p =< C_p > - C_p$) is plotted in Fig.7.38. Despite encouraging agreement for the phase angles corresponding to the blowing ($\Phi = 90°$) and suction ($\Phi = 270°$) peaks, LES captures only a trend of $\tilde{C}_p$ for the two remaining angles. For each of angles, there is either a considerable overprediction or underprediction of $\tilde{C}_p$. It is difficult to find a proper explanation for such a curious result especially because the phase-averaged skin-friction profiles do not exhibit such an odd behavior for the given phases. One should however point out that although these two deviations cancel each other in the long time-averaged C_p, undulations of the mean pressure coefficient obtained by LES and failure to capture the second pressure minima in Fig. 7.28 could be associated with this disagreement disclosed by the phase-averaged plots.

Regarding the phase-averaged profiles of streamwise velocity which are displayed in Fig.7.39, one can see that LES predictions are in very close agreement locally, depending on the phase angle and station considered. Likewise, certain local deviations from the measurements are noted. Certainly, the data sampled over 50 cycles are not sufficient to obtain smooth and absolutely reliable profiles as demonstrated by the phase-averaged shear stress distributions shown in Fig.7.40. However, it is noteworthy to emphasize qualitatively good agreement of the phase-averaged shear stress predicted by LES. Local discrepancies may be attributed to the resolution issues but one should keep in mind the maximum uncertainty in the measured stresses estimated as 20%. A distinct feature of the hump flow subjected to the oscillatory control can be recognized by carefull inspection of the phase-averaged shear stress profiles in line with the evolution of skin-friction (cf. 7.37). One can see that shear stress maxima occur consistently at the location in vicinity of the local reattachment (in the phase-averaged sense). In accordance with the previ-

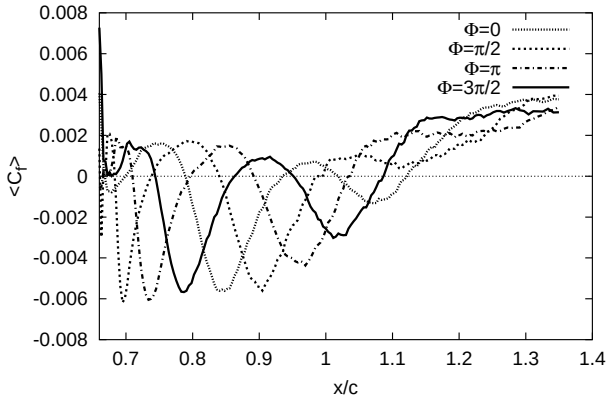

Figure 7.37: Phase averaged skin-friction coefficient

ous discussion of the phase-averaged behavior, the shear stress peaks are identified around $x/c = 1.0$ at the phase angles $\Phi = \pi$ and $3\pi/2$, upstream of the time-mean reattachment ($x/c = 0.9$) at $\Phi = \pi/2$ and downstream thereof ($x/c = 1.1$) at $\Phi = 0$.

Concluding Remarks

Different computational approaches: LES (Large-eddy Simulation), DES (Detached-eddy Simulations) and RANS (Reynolds-Averaged Navier-Stokes) were used to predict the flow over a wall-mounted hump aiming at comparative analysis of their features and performances in such complex flow situations relevant to the aircraft aerodynamics. In addition to the baseline case, the computations of the two configurations with active flow control realized by steady suction and oscillatory blowing/suction through a narrow opening (1.7 mm wide) at the hump crest close to the natural separation point were performed. Among the flow configurations considered, the oscillatory case appears to be the most challenging one for the unsteady flow computational strategies like LES and DES. The LES and DES predictions of the main characteristics of separated flow over a wall-mounted hump, obtained on relatively coarse grids with respect to the flow Reynolds number considered ($Re_c = 9.36 \cdot 10^5$), are encouraging, outperforming significantly the examined RANS models. As it was expected, the RANS approach was not capable of capturing the dynamics of the large scale motion being especially pronounced in the separated shear layer. A typical outcome is expressed in a lower turbulence level in this flow region leading consequently to a larger recirculation zone and decreased sensitivity against perturbations. LES provided good predictions of the important effects of steady suction and oscillatory suction/blowing flow control, i.e. a shortening of the recirculation bubble compared to the reference baseline case. The DES results are almost identical to those obtained by using the conventional LES in the baseline case. It is especially encouraging when one knows that a lower grid resolution (only 1.7 Mio. cells in total vs 4 Mio. cells for LES) was applied. However, poorer performance in the suction case (LES superior to DES) indicates the importance of the DES grid design with respect to this controlled flow featuring a thinner boundary layer upstream of the separation. The issue of LES–RANS interface appears to be crucial

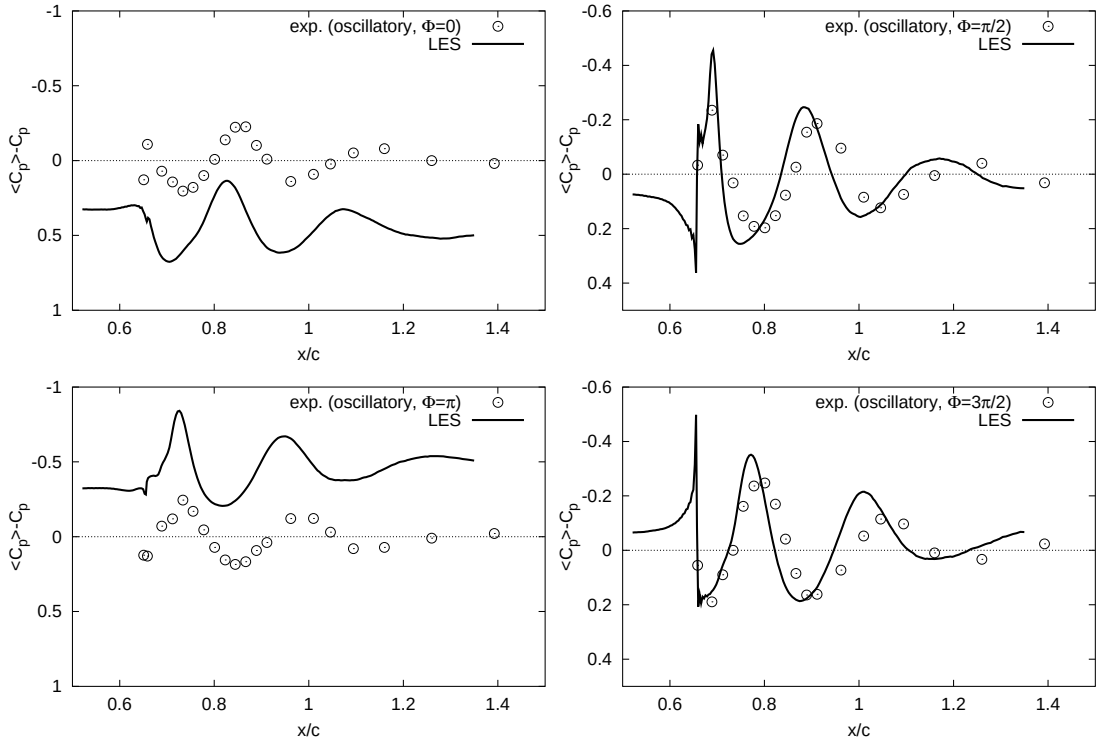

Figure 7.38: Coherent part of the pressure coefficient ($\tilde{C}_p =< C_p > - C_p$)

for exploiting advantages of both RANS and LES strategies in different regions of the flow. Comparison of the interface positions in all three flow configurations gives a rise to the question whether a grid used for the baseline case can be used for different flow control scenarios, i.e. suction and oscillatory flow control? Simulations of the oscillatory case demonstrate in general good predictions of the recirculation bubble, both instantaneously and in the time mean sense. Close agreement with the experiment is observed regarding the velocity and shear stress profiles. Despite relatively coarse grid resolution and a narrow computational domain in the spanwise direction ($L_{z,LES} = 0.152c$ and $L_{z,DES} = 0.2c$), it was possible to capture the three-dimensional instantaneous flow structures. The mean velocity field is not affected by the choice of slot velocity boundary condition, but an appropriate modeling conforming with the experimental mass flow rate is essential for capturing the turbulence characteristics within the recirculation zone. Finally, the phase-averaged results extracted from LES of the oscillatory controlled hump flow are in good agreement with the measurements, reproducing the main control mechanisms observed in the experiments. LES predicts accurately the convective speed of the vortices estimated as $U_{cv} \approx 0.36U_\infty$, the measured value being $U_{cv} \approx 0.35U_\infty$. A curious result obtained both experimentally and numerically (LES) is that convective velocities at which the large-scale vortices (emerged either from the step or from the control slot) move downstream are very close to each other, $0.3U_c$. vs. $0.35U_\infty$.

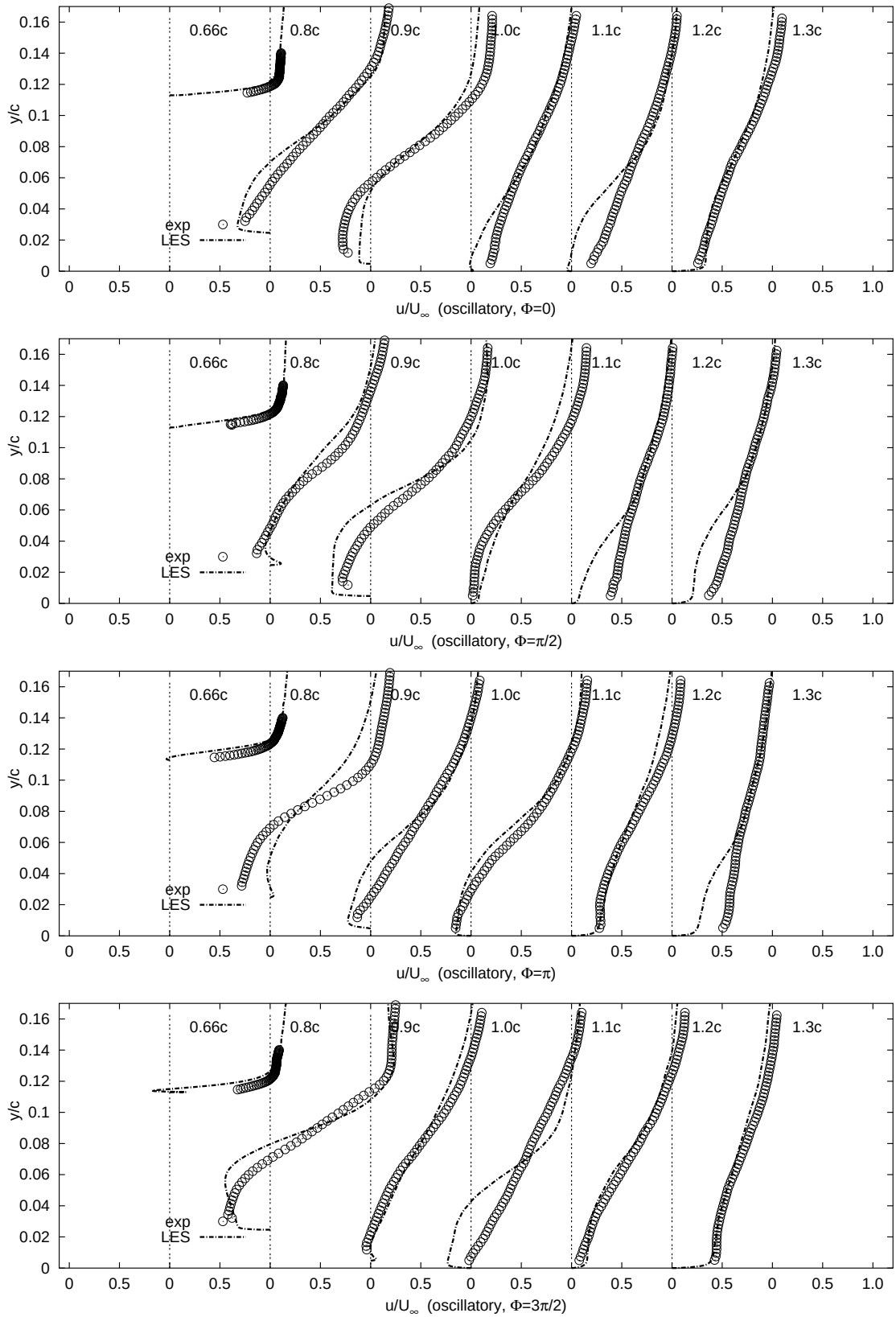

Figure 7.39: Phase-averaged streamwise velocity predicted by LES

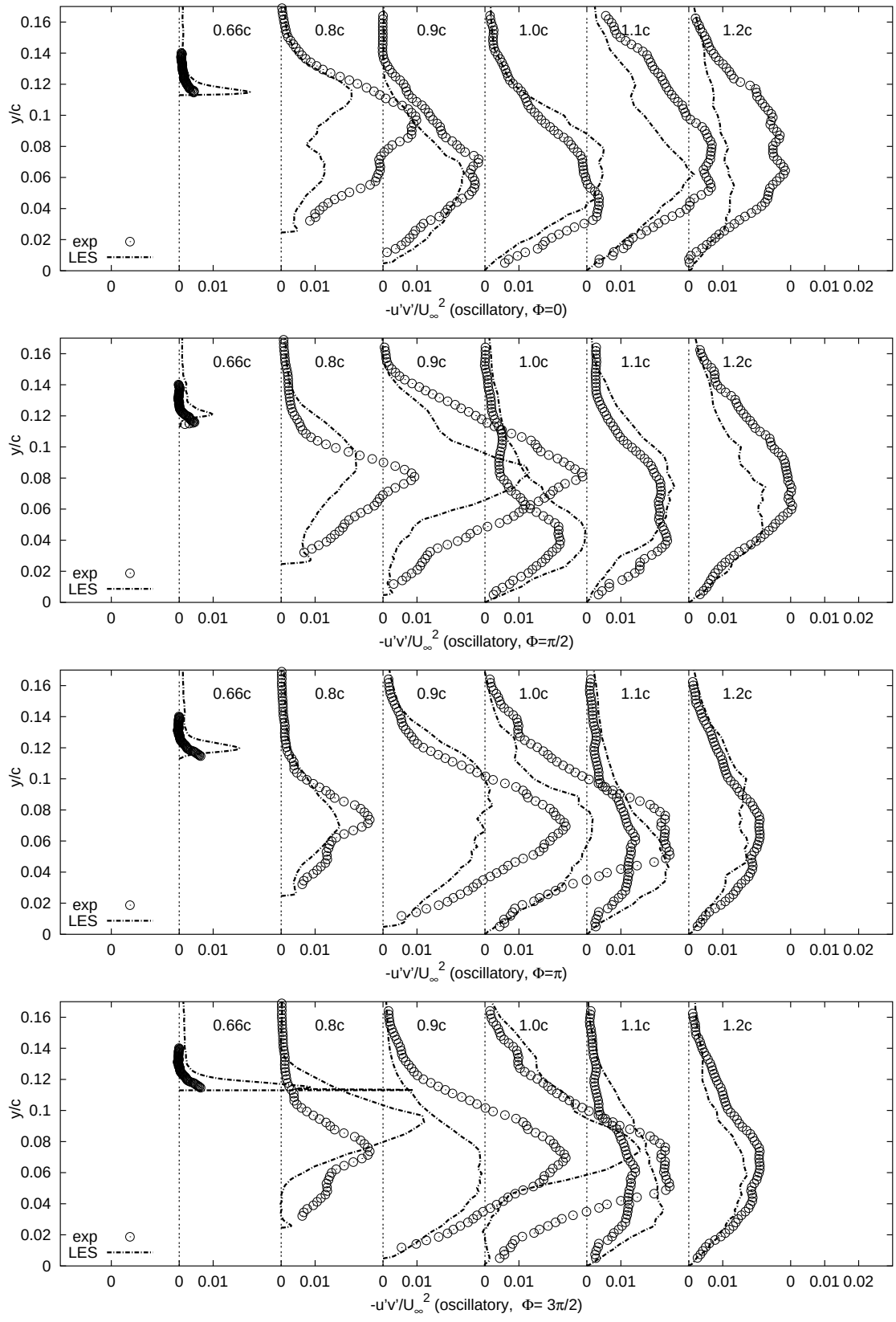

Figure 7.40: Phase-averaged shear stress predicted by LES

8 Conclusions and Recommendations

In the last chapter the main outcomes and conclusions inferred from the present work are summarized. Finally, directions and recommendations for future work are outlined.

8.1 Conclusions

The main goal of this work was a computational study of the effects of boundary-layer forcing on the mean flow and turbulence using various methods for turbulent flow computations (LES, DES and RANS), with an emphasis on the unsteady approaches LES and DES, aiming also at mutual comparison of their features and performance in complex flow situations. The numerous simulations of the flow configurations pertinent to active flow control (AFC) have been carried out providing a picture of the current status of CFD in AFC applications.

Predictive capability of various CFD methods were evaluated for the three representative complex separated flow configurations without flow control. Arguably, it seems to be unlikely that any existing RANS model, regardless of its complexity, can provide the accurate predictions needed in a number of complex separated and vortical flows. Obviously, RANS requires additional modeling and empiricism to achieve credible AFC predictions. A potential of the methods for unsteady flow computations: LES, DES and URANS was investigated by predicting the flow and turbulence field for the two experimentally investigated AFC configurations. They involve the two recent experimental works pertinent to AFC: periodically perturbed backward-facing step (BFS) flow at a low Reynolds number (Yoshioka et al. [77, 78]) and high Reynolds number flow over a wall-mounted hump (Greenblatt et al. [22, 23]). The following conclusions can be drawn based on the results of the present study:

• In general, both the LES and DES computations have reproduced all important effects observed in the BFS experiments. The imposed perturbation frequency corresponding to $St = 0.19$ was found to be the optimum one, leading to the maximum reduction of the reattachment length. Compared to the measured value of 28.3%, LES and DES exhibit the closest agreement, predicting the reduction of 24.5 and 35%, respectively. URANS underpredicts substantially the intensity of the reduction with 5.9% (SA model) and 12.9% ($k - \omega$ SST model), exhibiting a very weak sensitivity to the perturbations.

• A computational analysis of the influence originating from the inflow boundary conditions has shown that there is a certain impact of the inlet turbulence intensity on the flow around and downstream the reattachment. However, it is be-

lieved that the imposed inlet profiles are not appreciably influential.

• Overall comparison of the mean flow and turbulence for different perturbation frequencies has shown a close agreement of LES and DES predictions with the experimentally observed trends. Not only a general enhancement of the turbulence production with the perturbation was reproduced but also the frequency dependence of the Reynolds stress increase. Some peculiarities in the stress field arising from the flapping motion of the perturbed shear layer were captured by LES and DES.

• Beside a close agreement with the experiment concerning time-mean behavior of the flow for all perturbation frequencies, the extracted phase-averaged LES results for the case with the optimum frequency ($St = 0.19$) compare well with the reference experimental data.

• Among the hump flow configurations considered, the oscillatory case appears to be the most challenging one. The LES and DES predictions of the main characteristics of separated flow over a wall-mounted hump, obtained on relatively coarse grids with respect to the flow Reynolds number considered ($Re_c = 9.36 \cdot 10^5$), are encouraging, outperforming significantly the examined RANS models. As it was expected, the RANS approach was not capable of capturing the dynamics of the large scale motion in both the baseline and steady suction cases, being especially pronounced in the separated shear layer. A typical outcome is expressed in a lower turbulence level in this flow region leading consequently to a larger recirculation zone and decreased sensitivity against perturbations.

• LES provided good predictions of the important effects of steady suction and oscillatory suction/blowing flow control, i.e. a shortening of the recirculation bubble compared to the reference baseline case. The DES results are almost identical to those obtained by using the conventional LES in the baseline case. It is especially encouraging when one knows that a lower grid resolution (only 1.7 Mio. cells in total vs 4 Mio. cells for LES) was applied.

• A poorer performance of DES in the suction case points to importance of the DES grid design with respect to this controlled flow featuring a thinner boundary layer upstream of the separation. The issue of LES–RANS interface appears to be crucial for exploiting advantages of both RANS and LES strategies in different regions of the flow. The important outcome regarding hybrid simulations of flows with separation control in general can be recognized. As flow control affects the structure of the boundary layer on the verge of separation, the LES–RANS interface changes in terms of the wall units but actually remains fixed in absolute sense. The question that arises is whether a grid used for the baseline case can be successfully utilized to predict different flow control scenarios as well, i.e. suction and oscillatory flow control?

• LES and DES of the oscillatory case demonstrate in general good predictions

of the recirculation bubble, both instantaneously and in the time mean sense. Close agreement with the experiment is observed regarding the velocity and shear stress profiles. Despite relatively coarse grid resolution and a narrow computational domain in the spanwise direction ($L_{z,LES} = 0.152c$ and $L_{z,DES} = 0.2c$), it was possible to capture the three-dimensional instantaneous flow structures.

• The mean velocity field is not affected by the choice of slot velocity boundary condition, but an appropriate modeling conforming with the experimental mass flow rate is essential for capturing the turbulence characteristics within the recirculation zone.

• The phase-averaged results extracted from LES of the oscillatory controlled hump flow are in good agreement with the measurements, particularly encouraging is that LES accurately predicts the convective speed of the vortices estimated as $U_{cv} \approx 0.36U_\infty$, the measured value being $U_{cv} \approx 0.35U_\infty$.

• A curious result obtained both experimentally and numerically (LES) is that convective velocities at which the large-scale vortices (emerged either from the step or from the control slot) move downstream are very close to each other, $0.3U_c$. vs. $0.35U_\infty$.

• With regard to both BFS and hump flow configurations, it was clearly recognized that reduction in the reattachment length follows the evolution of wall-normal stress ($\overline{v^2}$). It has been shown that capturing the near-wall turbulence, especially the wall-normal component, has a great impact on the mean flow predictions downstream of the step/hump.

8.2 Recommendations for Future Work

Based on the results of the present work some directions and issues for future research are proposed as follows:

• Failure of DES to predict the steady suction case should be further investigated. Different grid configurations could be examined in order to achieve predictions comparable to the baseline case, which implies a sort of the interface optimization with respect to the flow considered.

• An attempt to make the LES-RANS interface not only grid-dependant but also locally flow-sensitive would be challenging for hybrid LES-RANS simulations of AFC.

• As the experiments have demonstrated a weak dependency on the flow Reynolds number, the same configurations with a substantially lower Reynolds number could be computed by LES and DES thus providing a well resolved reference data set

which could be used to improve the existing turbulence models. However, decreasing the Reynolds number at the presently used computational grids implies a finer grid resolution which is expected to be more sensitive to the inlet boundary conditions. Hence, unsteady inlet profiles would be required for these simulations.

• Compared to the baseline case RANS predictions of the hump flow have proven to be less accurate in the suction case. Scarcity of RANS calculations of the oscillatory case is motivation for a detailed investigation of the oscillatory flow control case employing solely URANS. This would help answering the question: to what extent RANS approach does work in real AFC applications?

Bibliography

[1] Abe, H., Segawa, T., Kikushima, Y., Yoshida, H., Nishizawa, A., Takagi, S.: *Toward smart control of separation around a wing-active control device part 2.* 5^{th} Symposium on Smart Flow Control of Turbulence, Tokyo, Japan, 2004.

[2] Akselvoll, K., Moin, P.: *Large eddy simulation of a backward facing step flow.* Engineering Turbulence Modelling and Experiments 2, Rodi, W. and Marteli, F. Eds.:, pp. 303–313, 1993.

[3] Almeida, G.P., Heitor, M.V.: *Wake Flows behind Two-Dimensional Model Hills.* Expl. Thermal Fluid Sci., Vol 7 , pp. 87–101, 1993.

[4] Amitay, M., Smith, D.R., Kibens, V., Parekh, D.E, Glezer, A.: *Aerodynamic flow control over an unconventional airfoil using synthetic jet actuators.* AIAA Journal, Vol 39(3) , pp. 361–370, 2001.

[5] Arnal, M., Friedrich, R.: *Large-Eddy Simulation of a Turbulent Flow with Separation.* Turbulent Shear Flows, F. Durst et al., eds., Springer Verlag, Vol 8 , pp. 169–187, 1993.

[6] Breuer, M., Jaffrézic, B.: *Hybrid LES–RANS Technique Based on a One-Equation Near-Wall Model.* EUROMECH Colloquium 469, Large-Eddy Simulation of Complex Flows, Dresden, Germany, October 6-8, 2005.

[7] Breuer, M.: *New Reference Data for the Hill Flow Test Case.* personal communication, `http://www.hy.bv.tum.de/DFG-CNRS/`, 2005.

[8] Breuer, M., Manhart, M., Peller, N., Fröhlich, J., Hinterberger, C., Rodi, W., Deng, G., Chikhaoui, O., Šarić, S. , Jakirlić, S.: *A comparative study of the turbulent flow over a periodic arrangement of smoothly contoured hills.* 6^{th} ERCOFTAC Workshop on Direct and Large-Eddy Simulation *DLES-6*, Poitiers, France, September 12-14, 2005.

[9] Breuer, M., Rodi, W.: *Large-Eddy Simulation of Complex Turbulent Flows of Practical Interest.* In: Flow Simulation with High-Performance Computers II, Notes on Numer. Fluid Mech., Vieweg, 52 , pp. 258–274, 1996.

[10] Breuer, M., Rodi, W.: *Large-Eddy Simulation of the Sub-Critical Flow Past a Circular Cylinder: Numerical and Modeling Aspects.* Int. J. Num. Methods Fluids, 28 , pp. 1281–1302, 1998.

[11] Chun, K.B., Sung, H.J.: *Control of turbulent separated flow over a backward-facing step by local forcing.* Experiments in Fluids, Vol. 21 pp. 417–426, 1996.

[12] Chun, K.B., Sung, H.J.: *Effect of spanwise-varying local forcing on turbulent separated flow over a backward-facing step.* Experiments in Fluids, Vol. 26 pp. 437–440, 1999.

[13] Collis, S.S., Joslin, R.D., Seifert, A., Theofilis, V.: *Issues in active flow control:theory, control, simulation, and experiment.* Progress in Aerospace Sciences, Vol 40 , pp. 237–289, 2004.

[14] Dejoan, A., Jang, Y.-J., Leschziner, M.: *LES and unsteady RANS computations for a periodically-perturbed separated flow over a backward-facing step.* ASME Heat Transfer/Fluids Engineering Summer Conference, Charlotte, NC, USA, 2004.

[15] Dejoan, A., Leschziner, M.: *Large eddy simulation of periodically perturbed separated flow over a backward-facing step.* Int. Journal of Heat and Flow, Vol 25 , pp. 581–592, 2004.

[16] Deng, G.B., Queutey, P., Visonneau, M.: *Three-Dimensional Flow Computation with Reynolds Stress and Algebraic Stress Models.* In: Engineering Turbulence Modelling and Experiments 6, ed. W. Rodi and M. Mulas, ELSEVIER, Charlotte, NC, USA, 2005.

[17] Durst, F., Schäfer M.: *A Parallel Block–Structured Multigrid Method for the Prediction of Incompressible Flows.* Int. J. Num. Methods Fluids, Vol 22 , pp. 549–565, 1996.

[18] Ferziger, J.H., Perić, M.: *Computational Methods for Fluid Dynamics.* Springer, 2002.

[19] Fröhlich, J., Mellen, C.P., Rodi, W., Temmerman L., Leschziner, M.A.: *Highly Resolved Large-Eddy Simulation of Separated Flow in a Channel with Streamwise Periodic Constrictions.* J. Fluid Mech., Vol 526 , pp. 19–66, 2005.

[20] Germano, M., Piomelli, U., Moin, P., Cabot, W.: *A dynamic subgrid-scale eddy viscosity model.* Physics of Fluids, Vol A(3) , pp. 1760–1765, 1999.

[21] Gibson, M.M., Launder, B.E.: *Grounds Effects on Pressure Fluctuations in the Atmospheric Boundary Layer.* J. Fluid Mech., Vol 86 , pp. 491–511, 1978.

[22] Greenblatt, D., Paschal, K.B., Yao, C.-S., Harris, J.: *A Separation Control CFD Validation Test Case Part 2: Zero Efflux Oscillatory Blowing.* AIAA 2005-0485, 2005.

[23] Greenblatt, D., Paschal, K.B., Yao, C.-S., Harris, J., Schaeffler, N.W., Washburn, A.E.: *A Separation Control CFD Validation Test Case Part 1: Baseline and Steady Suction.* AIAA 2004-2220, 2004.

[24] Hanjalić, K., Jakirlić, S.: *Contribution towards the second-moment closure modelling of separating turbulent flows.* Computers and Fluids, Vol 22(2) , pp. 137–156, 1998.

[25] Hanjalić, K.: *Will RANS survive LES? A view of perspectives.* ASME Heat Transfer/Fluids Engineering Summer Conference, Charlotte, NC, USA, 2004.

[26] Hinterberger, C.: *Dreidimensionale und tiefengemittelte Large-Eddy-Simulation von Flachwasserströmungen.* Ph.D. Thesis, University of Karlsruhe, 2004.

[27] Iaccarino, G., Marangiu, P.C., Catalano, P., Amato, M.: *RANS simulation of the separated flow over a bump with active control.* Center for Turbulence Research, Annual Research Brief 2003, Stanford University, CA, USA, 2003.

[28] Jaffrézic, B., Breuer, M., Chikhaoui, O., Deng, G., Visonneau, M.: *Towards Hybrid LES–RANS-Coupling for Complex Flows with Separation.* CEMRACS 2005 Proceedings, Marseille, France, 2005.

[29] Jakirlić, S., Hanjalić, K.: *A new approach to modelling near-wall turbulence energy and stress dissipation.* J. Fluid Mech., Vol 539 , pp. 139–166, 2002.

[30] Jakirlić, S., Jester-Zürker, R., Tropea, C. Proc. 9^{th} ERCOFTAC/IAHR/COST Workshop on refined turbulence modelling, Darmstadt, Germany, 2001.

[31] Jasak, H.: *Error Analysis and Estimation for the Finite Volume Method with Applications to Fluid Flows.* Ph.D. Thesis, University of London, 1996.

[32] Jin, S., Choi, H., Kim , S., Yoo, J.Y., Kim, S.: *An experimental study of turbulent backward-facing step flow under two-frequency forcing.* Proceedings of the fifth World Conference on Experimental Heat Transfer, Fluid Mechanics, and Thermodynamics, Thessaloniki, Greece: pp. 1933–1938, 2001.

[33] Johansson, G., Davidson, L. Proc. 11^{th} ERCOFTAC/IAHR/COST Workshop on refined turbulence modelling, Gothenburg, Sweden, 2005.

[34] Joslin, R.D., Horta, L.G., Chen, F.-J.: *Transitioning active flow control to applications.* 30^{th} AIAA Fluid Dynamics Conference, Norfolk, VA, USA, 1999.

[35] Kasagi, N., Matsunaga, A.: *Three-dimensional particle-tracking velocity measurements of turbulence statistics and energy budget in a backward-facing step flow.* Int. J. Heat and Fluid Flow, Vol 16 , pp. 477–485, 1995.

[36] Kim, J., Moin P., Moser, R.: *Turbulence statistics in fully developed channel flow at the low Reynolds number.* Int. J. Fluid Mech., Vol 177 , pp. 133–166, 1987.

[37] Klebanoff, P.S.: *Characteristics of Turbulence in a Boundary Layer with Zero Pressure Gradient.* NACA TN 3178, 1954.

[38] Krishnan, V., Squires, K.D, Forsythe, J.R.: *Prediction of separated flow characteristics over a hump using RANS and DES.* 2nd AIAA Flow Control Conference, AIAA 2004-2224, Portland, OR, USA, 2004.

[39] Launder, B.E., Sharma, B.I.: *Application of the Energy-Dissipation Model of Turbulence to the Calculation of Flow Near a Spinning Disc.* Letters in Heat and Mass Transfer, Vol 1 , pp. 131–138, 1974.

[40] Leschziner, M.A.: *At the crossroads of turbulence modelling and simulation: opportunities and challenges.* Proc. 8^{th} IAHR International Symposium on Flow Modelling and Turbulence Measurements, Tokyo, Japan, 2001.

[41] Manceau, R., Bonnet, J.-P. Proc. 10^{th} ERCOFTAC/IAHR/COST Workshop on refined turbulence modelling, Poitiers, France, 2002.

[42] Manhart, M.: *A Zonal Grid Algorithm for DNS of Turbulent Boundary Layers.* Computers and Fluids, Vol 33(3) , pp. 435–461, 2002.

[43] Mason, P.J., Callen, N.S.: *On the magnitude of the subgrid-scale eddy coefficient in large-eddy simulations of turbulent channel flow.* Int. J. Fluid Mech., Vol 162 , pp. 439–462, 1986.

[44] Mellen, C.P, Fröhlich, J., Rodi, W.: *Large-Eddy Simulation of the Flow over Periodic Hills.* Proc. 16^{th} IMACS World Congress, (eds.) Deville, M., Owens, R, Lausanne, Switzerland, 2000.

[45] Menter, F.R.: *Zonal two-equation $k-\omega$ turbulence model for aerodynamic flows.* AIAA Paper 1993-2906, 1994.

[46] Moin, P., Kim, J.: *Numerical investigation of turbulent channel flow.* Int. J. Fluid Mech., Vol 118 , pp. 341–377, 1982.

[47] Neumenn, J., Wengle, H.: *LES of controlled turbulent flow over a rounded step.* Fluid Dynamics Research, Vol 26 , pp. 421–436, 2000.

[48] Nikitin, N.V, Nicoud F. Wasistho B.-Squires K.D., Spalart, P.R.: *An Approach to Wall Modelling in Large-Eddy Simulations.* Phys. Fluids, Vol 12(7) , pp. 1629–1632, 2000.

[49] Nishizawa, A., Takagi, S., Abe, H., Segawa, T., Yoshida, H.: *Toward smart control of separation around a wing-active separation control system part 2.* 5^{th} Symposium on Smart Flow Control of Turbulence, Tokyo, Japan, 2004.

[50] Nishizawa, A., Takagi, S., Abe, H., Segawa, T., Yoshida, H.: *Smart control of separation around a wing.* 6^{th} Symposium on Smart Flow Control of Turbulence, Tokyo, Japan, 2005.

[51] Obi, S., Ohizumi, H., Aoki, K., Masuda, S.: *Turbulent separation control in a plane asymmetric diffuser by periodic perturbation.* Engineering Turbulence Modelling and Experiments 6, Rodi, W. and Marteli, F. Eds.:, pp. 633–642, 1993.

[52] Obi, S.: *personal communication.* 2002.

[53] Perić, M., Lilek Ž.: *User Manual for the FAN–2D, Software for the Calculation of Incompressible Flows, Version 1.0.* Institut für Schiffbau der Universität Hamburg, 1993.

[54] Pope, S.B.: *Turbulent Flows.* Cambridge University Press, 2000.

[55] Rhee, G.H. Sung, H.J.: *Numerical prediction of locally forced turbulent separated and reattaching flow.* Fluid Dynamics Research, Vol 26 , pp. 421–436, 2000.

[56] Rodi, W., Mansour, N.N., Michelassi, V.: *One-Equation Near-Wall Turbulence Modelling with the Aid of Direct Numerical Simulation Data.* J. Fluids Eng., Vol 115 , pp. 196–208, 1993.

[57] Rumsey, C. L.: *personal communication.* 2002.

[58] Rumsey, C.L., Gatski, T.B., Sellers, W.L.,Vatsa, S.A., Viken, S.A.: *Summary of the 2004 CFD validation workshop on synthetic jets and turbulent separation control.* 2nd AIAA Flow Control Conference, AIAA 2004-2217, Portland, OR, USA, 2004.

[59] Schatz, M., Thiele, F.: *Numerical study of high-lift flow with separation control by periodic excitation.* AIAA 2001-0296, 2002.

[60] Seifert, A., Bachar, T., Koss, D., Shepshelovich, M., Wygnanski, I.: *Oscillatory Blowing: A Tool to Delay Boundary-Layer Separation.* AIAA Journal, Vol 31(11) , pp. 2052–2060, 1993.

[61] Seifert, A., Bachar, T., Wygnanski, I.: *Application of active separation control to a small unmanned air vehicle.* Journal of Aircraft, Vol 36(2) , pp. 474–477, 1998.

[62] Seifert, A., Darabi, A., Wygnanski, I.: *Delay of Airfoil Stall by Periodic Excitation.* Journal of Aircraft, Vol. 33(4) , pp. 691–698, 1996.

[63] Seifert, A., Eliahu, S., Greenblat, D., Wygnanski, I.: *Use of pizoelectric actuators for airfoil separation control.* AIAA Journal, Vol 36(8) , pp. 1535–1537, 1998.

[64] Seifert, A., Pack, L.G.: *Active flow separation control on wall-mounted hump at high Reynolds numbers.* AIAA Journal, Vol 37(9) , pp. 1062–1071, 1999.

[65] Seifert, A., Pack, L.G.: *Active flow separation control on wall-mounted hump at high Reynolds numbers.* AIAA Journal, Vol 40(7) , pp. 1363–1372, 2002.

[66] Seifert, A., Pack, L.G.: *Effects of sweep on active separation control at high Reynolds numbers.* Journal of Aircraft, Vol 40(1) , pp. 120–126, 2003.

[67] Spalart, P.R., Allmaras, S.R.: *A one equation turbulence model for aerodynamic flows.* La Recherche Aeŕospatialle, Vol 1 , pp. 5–21, 1994.

[68] Spalart, P.R., Jou, W. H., Strelets, M., Allmaras, S.: *Comments on the feasibility of LES for wings and on hybrid RANS/LES approach.* First AFOSR Int. Conference on DNS and LES, Ruston, Luisiana, USA, 1997.

[69] Spalart, P.R.: *Direct simulation of a turbulent boundary layer up to* $R_\theta =$ 1410. Int. J. Fluid Mech., Vol 187 , pp.61–98, 1988.

[70] Spall, R.E., Phillips, W.F., Alley, N.: *An assessment of five turbulence models in predicting turbulent separation.* ASME Heat Transfer/Fluids Engineering Summer Conference, Charlotte, NC, USA, 2004.

[71] Temmerman, L., Hadžiabdić, M., Leschziner, M.A., Hanjalić, K.: *A Hybrid Two-Layer URANS-LES Approach for Large-Eddy Simulation at High Reynolds Numbers.* International Journal of Heat and Fluid Flow, Vol. 26 , pp. 173–190, 2005.

[72] Tennekes, H., Lumley, J.L.: *A first course in turbulence.* Cambridge, MA: MIT Press, 1972.

[73] Travin, A., Shur, M., Strelets, M., Spalart, P.R.: *Physical and Numerical Upgrades in the Detached-Eddy Simulation of Complex Turbulence Flows.* Fluid Mechanics and Its Application: Advances in LES of Complex Flows.

[74] Tuck, A., Soria, J.: *Active flow control of a NACA 0015 airfoil using a ZNMF jet.* Australian Aerospace Student Conference, Sydney, 2004:, Paper 01, 2004.

[75] Šarić, S., Jakirlić, S., Breuer M., Jaffrézic, B., Fröhlich, J., von Terzi, D., Deng, G., Chikhaoui, O., Manhart, M., Peller, N.: *Issues in hybrid LES-RANS and coarse grid LES of separated flows.* EUROMECH Colloquium 469 on Large-Eddy Simulation of Complex Flows, Dresden, Germany, October, 2005.

[76] Yoshioka, S., Obi, S., Masuda, S.: *Momentum transfer in the periodically perturbed turbulent separated flow over the backward-facing step.* Proceedings of the First International Symposium on Turbulence and Shear Flow Phenomena TSFP-1, Santa Barbara, CA, USA: pp. 1321–1326, 1999.

[77] Yoshioka, S., Obi, S., Masuda, S.: *Organized vortex motion in periodically perturbed turbulent separated flow over backward-facing step.* International Journal of Heat and Fluid Flow, Vol. 22 , pp. 301–307, 2001.

[78] Yoshioka, S., Obi, S., Masuda, S.: *Turbulence statistics of periodically perturbed separated flow over backward-facing step.* International Journal of Heat and Fluid Flow, Vol. 22 , pp. 393–401, 2001.

[79] You, D., Wang, M., Moin, P.: *Large-eddy simulation of flow over a wall-mounted hump with separation control.* Center for Turbulence Research, Stanford, Annual Research Briefs, 2005.

[80] Zhu, J., Rodi, W.: *A low dispersion and bounded convection scheme.* Comput. Meth. Appl. Mech. Eng., Vol. 92 , pp. 87–96, 1991.